QUANTIFICATION ACCURACY FOR I-123 SPECT/CT STUDIES USING LEHR AND ME COLLIMATORS: A MONTE CARLO STUDY

by

Anneray Richards

Submitted in fulfilment of the requirements in respect of the Master's degree MMedSc (Medical Physics) in the Department of Medical Physics in the Faculty of Health Sciences at the University of the Free State.

2 December 2021

Supervisor: Dr. J.A. van Staden
Co-supervisor: Dr. H. du Raan

I, Anneray Richards, declare that the Master's Degree research dissertation, that I herewith submit for the Master's Degree MMedSc (Medical Physics) at the University of the Free State is my independent work, and that I have not previously submitted it for a qualification at another institution of higher education.

Paarl

2 December 2021

Anneray Richards

Acknowledgements:

My sincerest thanks to my supervisors Dr Hanlie du Raan and Dr Johan van Staden. My research would have been impossible without their support. It was a long and challenging journey, but they were there through rough days, and with lots of patience, we got where we needed to be.

Dr Michaella Morphis, her help, friendship and many coffee breaks were a lifesaver. I am profoundly grateful for all the moral and academic support and hours of video calls. She went above and beyond. Thank you, my friend.

The High-performance Computing Division of UFS gave me invaluable help in making all simulation and processing possible. I thank them. I also wish to thank the Nuclear Medicine Department at Universitas Academic Hospital.

The people closest to me cannot be thanked enough. My grandparents, parents, family and friends stood by me with unwavering support. I appreciate you more than I can possibly articulate.

F.K., you are a rock and a light.

Emuel, my best friend, you kept me afloat and reminded me to have fun in the moments in between. You are incredible.

Table of Contents

Abstract

The accurate quantification of Nuclear Medicine single photon emission tomography (SPECT) plays an important part in radiopharmaceutical therapy. Accurately quantifying SPECT images of a diagnostic radionuclide such as I-123 is desirable, although not a straightforward process as it is hindered by the complex decay scheme. I-123 has low-energy primary emissions of 159 keV, and performing acquisitions with a low-energy resolution (LEHR) collimator result in images with high resolution. However, I-123 also has high-energy photon emissions which degrade image contrast and quantification accuracy. This degradation can be reduced by using medium-energy collimators (ME); however, at the expense of spatial resolution. Most clinical facilities have access to LEHR collimators, but not necessarily ME collimators.

The aim of this study was to evaluate the quantification accuracy of I-123 LEHR and ME collimated SPECT images when an optimised OSEM reconstruction protocol is applied. To accomplish the aim three objectives were identified: 1) validation of a SIMIND modelled gamma camera fitted with LEHR and ME collimators, 2) optimisation of the iterative reconstruction algorithm in terms of equivalent iterations and SPECT corrections, and based on these results, 3) evaluation of the quantification accuracy of I-123 LEHR and ME SPECT images.

The first objective of this study, to validate the SIMIND modelled gamma camera fitted with LEHR and ME collimators for I-123, involved comparing measured and simulated I-123 data. Results of measured and simulated planar performance tests (system energy resolution, system spatial resolution, and system sensitivity) were compared for both collimators. The validation included a visual comparison of reconstructed SPECT images of a quality control phantom in terms of uniformity, cold contrast, resolution, and linearity. The measured and simulated planar results for system energy resolution, system spatial resolution and system sensitivity differed by 3.4%, 6.4% and 5.3%, respectively. The visual comparison performed on the reconstructed SPECT images showed good agreement between the measured and simulated data.

The second objective was to optimise the OSEM iterative reconstruction algorithm concerning the number of iterations and SPECT corrections. SPECT images of voxel-based phantoms of spherical objects and image quality phantoms were simulated and reconstructed with different numbers of effective iterations. The count

density recovery, image noise, contrast and resolution were evaluated. The image quality phantom was also reconstructed with different corrections (attenuation, scatter and collimator-detector response (CDR)) and compared. The optimal number of equivalent iterations was selected as 64 and the contribution of the different corrections was appreciated. When septal penetration and scatter was compensated for as part of the CDR correction, the LEHR collimator results were comparable to that obtained with the ME collimator.

This led to the aim of the final objective: to determine the quantification accuracy of I-123 SPECT studies in patient phantoms acquired with LEHR and ME collimators. Using voxel based patient phantoms, the quantification accuracy was assessed for LEHR and ME SPECT images of spherical objects. Quantification errors smaller than 3.8% were recorded for both the LEHR and ME collimators when attenuation, scatter and CDR (including septal penetration and scatter) corrections were applied.

Therefore, to conclude, when appropriate SPECT corrections were applied during the reconstruction of I 123 LEHR and ME SPECT images, the image quality between the collimators were comparable and quantification accuracy of up to 3.8% was achievable.

Keywords: Nuclear Medicine, I-123, SPECT/CT, Monte Carlo simulations, LEHR collimator, ME collimator, optimisation, quantification.

Abbreviations

%RMS	Percentage root mean square
3D	Three-dimensional
A	CT-based attenuation correction
AC	Attenuation correction
A-S	CT-based attenuation correction and ESSE scatter corrections
A-S-CDR	CT-based attenuation, ESSE scatter, and collimator detector response (including geometric, septal scatter and penetration) corrections
A-S-Geo	CT-based attenuation, ESSE scatter, and geometric CDR response corrections
CDR	Collimator-detector response
CF	Calibration factor
CT	Computed tomography
$\boldsymbol{E}$	Photon energy
EI	Equivalent iterations
ESSE	Effective scatter source estimation
FWHM	Full-width at half maximum
FWTM	Full-width at tenth maximum
HE	High-energy
I-123	Iodine-123
I-131	Iodine-131
IQ	Image quality
LEHR	Low-energy high resolution
LEHR-M	Measured LEHR collimator dataset
LEHR-S	Simulated LEHR collimator dataset
LSF	Line spread function
M	Measurement
MC	Monte Carlo
ME	Medium-energy
ME-M	Measured ME collimator dataset
ME-S	Simulated ME collimator dataset
mIBG	Metaiodobenzylguanidine
NaI	Sodium iodide
NEMA	National Electrical Manufacturers Association
NM	Nuclear Medicine
NMISA	National Metrology Institute of South Africa
OSEM	Ordered subset expectation maximization
PVC	Partial volume corrections
PVE	Partial volume effect
RBSC	Reconstruction-based scatter correction

R_c	Collimator resolution
R_E	Energy resolution
R_i	Intrinsic resolution
R_s	System spatial resolution
RC	Recovery coefficient
ROI	Region of interest
RPT	Radiopharmaceutical therapy
S	Simulation
SC	Scatter correction
SIMIND	Simulation of imaging nuclear detectors
SPECT	Single-photon computed tomography
TEW	Triple energy window
UAH	Universitas Academic Hospital
VOI	Volume of interest

Chapter 1: Introduction

Table of Contents

1.1 Overview

1.1.1 Radiopharmaceutical Therapy

Targeted radiopharmaceuticals are used in Nuclear Medicine (NM) to diagnose and plan the treatment of diseases, such as cancer, by assessing patient anatomical structures and active physiological processes. After the administration of the radiopharmaceutical and an allotted waiting period, the images of the patient obtained with a gamma camera would provide information on the uptake of the radiopharmaceutical. The spatial distribution of the radioactivity displayed within a region of interest (ROI) would be an indication of tissue functionality and metabolism. Unusual uptake can imply abnormalities such as cancer or disease.

Radiopharmaceutical therapy (RPT) (Wahl, Ahuja and Clarke, 2021), also known as theragnostics (Frangos and Buscombe, 2019), allows personalised patient diagnosis and treatment. The fundamental principle of RPT is using a diagnostic agent to determine the possible benefits of a therapeutic radionuclide coupled to the same molecular agent (Del Vecchio *et al.*, 2007). This approach allows treatment response predictions/ monitoring and analysis of possible adverse effects (Lee and Li, 2011; Yordanova *et al.*, 2017). RPT aims to optimise personalised therapy; therefore, detailed and accurately quantifiable diagnostic imaging is a prerequisite (Li *et al.*, 2017).

Conventional planar quantification is still used for RPT planning, but the limitations of planar quantification, such as the overlay of distribution information, have promoted the standard use of SPECT/CT due to its improved quantification accuracy.

Single-photon computed tomography (SPECT) provides three-dimensional (3D) information of organ/tissue function through the detection of radioactivity distribution. It is assumed that the image information is directly proportional to the radioactive distribution in the patient. Computed tomography (CT) scans provide information on internal structures' anatomical placement, morphology and densities (Bushberg *et al.*, 2012). By fusing the images from SPECT and CT, the localisation of the detected activity is significantly increased (Munley *et al.*, 1999).

SPECT imaging performed in NM can be influenced by certain physical, technical and patient factors causing artefacts that affect the image quality of the images and

therefore the accuracy of quantification. The physical factors include attenuation, Compton scatter of photons, collimator-detector response (CDR), and partial volume effects (PVE), and are further discussed in section 1.1.4.

The aforementioned physical factors will degrade the images' quantitative information, contrast and resolution. Applying accurate corrections for these factors improve the quantification accuracy of the acquired images. The efficiency of an RPT plan is based on the diagnostic image quantification accuracy. With increasing quantification accuracy, the therapeutic absorbed dose calculation becomes more precise. As a result, tumour control is improved, normal tissue complications are reduced, and treatment plan efficacy is increased (Takam *et al.*, 2008).

1.1.2 Iodine for Radiopharmaceutical Therapy

For decades iodine-131 (I-131) has been used to treat diseases such as hyperthyroidism, thyroid cancer and non-Hodgkin's lymphoma (Greig, McDougall and Halnan, 1973; Dewaraja, Ljungberg and Koral, 2000; Silberstein, 2012; Yeong, Cheng and Ng, 2014). In recent years, I-131 has also been labelled with metaiodobenzylguanidine (mIBG) to treat neuroblastomas (Tang *et al.*, 2000; Kushner *et al.*, 2009; Bombardieri *et al.*, 2010; Theerakulpisut *et al.*, 2018) . I-131 has a half-life of 8.0 days and decays through β^- emissions and emit a principal gamma ray at 364.5 keV (81.2%), with additional gamma emissions at 284.3 keV, 637.0 keV and

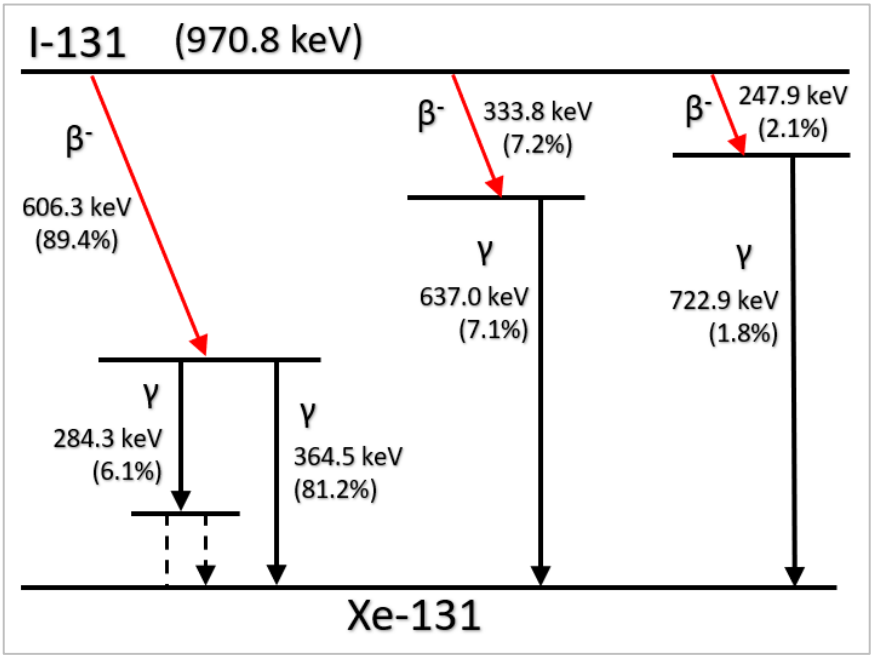

***Figure 1-1**: Diagram of I-131 decay scheme*

722.9 keV (6.1%, 7.1% and 1.8%, respectively), as indicated by Figure 1-1 (Laboratoire National Henri Becquerel, 2014) .

Due to its favourable decay characteristics, Iodine-123 (I-123) (Figure 1-2) is an ideal diagnostic imaging radionuclide. It decays through electron capture to tellurium-123 with a half-life of 13.2 hours, and the primary gamma emission energy of 159.0 keV (83.3% abundance) (Laboratoire National Henri Becquerel, 2004) makes it well suited for gamma camera imaging using a low-energy high resolution (LEHR) collimator. However, the decay scheme of I-123 also includes emissions of photons with energies between 440.0 – 624.6 keV and 628.3 – 783.6 keV.

I-123 labelled metaiodobenzylguanidine (mIBG) is useful in assessing cardiac function and diagnosing heart failure (Nakajima *et al.*, 2007; Gerson *et al.*, 2013; Asghar *et al.*, 2017). It can also be used to visualise tumours of neuroendocrine origin (Dewaraja, Ljungberg and Koral, 2000; Kushner *et al.*, 2009; Matthay *et al.*, 2010; Söderberg *et al.*, 2012; Brady and Shulkin, 2019). Diagnostic imaging with I-123 labelled to a radioligand (I-123-ioflupane, I-123-FP-CIT) has been used to study dopamine transport and allowed the improvement of diagnosis of patients suffering from Parkinson's disease (Dobbeleir *et al.*, 2006; Du, Tsui and Frey, 2006; Crespo *et al.*, 2008; Matsutomo *et al.*, 2015; Niñerola-Baizán *et al.*, 2018; Okada *et al.*, 2018).

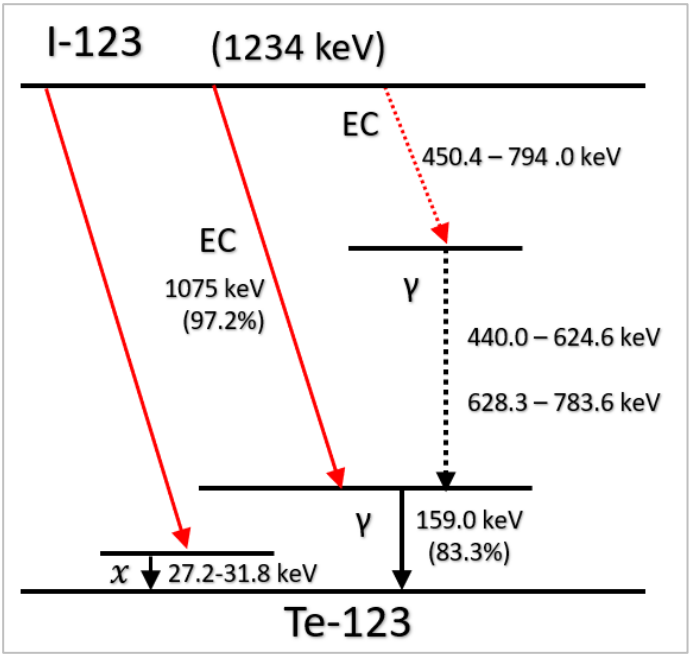

***Figure 1-2**: Diagram of I-123 decay scheme*

I-123 has been proven to be the preferred diagnostic agent in conjunction with I-131 as the therapeutic radioisotope, since it can be labelled to the same pharmaceutical (Bombardieri *et al.*, 2010; Matthay *et al.*, 2010; Lee and Li, 2011; Silberstein, 2012; Parisi *et al.*, 2016; Yordanova *et al.*, 2017).

1.1.3 Gamma Camera Imaging in Nuclear Medicine

1.1.3.1 Gamma Camera Principles

As mentioned before, a gamma camera can be used to acquire images of the uptake of radiopharmaceuticals. The radioactivity in the patient would provide information on tissue physiology by emitting photons of certain energies. A gamma camera is comprised of a scintillation crystal, which detects and converts these emitted photons into light. This light is channelled to photomultiplier tubes where the detected light signal is amplified and converted into an electronic signal. The signal amplitude and position of the event in the crystal are processed by positional circuitry to create a digital image. A collimator, made of lead sheets, can be fitted to the crystal face. The collimator allows only photons travelling in a specific direction relative to the detector to reach the crystal and be recorded as an event, while the rest is absorbed by the lead of the collimator (Cherry, Sorenson and Phelps, 2012).

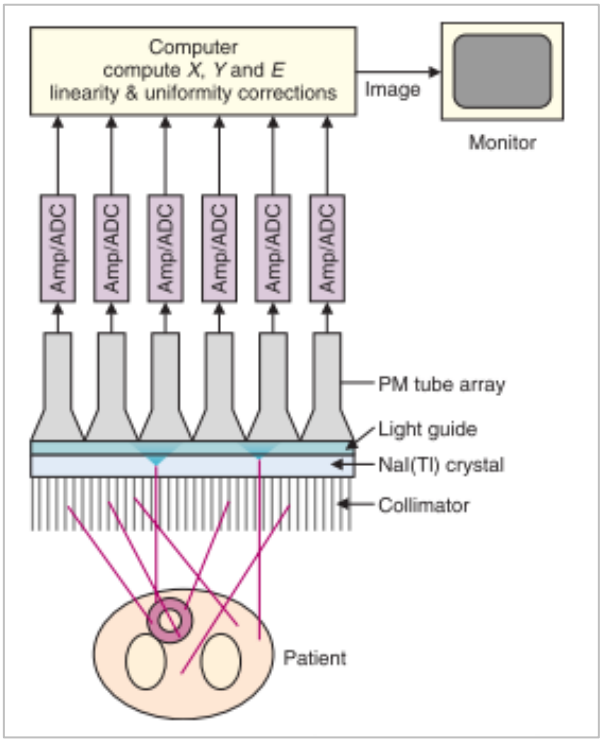

***Figure 1-3**: Basic composition of gamma camera (Cherry, Sorenson and Phelps, 2012)*

1.1.3.2 Collimator Selection for I-123

The collimator selection for I-123 imaging has been a point of debate for some time (Inoue *et al.*, 2004). Each collimator has its own advantages and disadvantages. The high-energy photons (440.0 – 783.6 keV) emitted during I-123 decay easily penetrate the LEHR collimator's septa and degrade the image contrast and quantification accuracy. Acquiring I-123 SPECT images with a medium-energy (ME) collimator would reduce the septal penetration and improve image contrast and quantification accuracy but at the cost of spatial resolution (De Geeter *et al.*, 1996).

In summary, LEHR collimators produce images with high resolution (Macey *et al.*, 1986; Dobbeleir, Hambÿe and Franken, 1999; Rault *et al.*, 2007) and are commonly used for cardiac studies (Inoue *et al.*, 2004), whereas ME collimators are well-suited for quantification studies but have limitations when analysing small objects. I-123 studies with either of these collimator types are viable; however, the collimator choice for I-123 diagnostic imaging is dependent on the clinical need, the type of study that needs to be performed and the resources available (Brown, 2018). Since LEHR is the ideal collimator for Tc-99m imaging, most clinical departments have access to LEHR collimators, but not necessarily ME collimators.

Assessment of and attempts to improve I-123 image quantification has been ongoing (Gilland *et al.*, 1994; Chen *et al.*, 2006; Du, Tsui and Frey, 2006; Matsutomo *et al.*, 2015; Niñerola-Baizán *et al.*, 2018).

1.1.3.3 Performance Evaluation of the Gamma Camera

NEMA is frequently cited when evaluating the performance of gamma camera (National Electrical Manufacturers Association, 2012). The performance of a gamma camera is based on the systems' ability to accurately detect scintillation events, the counting rate it can handle before going into dead time, and to measure the energy of incident gamma rays. Two types of performance measurement exist: intrinsic and system tests. Intrinsic gamma camera tests aim to assess the performance of the detector (crystal and electrical components) without the degrading effects related to a collimator. Collimators are fitted during system tests (clinically realistic conditions) and indicate how well the components of the gamma camera function as a complete unit to produce the final gamma camera images.

i. Energy resolution

Compton scatter is a common occurrence for the range of emission energies used during clinical studies. The gamma camera should be able to distinguish between scattered photons with lower energies and the primary photon energies. This is important to ensure that the positional information of the detected event is correct. The energy resolution of the system determines the efficiency with which this can be accomplished. Statistical fluctuations in the number of collected light photons influence the energy resolution of a scintillation detector. Therefore, the energy resolution of the gamma camera varies with photon energy (E) as $1/\sqrt{E}$. As a result, higher energy photons result in improved energy resolution. The energy resolution ($\mathrm{R_E}$) of a system is defined as the full-width at half maximum (FWHM) of the photopeak expressed as a percentage of photon energy:

$$\mathrm{R_E}(\%) = \frac{FWHM}{E} \times 100 \qquad (1\text{-}1)$$

As energy resolution improves, fewer scattered events will be included in the imaging energy window, increasing image contrast (Bailey *et al.*, 2014).

ii. System Spatial Resolution

The system spatial resolution (R_s) is the smallest distance between point sources in an image that the gamma camera can detect. Two components, intrinsic resolution ($\mathrm{R_i}$) and collimator resolution ($\mathrm{R_c}$), determine the spatial resolution of a gamma camera, which may be expressed as:

$$\mathrm{R}_s = \sqrt{{R_i}^2 + {R_c}^2} \qquad (1\text{-}2)$$

Poor spatial resolution will cause blurring of source edges and decrease the image contrast. The intrinsic spatial resolution is dependent on the energy of the incident photon energy, and the light collection efficiency of the photomultiplier tubes. With increased photon energy more light photons are produced in the scintillation crystal, resulting in less statistical variations in detecting the signal. Thicker crystals result in poorer spatial resolution due to greater spreading of the scintillation light, (greater uncertainty in the X, Y location of original event). However, the intrinsic spatial resolution contribution is negligible to the system resolution, which is mainly affected by the collimator design.

iii. System Sensitivity

The system sensitivity of a gamma camera is defined as the number of detected events within the crystal per unit time and unit of activity for a specific radionuclide energy. The sensitivity is determined by the scintillation crystal composition, the incident photon energy, the energy window settings and the collimator. The test for sensitivity can only be performed with a known activity concentration.

1.1.4 Quantification in Nuclear Medicine

Radioactivity distribution quantification contributes to the interpretation of clinical images, but is also an essential tool to accurately perform internal radionuclide radiation dosimetry. Quantification, per its definition, is to measure and express the quantity of something. In NM studies, the radioactivity distribution (also expressed as image counts) within a ROI or object is quantified. The ability to quantify activity distribution accurately depends largely on the imaging modalities used to capture the distribution of the radioactivity. Factors such as radioactive decay and photon emission energy can also be detrimental to final results.

Image-based quantification in NM imaging modalities is often either relative or absolute. Relative quantification expresses the activity distribution in a ROI in relation to another. For example, the activity uptake in the left ventricle (LV) wall compared to the LV cavity (El Fakhri *et al.*, 1999), or the count density in the LV in relation to the count density in the upper mediastinum (Chen *et al.*, 2006). Absolute quantification is a direct measurement of activity concentration and is routinely used in dosimetry studies (Almeida *et al.*, 1999; Da Silva *et al.*, 2001; Dewaraja *et al.*, 2010; Gregory *et al.*, 2019). To achieve accurate absolute quantification, degrading factors such as attenuation, scatter and loss of resolution in the detector should be corrected for (IAEA, 2014). These image degrading factors form an integral part of the imaging process in NM and the influence of these phenomena on quantification accuracy will be discussed below.

These factors' effect on the image quality and quantitative accuracy can be compensated for by applying the relevant correction methods for attenuation, scatter, CDR and PVE. When these corrections have been applied, reliable quantitative information from SPECT images can be obtained (Frey, Humm and Ljungberg, 2012).

1.1.4.1 Iterative Reconstruction

With SPECT imaging, planar projections of the activity distribution are acquired at multiple angles. An extra dimension is added to the data by reconstructing these projections, which enables the viewer to distinguish overlayed activity distribution information.

The ordered subset expectation maximization (OSEM) iterative algorithm is widely available and regularly used to reconstruct SPECT images (Seret and Forthomme, 2014). The working principles of an iterative reconstruction algorithm are illustrated in Figure 1-4. The reconstruction process starts with a simple estimate of the activity distribution (usually a uniform image). The uniform estimate is forward projected, through summation of intensities along ray paths, to create a set of estimated projections. The estimated projections are compared to the measured projections and the difference is calculated. This difference, or error, is back projected to update the starting estimate. These steps are then repeated (iterated), starting with the newly updated estimates, until converged error estimates are calculated (Cherry, Sorenson and Phelps, 2012; Grimes, 2013). When sufficiently small errors are obtained, the process stops as it is assumed the newly reconstructed image accurately depicts the activity distribution in the patient. For this assumption to be plausible however, the same degrading factors present during the physical measurement has to be incorporated in the forward projection of the estimates. These degrading factors, and the incorporation of their corrections into the iterative reconstruction algorithm will be discussed further.

Because of the time-consuming nature of the iterative process, the OSEM algorithm was introduced (Hudson and Larkin, 1994). With the OSEM iterative algorithm, the total number of projections are subdivided into subsets, each with an equal number of projections. The reconstructed image will therefore be updated after processing each subset of data. Only once all subsets have been processed a single iteration has been completed, but several updates have been performed. To give an example: 64 measured projections are grouped into 4 subsets, each containing 16 projections, and reconstructed with OSEM. An update occurs after the 16 projections have been processed. Within 1 iteration, the estimate projection would be updated 4 times. The more iterations completed, the smaller the reconstruction bias (difference between

estimate and true activity distribution). This gain in error convergence comes at the price of image noise and extended reconstruction time (Dewaraja *et al.*, 2012).

To ensure accurate iterative reconstruction of measured projections, several corrections can be modelled in the algorithm. The implementation of these corrections is shown in the diagram in Figure 1-5.

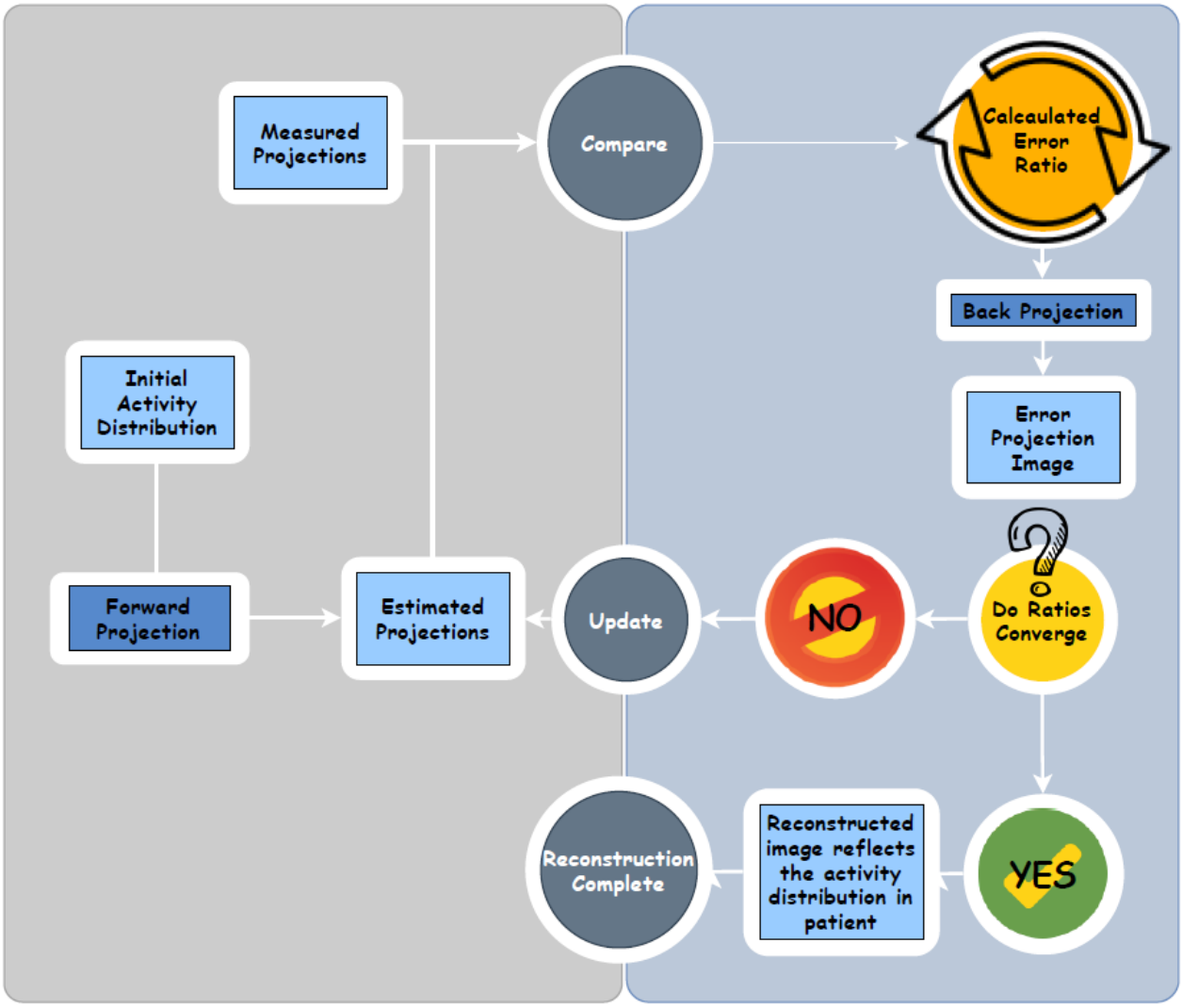

Figure 1-4: *Flowchart describing basic iteration reconstruction process*

i. Attenuation Correction

During attenuation, some photons do not reach the detector due to interactions within the patient. The photon interactions, photoelectric absorption and Compton scatter result in a loss of photons being detected and recorded in the image. The amount of attenuation that can occur is determined by the material thickness, its atomic number (Z) and the energy of the incident photons, which is reflected by the linear attenuation coefficient (μ). If an incident photon beam with an intensity I_0 passes through a

material with a thickness x, the beam that exits will have an intensity I. It can be determined using the following equation:

$$I = I_0 e^{-\mu x} \qquad (1\text{-}3)$$

Furthermore, μ is dependent on the experimental geometry used to determine its value (Rosenthal *et al.*, 1995), which can be either a broad or a narrow beam. With a broad beam geometry, scattered photons contribute to the detected signal. Narrow beam geometry implies that the geometrical arrangement is designed to minimise detection of scattered photons, meaning sufficient collimation is in place.

To perform accurate attenuation correction (AC), the spatial distribution of linear attenuation coefficients (i.e., an attenuation map), is required. Using a hybrid SPECT/CT system allows the acquisition of CT data which can be used to derive an attenuation map. The creation of the attenuation map requires that the CT images be converted from the standard Hounsfield units to linear attenuation coefficients that correspond to the photon energy of the radionuclide used during SPECT acquisition (Ritt *et al.*, 2011). The attenuation map (an array of μ values) is then incorporated into a reconstruction algorithm in order to correct for the attenuation of the gamma rays.

ii. Scatter Correction

A common and dominant interaction that can occur between a photon and a loosely bound electron, at the energy range relevant to this study, is Compton scatter (Ritt *et al.*, 2011). Some scatter will appear in the image due to the intrinsic energy resolution of the detector not being good enough to detect the energy difference between scattered and primary photons. A result of the inclusion of scattered photons in the photopeak is the degradation of the image's contrast and spatial resolution (Dewaraja, Ljungberg and Koral, 2000; Willowson, Bailey and Baldock, 2008). Two scatter correction (SC) methods are used extensively: measured scatter and modelled scatter distributions.

A renowned method for measured scatter correction is the triple energy window (TEW) method. The method incorporates an energy window over the photopeak (the main window), and two narrow scatter windows placed above and below the main energy window. The scatter detected in these scatter windows is subtracted from the main energy window counts (Ogawa *et al.*, 1991; Pereira *et al.*, 2010). The upper scatter

window is used to detect any scattered events occurring from photons with higher energy than the photon energy primarily used for imaging, which is relevant for I-123. The lower scatter window is used to correct for scatter of the main imaging photon. The upper scatter window can be ignored if a mono-energetic isotope is used, as for Tc-99m. An advantage of the TEW method is the ease with which it can be applied for any radionuclide or energy window width. A notable disadvantage of TEW is that there is an amplification of noise due to low statistical information in the narrow scatter windows (Hutton, Buvat and Beekman, 2011).

Scatter correction based on modelling of 3D spatial scatter has proven to be more accurate than the energy window-based subtraction method mentioned above (Kadrmas *et al.*, 1998). Reconstruction-based scatter compensation (RBSC) is an example of a scatter modelling technique. The RBSC method involves modelling of the scatter response function (SRF) in an iterative reconstruction algorithm, mapping the path of scattered photons from the last known position back to the origin. The effective source scatter estimation (ESSE) (Frey and Tsui, 1996) is an example of an RBSC approach. With ESSE, a scatter kernel, derived using Monte Carlo (MC) simulations, is used to estimate the contribution of scatter to the image of the activity distribution. The simulated kernel is a function of the radionuclide energy, the energy window settings and the system spatial resolution of the gamma camera (Ljungberg and Sjögreen Gleisner, 2016). An attenuation map and the source distribution are incorporated into the reconstruction algorithm to calculate the scatter contribution.

iii. Collimator-Detector Response Correction

CDR is an additional source of image degradation that determines SPECT image resolution. The CDR comprises of four components, namely detector intrinsic response (responsible for spatial resolution), collimator resolution, septal penetration and septal scatter (Ritt *et al.*, 2011; Ghaly, Links and Frey, 2017). The intrinsic spatial resolution is determined by the crystal's characteristics and the statistical variation in the pulse formation determines the event's position. The collimator resolution is primarily dependent on the design of the collimator and is also influenced by the distance from the collimator (Kalantari, Rajabi and Saghari, 2011), meaning that the collimator resolution deteriorates with an increase in the collimator-source distance. When photons have high enough energies and pass through the collimator's septa, septal penetration and scatter could occur, which degrades the spatial resolution and

contrast of the SPECT images. The effect of septal penetration and scatter is especially noteworthy at medium- to high-energy gamma rays. All CDR components can be corrected for by using MC simulated kernels. The kernels are determined from in-air point sources simulated at different distances from the detector (Minarik, Sjögreen Gleisner and Ljungberg, 2008; Chun, Fessler and Dewaraja, 2013; Ljungberg and Sjögreen Gleisner, 2016).

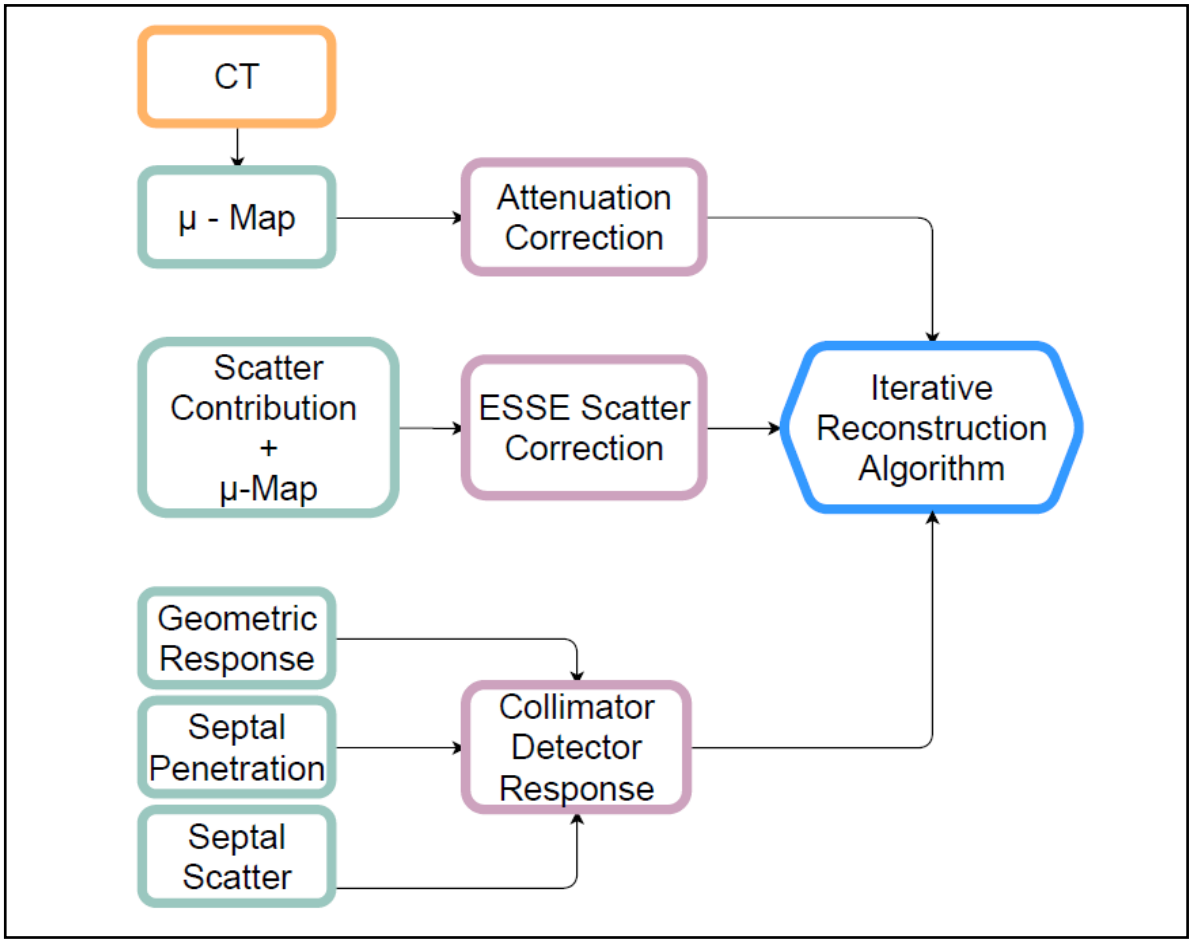

Figure 1-5: *Corrections factors that can be incorporated into iterative reconstruction*

1.1.4.2 Partial Volume Effect Correction

PVEs are caused mainly by the imaging system's limited spatial resolution and the limits set by the pixel size during image sampling (Kalantari, Rajabi and Saghari, 2011). This limitation causes the blurring effect, resulting from spill-in or spill-out between adjacent regions containing activity (Bailey *et al.*, 2014). PVE dominantly occurs in objects/sources that are smaller than two times the spatial resolution of the gamma camera (Saha, 2006). By incorporating a CDR correction (described in section 1.1.4.1iii) as part of the iterative reconstruction algorithm, the PVE are partially

corrected for. However, CDR correction does not entirely eliminate PVE from images, especially for small objects.

PVE can further be corrected for post-reconstruction by applying recovery coefficients (RCs). The RC is defined as the ratio of the recovered (measured) activity concentration in the SPECT images to the true activity concentration (Willowson, Bailey and Baldock, 2008). Physical phantoms containing spheres of various sizes, filled with known activity concentrations can be imaged and analysed to obtain a set of recovery coefficients. PVE caused by spill-out can be compensated for by applying this coefficient to the measured activities of spherical objects of similar sizes (Rousset and Zaidi, 2006).

1.1.5 Monte Carlo Simulations

MC simulation software can implement mathematical modelling to simulate random or statistical processes when physical data collection is impossible. The MC software uses statistical processes to compute outcomes by generating random numbers used in the algorithms. MC is implemented in NM to simulate the transport of electrons and/or photons which is highly random and determine several variables, one of these being the type of interaction the particles undergo (Zaidi, 1999). An advantage of using MC software is that it can be used to create almost any experimental setup, whether clinically applicable or not, and can be used to model statistical variations. CT images of physical phantoms or patients can be recreated as digital voxel-based phantoms and incorporated during MC simulations. Realistic radiation radionuclide distribution uptake and radiation interactions can be reproduced by using these phantoms during simulations.

Authors have used MC codes, such as SIMIND (Ljungberg and Strand, 1989) and GATE (Jan *et al.*, 2004), to model SPECT gamma camera detectors (Dewaraja *et al.*, 2002; Autret *et al.*, 2005; Rodrigues *et al.*, 2007), create photon and electron transport models (Salvat and Fernández-Varea, 2009), evaluate penetration and attenuation, and scatter corrections (Ljungberg and Strand, 1990; Ljungberg *et al.*, 2002; Asl, Sadremomtaz and Bitarafan-Rajabi, 2013). MC simulations have also been used to assess the influence of tumour shape and calibration geometry on quantification accuracy (Dewaraja *et al.*, 2005; D'Arienzo *et al.*, 2016; Ramonaheng *et al.*, 2021) and for the design of gamma camera collimators (Macey *et al.*, 1986; Razavi *et al.*, 2017).

To accurately create a MC modelled gamma camera and implement it as a trusted tool in research studies, the performance of the physical gamma camera should be assessed. If the performance test results of the physical gamma camera correspond to specified criteria, and those results can be replicated using the MC modelled gamma camera to within a certain error margin, the model can be considered validated.

1.2 Aim and Objectives

The thesis aimed to evaluate the quantification accuracy of I-123 LEHR and ME collimated SPECT images when an optimised OSEM reconstruction protocol is applied. The study was based on SIMIND MC simulations of voxel-based phantoms.

The following objectives were pursued and presented in three articles:

1. Create and validate a SIMIND MC based gamma camera for I-123 imaging using the LEHR and ME collimators
2. Optimise the OSEM reconstruction protocol in terms of equivalent iterations and SPECT corrections
3. Assess the quantification accuracy of I-123 SPECT images acquired with LEHR and ME collimators

1.3 Summary of Papers

Chapter 2 – Article 1: *Validation of a Monte Carlo Modelled Gamma Camera for LEHR And ME Collimated I-123 SPECT Imaging*

The aim of this article was to validate a SIMIND MC modelled gamma camera for I-123 using LEHR and ME collimators. The model is based on a Siemens Symbia dual-head gamma camera.

Chapter 3 – Article 2: *Optimisation of I-123 SPECT Image Reconstruction using LEHR and ME Collimators: A Monte Carlo study*

The article aimed to optimise the OSEM reconstruction protocol used when performing quantification of I-123 LEHR and ME images. The reconstruction was optimised in terms of equivalent iterations and applied SPECT corrections. Voxel-based phantoms were used to assess the count recovery of radioactive spheres in a cold background,

and image quality parameters such as uniformity, contrast and resolution were analysed.

Chapter 4 – Article 3: *Quantification Accuracy of I-123 Patient Phantom SPECT Studies using LEHR and ME Collimators*

In this article absolute activity quantification was performed on LEHR and ME collimated I-123 SPECT images. Voxel-based phantom patients and geometrically simple sources were simulated. The optimised reconstructed protocol was implemented and collimator-specific calibration factors were determined for activity concentration recovery. Recovery coefficients were determined to improve the quantification accuracy. The quantification errors calculated for each collimator were compared.

1.4 References

Almeida, P., Ribeiro, M. J., Bottlaender, M., Loc, C., Langer, O., Strul, D., Hugonnard, P., Grangeat, P., Mazière, B. and Bendriem, B. (1999) 'Absolute quantitation of iodine-123 epidepride kinetics using single-photon emission tomography: comparison with carbon-11 epidepride and positron emission tomography', *European Journal of Nuclear Medicine*, 26(12), pp. 1580–1588. doi: 10.1007/s002590050498.

Asl, M. N., Sadremomtaz, A. and Bitarafan-Rajabi, A. (2013) 'Evaluation of six scatter correction methods based on spectral analysis in 99mTc SPECT imaging using SIMIND Monte Carlo simulation', *Journal of Medical Physics*, 38(4), pp. 189–198. doi: 10.4103/0971-6203.121197.

Autret, D., Bitar, A., Ferrer, L., Lisbona, A. and Bardiès, M. (2005) 'Monte Carlo Modeling of Gamma Cameras for I-131 Imaging in Targeted Radiotherapy', *Cancer Biotherapy and Radiopharmaceuticals*, 20(1), pp. 77–84. doi: 10.1089/cbr.2005.20.77.

Bailey, D. L., Humm, J. L., Todd-Pokropek, A. and Van Aswegen, A. (2014) *Nuclear Medicine Physics - A Handbook for Teachers and Students*, *IAEA*. Austria: IAEA. doi: 10.1118/1.3611048.

Bombardieri, E., Giammarile, F., Aktolun, C., Baum, R. P., Bischof Delaloye, A., Maffioli, L., Moncayo, R., Mortelmans, L., Pepe, G., Reske, S. N., Castellani, M. R. and Chiti, A. (2010) '131I/123I-Metaiodobenzylguanidine (mIBG) scintigraphy: Procedure guidelines for tumour imaging', *European Journal of Nuclear Medicine and Molecular Imaging*, 37(12), pp. 2436–2446. doi: 10.1007/s00259-010-1545-7.

Brady, S. L. and Shulkin, B. L. (2019) 'Analysis of quantitative [I-123] mIBG SPECT/CT in a phantom and in patients with neuroblastoma', *EJNMMI Physics.* 6(31), p. 14. doi: 10.1186/s40658-019-0267-6.

Brown, C. M. (2018) *Application of Novel Corrections for Quantification of 123 I SPECT*, *Thesis, PhD*. University of Glasgow. Available at: https://theses.gla.ac.uk/8923/.

Bushberg, J., Seibert, A. J., Leidholdt JR, E. M. and Boone, J. M. (2012) *The Essential Physics of Medical Imaging*. 3rd edn. Edited by C. W. Mitchell and R. Shaw. Philadelphia, PA: Lippincott Williams & Wilkins. doi: 10.1148/radiology.191.3.786.

Chen, J., Garcia, E. V., Galt, J. R., Folks, R. D. and Carrio, I. (2006) 'Optimized acquisition and processing protocols for I-123 cardiac SPECT imaging', *Journal of Nuclear Cardiology*, 13(2), pp. 251–260. doi: 10.1016/j.nuclcard.2006.01.017.

Cherry, S., Sorenson, J. and Phelps, M. (2012) *Physics in Nuclear Medicine*. 4th edn, Edited by L. Barnes, C. Thoms, and D. Scholz. Philadelphia, PA: Elsevier Saunders. doi: 10.1016/C2009-0-51635-2.

Chun, S. Y., Fessler, J. A. and Dewaraja, Y. K. (2013) 'Correction for Collimator-DetectorResponse in SPECT Using Point Spread Function Template', *IEEE Transactions on Medical Imaging*, 32(2), pp. 295–305. doi: 10.1109/TMI.2012.2225441.Correction.

Crespo, C., Gallego, J., Cot, A., Aguiar, P., Sempau, J., Lomeña, F., Calviño, F., Pavía, J. and Ros, D. (2008) 'Quantification of dopaminergic neurotransmission SPECT studies with 123 I-labelled radioligands . A comparison between different imaging systems and data acquisition protocols using Monte Carlo simulation', *European Journal of Nuclear Medicine*, 35, pp. 1334–1342. doi: 10.1007/s00259-007-0711-z.

D'Arienzo, M., Cazzato, M., Cozzella, M. L., Cox, M., D'Andrea, M., Fazio, A., Fenwick, A., Iaccarino, G., Johansson, L., Strigari, L., Ungania, S. and De Felice, P. (2016) 'Gamma camera calibration and validation for quantitative SPECT imaging with 177Lu', *Applied Radiation and Isotopes*. Elsevier, 112, pp. 156–164. doi: 10.1016/j.apradiso.2016.03.007.

Da Silva, A. J., Tang, H. R., Wong, K. H., Wu, M. C., Dae, M. W. and Hasegawa, B. H. (2001) 'Absolute Quantification of Regional Myocardial Uptake of 99m Tc-Sestamibi with SPECT : Experimental Validation in a Porcine Model', *Journal of Nuclear Medicine*, 42(5), pp. 772–779.

Dewaraja, Y. K., Frey, E. C., Sgouros, G., Brill, A. B., Roberson, P., Zanzonico, P. B. and Ljungberg, M. (2012) 'MIRD Pamphlet no. 23: Quantitative SPECT for Patient-Specific 3-Dimensional Dosimetry in Internal Radionuclide Therapy', *Journal of Nuclear Medicine*, 53(8), pp. 1310–1325. doi: 10.2967/jnumed.111.100123.

Dewaraja, Y. K., Ljungberg, M. and Koral, K. F. (2000) 'Characterization of scatter and penetration using Monte Carlo simulation in I-131 imaging', *Journal of Nuclear Medicine*, 41(1), pp. 123–130. doi: 10.1016/j.nima.2010.12.144.

Dewaraja, Y. K., Ljungberg, M., Majumdar, A., Bose, A. and Koral, K. F. (2002) 'A

parallel Monte Carlo code for planar and SPECT imaging: Implementation, verification and applications in I-131 SPECT', *Computer Methods and Programs in Biomedicine*, 67(2), pp. 115–124. doi: 10.1016/S0169-2607(01)00121-3.

Dewaraja, Y. K., Schipper, M. J., Roberson, P. L., Wilderman, S. J., Amro, H., Regan, D. D., Koral, K. F., Kaminski, M. S. and Avram, A. M. (2010) 'I-131 Tositumomab Radioimmunotherapy: Initial Tumor Dose – Response Results Using 3-Dimensional Dosimetry Including Radiobiologic Modeling', *Journal of Nuclear Medicine*, 51, pp. 1155–1163. doi: 10.2967/jnumed.110.075176.

Dewaraja, Y. K., Wilderman, S. J., Ljungberg, M., Koral, K. F., Zasadny, K. and Kaminiski, M. S. (2005) 'Accurate dosimetry in I-131 radionuclide therapy using patient-specific, 3-dimensional methods for SPECT reconstruction and absorbed dose calculation', *Journal of Nuclear Medicine*, 46(5), pp. 840–849. doi: 46/5/840 [pii].

Dobbeleir, A. A., Hambye, A. E., Vervaet, A. M. and Ham, H. R. (2006) 'Dopamine transporter imaging in the human brain . Quantification of Iodine-123-FP-CIT SPECT with a resolution independent technique', in *Quantification and data optimisation of heart and brain studies in conventional nuclear medicine*. s.n. *Thesis, PhD*, University of Groningen. pp. 89–101. Available at: https://research.rug.nl/en/publications/quantification-and-data-optimisation-of-heart-and-brain-studies-i

Dobbeleir, A. A., Hambÿe, A. S. E. and Franken, P. R. (1999) 'Influence of high-energy photons on the spectrum of iodine-123 with low- and medium-energy collimators: Consequences for imaging with 123I-labelled compounds in clinical practice', *European Journal of Nuclear Medicine*, 26(6), pp. 655–658. doi: 10.1007/s002590050434.

Du, Y., Tsui, B. M. W. and Frey, E. C. (2006) 'Model-based compensation for quantitative 123 I brain SPECT imaging', *Physics in Medicine and Biology*, 51, pp. 1269–1282. doi: 10.1088/0031-9155/51/5/016.

El Fakhri, G. N., Buvat, I., Pélégrini, M., Benali, H., Almeida, P., Bendriem, B., Todd-Pokropek, A. and Di Paola, R. (1999) 'Respective roles of scatter, attenuation, depth-dependent collimator response and finite spatial resolution in cardiac single-photon emission tomography quantitation: A Monte Carlo study', *European Journal of Nuclear Medicine*, 26(5), pp. 437–446. doi: 10.1007/s002590050409.

Frangos, S. and Buscombe, J. R. (2019) 'Why should we be concerned about a "g"?', *European Journal of Nuclear Medicine and Molecular Imaging.* 46(519), p. 1. doi: 10.3345/cep.2020.00521.

Frey, E. C., Humm, J. L. and Ljungberg, M. (2012) 'Accuracy and precision of radioactivity quantification in nuclear medicine images', *Seminars in Nuclear Medicine*. Elsevier Inc., 42(3), pp. 208–218. doi: 10.1053/j.semnuclmed.2011.11.003.

Frey, E. C. and Tsui, B. M. W. (1996) 'A New Method for Modeling the Spatially-

Variant, Object-Dependent Scatter Response Function in SPECT', *IEEE Nuclear Science Symposium Conference Record*, pp. 1082–1086.

De Geeter, F., Franken, P. R., Defrise, M., Andries, H., Saelens, E. and Bossuyt, A. (1996) 'Optimal collimator choice for sequential iodine-123 and technetium-99m imaging', *European Journal of Nuclear Medicine*, 23(7), pp. 768–774. doi: 10.1007/BF00843705.

Ghaly, M., Links, J. M. and Frey, E. C. (2017) 'Collimator optimization and collimator-detector response compensation in myocardial perfusion SPECT using the ideal observer with and without model mismatch and an anthropomorphic model observer', *Physics in Medicine and Biology*, 61(5), pp. 2109–2123. doi: 10.1088/0031-9155/61/5/2109.

Gilland, D. R., Jaszczak, R. J., Turkington, T. G., Greer, K. L. and Coleman, R. E. (1994) 'Volume and Activity Quantitation with I-123 SPECT', *Journal of Nuclear Medicine*, 35(10), pp. 1707–1713. Available at: https://jnm.snmjournals.org/content/jnumed/35/10/1707.full.pdf.

Gregory, R. A., Murray, I., Gear, J., Leek, F., Chittenden, S., Fenwick, A., Wevrett, J., Scuffham, J., Tipping, J., Murby, B., Jeans, S., Stuffins, M., Michopoulou, S., Guy, M., Morgan, D., Hallam, A., Hall, D., Polydor, H., Brown, C., Gillen, G., Dickson, N., Brown, S., Wadsley, J. and Flux, G. (2019) 'Standardised quantitative radioiodine SPECT/CT Imaging for multicentre dosimetry trials in molecular radiotherapy', *Physics in Medicine and Biology*, 64(24), pp. 1–3. doi: 10.1088/1361-6560/ab5b6c.

Greig, W. R., McDougall, I. R. and Halnan, K. E. (1973) 'Treatment with Unsealed Radioisotopes', *British Medical Bulletin*, 29(1), pp. 63–68. doi: 10.1093/oxfordjournals.bmb.a070959.

Grimes, J. (2013) *Patient-Specific Internal Dose Calculation Techniques for Clinical Use In Targeted Radionuclide Therapy*. *Thesis, PhD*, University of Guelph. doi: 10.14288/1.0073590.

Hudson, H. M. and Larkin, R. S. (1994) 'Accelerated Image Reconstruction Using Ordered Subsets of Projection Data', *IEEE transactions on medical imaging*, 13(4), pp. 601–609. Available at: https://ieeexplore.ieee.org/stamp/stamp.jsp?arnumber=363108&casa_token=T7Z-tI9VOLgAAAAA:y9ErK3Qs71X7dUsn8p4bkR1NOKQwLPgTmfeA27UxiYTfVq7midHvXeaqnH4d5kwOT66GrlO7G1a5&tag=1.

Hutton, B. F., Buvat, I. and Beekman, F. J. (2011) 'Review and current status of SPECT scatter correction', *Physics in Medicine and Biology*, 56(14). doi: 10.1088/0031-9155/56/14/R01.

IAEA (2014) *Quantitative Nuclear Medicine Imaging: Concepts, Requirements and Methods*, *IAEA Human Health Reports*. Available at: http://www-pub.iaea.org/books/IAEABooks/10380/Quantitative-Nuclear-Medicine-Imaging-

Concepts-Requirements-and-Methods.

Inoue, Y., Shirouzu, I., Machida, T., Yoshizawa, Y., Akita, F., Minami, M. and Ohtomo, K. (2004) 'Collimator choice in cardiac SPECT with I-123-labeled tracers', *Journal of Nuclear Cardiology*, 11(4), pp. 433–439. doi: 10.1016/j.nuclcard.2004.04.009.

Jan, S., Benoit, D., Becheva, E., Lin, H., Chuang, K., Lin, Y., Pet, C., España, S., Herraiz, J. L., Vicente, E., Lazaro, D., Buvat, I. and Loudos, G. (2004) 'GATE: a simulation toolkit for PET and SPECT', *Physics in Medicine and Biology*, 49, pp. 4543–4561. doi: 10.1088/0031-9155/49/19/007.

Kadrmas, D. J., Frey, E. C., Karimi, S. S. and Tsui, B. M. W. (1998) 'Fast implementations of reconstruction-based scatter compensation in fully 3D SPECT image reconstruction', *Physics in Medicine and Biology*, 43(4), pp. 857–873. doi: 10.1088/0031-9155/43/4/014.

Kalantari, F., Rajabi, H. and Saghari, M. (2011) 'Quantification and reduction of the collimator-detector response effect in SPECT by applying a system model during iterative image reconstruction : a simulation study', *Nuclear Medicine Communications*, 33(3), pp. 228–238. doi: 10.1097/MNM.0b013e32834e755f.

Kushner, B. H., Kramer, K., Modak, S. and Cheung, N. K. V. (2009) 'Sensitivity of surveillance studies for detecting asymptomatic and unsuspected relapse of high-risk neuroblastoma', *Journal of Clinical Oncology*, 27(7), pp. 1041–1046. doi: 10.1200/JCO.2008.17.6107.

Laboratoire National Henri Becquerel (2004) *Table de Radionucléides - I-123*. Available at: http://www.lnhb.fr/nuclides/I-123_tables.pdf (Accessed: 5 November 2018).

Laboratoire National Henri Becquerel (2014) *Table de Radionucléides - I-131*. Available at: http://www.lnhb.fr/nuclides/I-131_tables.pdf (Accessed: 20 November 2020).

Lee, D. Y and Li, K. C. P.(2011) 'Molecular Theranostics: A Primer for the Imaging Professional', *NIH Public Access*, 197(2), pp. 318–324. doi: 10.2214/AJR.11.6797.

Li, T., Ao, E. C. I., Lambert, B., Brans, B., Vandenberghe, S. and Mok, G. S. P. (2017) 'Quantitative Imaging for Targeted Radionuclide Therapy Dosimetry - Technical Review', *Theranostics*, 7(18), pp. 4551–4565. doi: 10.7150/thno.19782.

Ljungberg, M. and Sjögreen Gleisner, K. (2016) 'Personalized dosimetry for radionuclide therapy using molecular imaging tools', *Biomedicines*, 4(4), pp. 1–21. doi: 10.3390/biomedicines4040025.

Ljungberg, M., Sjögreen, K., Liu, X., Frey, E., Dewaraja, Y. and Strand, S.-E. (2002) 'A 3-Dimensional Absorbed Dose Calculation Method Based on Quantitative SPECT for Radionuclide Therapy: Evaluation for 131I Using Monte Carlo Simulation ', *Journal of Nuclear Medicine* , 43(8), pp. 1101–1109. Available at:

http://jnm.snmjournals.org/content/43/8/1101.abstract.

Ljungberg, M. and Strand, S. E. (1989) ‘A Monte Carlo program for the simulation of scintillation camera characteristics’, *Computer Methods and Programs in Biomedicine*, 29, pp. 257–272. doi: 10.1016/0169-2607(89)90111-9.

Ljungberg, M. and Strand, S. E. (1990) ‘Scatter and Attenuation Correction in SPECT Using Density Maps and Monte Carlo Simulated Scatter Functions.’, *Journal of Nuclear Medicine.* 31(9), pp. 1560–1567.

Macey, D. J., Denardo, G. L., Denardo, S. J. and Hines, H. H. (1986) ‘Comparison of Low- and Medium-Energy Coffimators for SPECT Imaging with Iodine-123-Labeled Antibodies’, *Journal of Nuclear Medicine*, 27, pp. 1467–1475. Available at: https://jnm.snmjournals.org/content/jnumed/27/9/1467.full.pdf.

Matsutomo, N., Nagaki, A., Yamao, F. and Sasaki, M. (2015) ‘Optimization of iterative reconstruction parameters with 3-dimensional resolution recovery, scatter and attenuation correction in 123I-FP-CIT SPECT’, *Annals of Nuclear Medicine*. Springer Japan, 29(7), pp. 636–642. doi: 10.1007/s12149-015-0987-1.

Matthay, K. K., Shulkin, B., Ladenstein, R., Michon, J., Giammarile, F., Lewington, V., Pearson, A. D. J. and Cohn, S. L. (2010) ‘Criteria for evaluation of disease extent by 123 I-metaiodobenzylguanidine scans in neuroblastoma: A report for the International Neuroblastoma Risk Group (INRG) Task Force’, *British Journal of Cancer*. Nature Publishing Group, 102(9), pp. 1319–1326. doi: 10.1038/sj.bjc.6605621.

Minarik, D., Sjögreen Gleisner, K. and Ljungberg, M. (2008) ‘Evaluation of quantitative Y-90 SPECT based on experimental phantom studies’, *Physics in Medicine and Biology*, 53(20), pp. 5689–5703. doi: 10.1088/0031-9155/53/20/008.

Munley, M. T., Marks, L. B., Scarfone, C., Sibley, G. S., Patz, E. F., Turkington, T. G., Jaszczak, R. J., Gilland, D. R., Anscher, M. S. and Coleman, R. E. (1999) ‘Multimodality nuclear medicine imaging in three-dimensional radiation treatment planning for lung cancer: challenges and prospects.’, *Lung Cancer*, 23(2), pp. 105–14. doi: S0169500299000057 [pii].

National Electrical Manufacturers Association (2012) *NEMA Standards Publication NU 1-2012: Performance Measurements of Gamma Cameras*. 7th edn. Virginia: National Electrical Manufacturers Association.

Niñerola-Baizán, A., Gallego, J., Cot, A., Aguiar, P., Lomeña, F., Javier, P. and Domènec, R. (2018) ‘Optimization of the reconstruction parameters in 123I-FP-CIT’, *Physics in Medicine and Biology*, 63, pp. 1–10. doi: 10.1088/1361-6560/aab799.

Ogawa, K., Harata, Y., Ichihara, T., Kubo, A. and Hashimoto, S. (1991) ‘A Practical Method for Position-Dependent Compton-Scatter Correction in Single Photon Emission CT’, *IEEE Transactions on Medical Imaging*, 10(3), pp. 408–412. Available at: https://ieeexplore.ieee.org/stamp/stamp.jsp?arnumber=97591&casa_token=aSKy7J

0nEtYAAAAA:NqWpbnNdrgJGOwNwhnV9X_IWkHC0QKHMf5wMAX-rkVybeW1pUZXHyGtgRbT8DiT_Yvez2DvdXURZ&tag=1.

Okada, Y., Shiraishi, M., Nakamura, H., Maki, F., Sasaki, N., Hasegawa, Y., Sasaki, O. and Nakashima, Y. (2018) 'Usefulness of the combination of iodine-123-metaiodobenzylguanidine scintigraphy and iodine-123-ioflupane scintigraphy in new-onset Parkinson's disease', *Nuclear Medicine Communications*, 39(11), pp. 983–988. doi: 10.1097/MNM.0000000000000898.

Parisi, M. T., Eslamy, H., Park, J. R., Shulkin, B. L. and Yanik, G. A. (2016) 'I-131-Metaiodobenzylguanidine Theranostics in Neuroblastoma: Historical Perspectives; Practical Applications', *Seminars in Nuclear Medicine*. Elsevier, 46(3), pp. 184–202. doi: 10.1053/j.semnuclmed.2016.02.002.

Pereira, J., Stabin, M., Lima, F., Guimaraes, M. and Forrester, J. (2010) 'Image Quantification for Radiation Dose Calculations - Limitations and Uncertainties', *Health Physics*, 99(5), pp. 688–701. doi: 10.1097/HP.0b013e3181e28cdb.

Ramonaheng, K., van Staden, J. A., du Raan, H. and du Raan, H. (2021) 'The effect of calibration factors and recovery coefficients on 177Lu SPECT activity quantification accuracy: a Monte Carlo study', *EJNMMI Physics*. 8(1), p. 23. doi: 10.1186/s40658-021-00365-8.

Rault, E., Vandenberghe, S., Van Holen, R., De Beenhouwer, J., Staelens, S. and Lemahieu, I. (2007) 'Comparison of Image Quality of Different Iodine Isotopes (I-123, I-124, and I-131)', *Cancer Biotherapy and Radiopharmaceuticals*, 22(3), pp. 423–430. doi: 10.1089/cbr.2006.323.

Razavi, S. H., Kalantari, F., Bagheri, M., Namiranian, N., Nafisi-Moghadam, R., Mardanshahi, A., Emami-Ardekani, A., Sobhan Ardekani, M. and Razavi-Ratki, S. K. (2017) 'Characterization of low, medium and high energy collimators for common isotopes in nuclear medicine: A Monte Carlo study', *Iranian Journal of Nuclear Medicine*, 25(2), pp. 100–104.

Ritt, P., Vija, H., Hornegger, J. and Kuwert, T. (2011) 'Absolute quantification in SPECT', *European Journal of Nuclear Medicine and Molecular Imaging*, 38(Suppl 1), pp. 69–77. doi: 10.1007/s00259-011-1770-8.

Rodrigues, S., Tome, B., Abreu, M. C., Santos, N., Mendes, P. R. and Peralta, L. (2007) 'Monte Carlo Simulation and Experimental Characterization of a Dual Head Gamma Camera', pp. 1–11. Available at: http://arxiv.org/abs/0711.2577 [physics.med-ph].

Rosenthal, M. S., Cullom, J., Hawkins, W., Moore, S. C., Tsui, B. M. and Yester, M. (1995) 'Quantitative SPECT imaging: a review and recommendations by the Focus Committee of the Society of Nuclear Medicine Computer and Instrumentation Council.', *Journal of Nuclear Medicine*, 36(8), pp. 1489–1513.

Rousset, O. G. and Zaidi, H. (2006) 'Correction for Partial Volume Effects in Emission

Tomography', in Zaidi, Habib (ed.) *Quantitative Analysis in Nuclear Medicine Imaging*. Switzerland: Springer, pp. 236–271.

Saha, G. B. (2006) *Physics and Radiobiology of Nuclear Medicine*. 3rd edn. Cleveland: Springer Science and Business Media, Inc. doi: 10.1007/978-0-387-36281-6.

Salvat, F. and Fernández-Varea, J. M. (2009) 'Overview of physical interaction models for photon and electron transport used in Monte Carlo codes', *Metrologia*, 46(2), pp. 112–138. doi: 10.1088/0026-1394/46/2/S08.

Seret, A. and Forthomme, J. (2014) 'Comparison of Different Types of Commercial Filtered Backprojection and Ordered-Subset Expectation Maximization SPECT Reconstruction Software', *Journal of Nuclear Medicine Technology*, 37, pp. 179–187. doi: 10.2967/jnmt.108.061275.

Silberstein, E. B. (2012) 'Radioiodine: The classic theranostic agent', *Seminars in Nuclear Medicine*. Elsevier Inc., 42(3), pp. 164–170. doi: 10.1053/j.semnuclmed.2011.12.002.

Söderberg, M., Mattsson, S., Oddstig, J., Uusijärvi-Lizana, H., Valind, S., Thorsson, O., Garpered, S., Prautzsch, T., Tischenko, O. and Leide-Svegborn, S. (2012) 'Evaluation of image reconstruction methods for 123I-MIBG-SPECT: A rank-order study', *Acta Radiologica*, 53(7), pp. 778–784. doi: 10.1258/ar.2012.120078.

Takam, R., Bezak, E., Yeoh, E. and Marcu, L. (2008) 'Assessment of Normal Tissue Complications and Second Cancer Risks Following Prostate Cancer Irradiation - A Review', *Austral-Asian Jornal of Cancer*, 7(3), pp. 171–184. Available at: https://www.researchgate.net/publication/247162197_Assessment_of_normal_tissue_complications_and_second_cancer_risk_following_prostate_cancer_irradiation.

Tang, H. R., Da Silva, A. J., Matthay, K. K., Price, D. C., Huberty, J. P., Hawkins, R. A. and Hasegawa, B. H. (2000) 'Neuroblastoma Imaging Using a Combined CT Scanner – Scintillation Camera and I131-MIBG', *Journal of Nuclear Medicine,* 42(2)*,* pp. 237–248. Available at: http://jnm.snmjournals.org/content/42/2/237.short.

Theerakulpisut, D., Raruenrom, Y., Wongsurawat, N. and Somboonporn, C. (2018) 'Value of SPECT/CT in Diagnostic I-131 MIBG Scintigraphy in Patients with Neuroblastoma', *Nuclear Medicine and Molecular Imaging*. Nuclear Medicine and Molecular Imaging, 52(5), pp. 350–358. doi: 10.1007/s13139-018-0532-y.

Del Vecchio, S., Zannetti, A., Fonti, R., Pace, L. and Salvatore, M. (2007) 'Nuclear imaging in cancer theranostics', *Quarterly Journal of Nuclear Medicine and Molecular Imaging*, 51(2), pp. 152–163. Available at: https://www.researchgate.net/profile/Antonella-Zannetti/publication/6401425_Nuclear_imaging_in_cancer_theranostics/links/58b0060da6fdcc6f03f40d09/Nuclear-imaging-in-cancer-theranostics.pdf.

Wahl, R. L., Ahuja, S. and Clarke, B. (2021) 'Current Landscape of Radiopharmaceutical Therapies: SNMMI Therapy Task Force Survey', *Journal of*

Medical Physics, 62(5), pp. 11–16.

Willowson, K., Bailey, D. L. and Baldock, C. (2008) 'Quantitative SPECT reconstruction using CT-derived corrections', *Physics in Medicine and Biology*, 53(12), pp. 3099–3112. doi: 10.1088/0031-9155/53/12/002.

Yeong, C. H., Cheng, M. and Ng, K. H. (2014) 'Therapeutic radionuclides in nuclear medicine: Current and future prospects', *Journal of Zhejiang University: Science B*, 15(10), pp. 845–863. doi: 10.1631/jzus.B1400131.

Yordanova, A., Eppard, E., Kürpig, S., Bundschuh, R. A., Schönberger, S., Gonzalez-carmona, M. and Feldmann, G. (2017) 'Theranostics in nuclear medicine practice', *OncoTargets and Therapy*, (October), pp. 4821–4828.

Zaidi, H. (1999) 'Relevance of accurate Monte Carlo modeling in nuclear medical imaging Addendum to "Relevance of accurate Monte Carlo modeling in nuclear medical imaging Relevance of accurate Monte Carlo modeling in nuclear medical imaging"', *Medical Physics*, 26(816), pp. 2566–574. doi: 10.1118/1.598945.

Chapter 2: Paper 1

Validation of a Monte Carlo Modelled Gamma Camera for LEHR And ME Collimated I-123 SPECT Imaging

Table of Contents

Abstract

The purpose of this study was to validate a Siemens Symbia gamma camera model fitted with low-energy high resolution (LEHR) and medium-energy (ME) collimators using the SIMIND Monte Carlo code, with I-123 as the source isotope. The validation focused on performance tests comparing simulation (S) to measurement (M) results using both LEHR and ME collimators. The system energy resolution, planar system spatial resolution, and planar system sensitivity were studied. The validation included a visual comparison of reconstructed SPECT images of a quality control phantom in terms of uniformity, cold contrast, resolution, and linearity. The validation was curated regarding standard deviation and percentage differences for the planar tests between each collimator's simulated and measured data. The LEHR spatial resolution FWHM had a < 1% difference (LEHR-M = 8.1 mm, LEHR-S = 8.1 mm), while the ME data differed by 6.3 % (ME-M = 11.2 mm, ME-S = 11.9 mm). The difference in sensitivity between measured and simulated values for the LEHR and ME was -2.3 % and 5.3 %, respectively. Furthermore, the visual comparison performed on the reconstructed LEHR and ME collimated SPECT images showed good agreement between the measured and simulated data. Overall, the measured and simulated results show that the SIMIND MC code can accurately mimic SPECT data from the Siemens Symbia gamma camera for I-123 using both the LEHR and ME collimators.

2.1 Introduction

Nuclear medicine (NM) is often used to diagnose, evaluate and treat diseases, such as cancer. Theragnostics (Frangos and Buscombe, 2019) is a growing field in NM in which personalised diagnosis and therapy can be improved using molecular targeting. Radioiodine, specifically iodine-131 (I-131), has, for many decades, been used to diagnose and treat differentiated thyroid cancer. Still, the true efficacy of the uptake was only realised in 1996 with the cloning of the sodium iodide symporter (Ahn, 2016). This discovery led to an improved understanding of how I-131 can infiltrate malignant thyroid cells.

I-131 has become even more popular in its use for the treatment of Graves' disease, multinodular goitre and neuroblastomas (Yeong, Cheng and Ng, 2014). It is an isotope that is naturally recognised and absorbed by the thyroid. By labelling it with a pharmaceutical, the detection of other diseases is also possible. I-131 decays (by β^- and γ emission) with a maximum β^--energy of 606.3 keV (89.4% abundance) and a

principal γ-energy of 364.5 keV (81.2% abundance) (Laboratoire National Henri Becquerel, 2014). It has a half-life of 8.0 days, and due to its emissions, I-131 is suitable for both therapy and imaging of target lesions. However, the high energy emissions (γ-emissions: 637.0 keV and 722.9 keV with 7.1% and 1.8% abundance, respectively) make appropriate collimation difficult, which can impede accurate activity quantification (Yordanova *et al.*, 2017). The gamma camera provides sufficient detection efficiency in the energy range 100-200 keV while maintaining a high intrinsic spatial resolution. Given that I-131 does not fully satisfy this requirement, I-123 is frequently chosen for gamma camera imaging.

I-123 decays through electron capture to Te-123 (Laboratoire National Henri Becquerel, 2004) and emits a primary γ-ray with an energy of 159.0 keV (abundance of 83.3%). The energy of this γ-ray and the relatively short half-life of 13.2 hours make I-123 suitable for diagnostic gamma camera imaging. It also has some additional γ-ray emissions, tabulated in Table 2-1. I-123 is routinely used in NM imaging procedures to diagnose thyroid abnormalities, cardiac disease and neuroblastomas, which are some of the most common solid malignancies found in children (Australian Nuclear Science and Technology Organisation, no date; Matthay *et al.*, 2010; Parisi *et al.*, 2016). Localisation, staging, and follow-up of neuroblastomas in patients can be performed with I-123 labelled to metaiodobenzylguanidine (mIBG) (Tang *et al.*, 2000). In recent years confidence has also grown in the use of I-123 mIBG to diagnose cardiac failure (Gerson *et al.*, 2013; Nakajima *et al.*, 2017). The ability to label mIBG with I-131 or I-123 makes it a suitable theragnostic agent (Matthay *et al.*, 2010; Silberstein, 2012).

***Table 2-1**: The most prominent decay transitions for I-123 are listed according to the nuclear data tables provided by Laboratoire National Henri Becquerel (2004).*

Emissions	Energy (keV)	Abundance (photons per 100 disintegrations)
γ emission	158.97	83.25
Range of γ emissions	440.02 – 624.57	2.44
Range of γ emissions	628.26 – 783.59	0.15
X-ray emission*	27.48	70.67
X-ray emission*	31.13	13.16
X-ray emission*	31.76	2.86

**Average energy reported*

From Table 2-1, it can be seen that the higher energy γ-emissions of I-123 have a relatively low abundance (< 2.5%). However, due to septal penetration and scatter detected in the 159 keV photopeak window, these higher energy γ-emissions still have a noticeable influence on the image quality and quantification (Dobbeleir, Hambÿe and Franken, 1999). I-123 is similarly absorbed in the body as I-131. However, the radiation burden from I-123 is much lower than that of I-131 (Bombardieri *et al.*, 2010; Matthay *et al.*, 2010; Yordanova *et al.*, 2017) due to the lack of the β^--emissions and shorter half-life, and is, therefore, a radionuclide of choice for gamma camera imaging.

The use of a high-energy (HE) collimator for imaging I-131 uptake has been proven to be the most suitable choice; however, there is still debate about which collimator should be used for imaging I-123. When I-123 is imaged with a medium-energy (ME) collimator, it is claimed that quantitative accuracy improves because the ME collimator reduces the effect of septal penetration and scatter (Bombardieri *et al.*, 2010) and thus produces images with better contrast (De Geeter *et al.*, 1996). Low-energy high resolution (LEHR) collimators are preferred when better resolution images are a prerequisite; however, scatter and septal penetration correction should then be applied (Macey *et al.*, 1986; Dobbeleir, Hambÿe and Franken, 1999; Rault *et al.*, 2007). With the growing interest in theragnostic procedures, acquiring images resulting in accurate quantification for dosimetry purposes is vital. Selecting the most suitable collimator for I-123 imaging would thus be essential for a diagnostic imaging study. Due to the cost of collimators, there is a possibility that not every NM practice may have access to

both LEHR and ME collimators. It is, therefore, necessary to know the performance characteristics of LEHR and ME collimators for I-123 imaging.

Research in the field of NM requires the handling of radioactivity, with which radiation risks are associated. Monte Carlo (MC) simulation software is ideal for circumventing the hazards involved in handling radioactive sources and reducing the cost involved in repetitive measurements with expensive radionuclides (Zaidi, 1999). The software "Simulation of imaging nuclear detectors" (SIMIND) is a MC simulation program that can be used to perform detector modelling (Ljungberg and Strand, 1989). This code facilitates a detailed study of the highly random radiation transport and the response of different gamma camera detectors. With SIMIND, a virtual model of the gamma camera detector can be constructed and tested in various scenarios using photon-emitting radioisotopes as the source. The characteristics of the modelled detector can be adjusted to suit specific needs (Ljungberg, Strand and King, 2012). SIMIND also enables the user to study various factors (i.e., attenuation, scatter, detector response) that typically influence NM image quality and quantification accuracy.

The SIMIND MC code allows the energy resolution ($\mathrm{R_E}$) to be simulated as a constant value for the specific photon energy of interest. It is also possible to model the energy response of the simulated gamma camera according to the theoretical energy-dependent Gaussian function, which varies with $\frac{1}{\sqrt{Energy}}$. Studies reported by Rault *et al.* (2011) and Ejeh *et al.* (2019) have shown that this relation is not always applicable across all energies. Morphis *et al*. (2021a) modelled the energy response with an energy-dependent function using the relation proposed by Hakimabad, Panjeh and Vejdani-Noghreiyan (2007). The authors showed significant improvement for high-energy photon emitting isotopes such as I-131, which is essential for accurate activity quantification. However, to obtain such an energy model, energy spectra of multiple radionuclide sources should be acquired and validated for the gamma camera model; some clinics have limited access to a variety of radionuclide sources (with energies covering a wide range), and measuring the energy spectra of enough radionuclides on a gamma camera to create an energy model may be troublesome. It will be more convenient if the intrinsic energy resolution of the gamma camera is measured using the isotope of interest and used to model the virtual gamma camera.

This option will be considered for I-123 using both the LEHR and ME collimators in this study.

Before the virtually modelled gamma camera can be used to simulate clinical data, the gamma camera model must be validated. A successful validation will imply that the modelled gamma camera can be used in experimental and clinical simulations – eliminating the handling of radioisotopes and the need for physical phantoms.

This study aimed to validate the SIMIND MC modelled Siemens Symbia gamma camera for I-123 SPECT imaging, using both the LEHR and ME collimators and a constant R_E value.

Although a similar validation was performed by Morphis *et al.* (2021b) for I-123, the gamma camera was modelled using the energy-dependent energy resolution function (Morphis *et al.,* 2021a). In this study, the R_E will be modelled using a constant value obtained intrinsically with I-123.

2.2 Materials and Methods

The modelled gamma camera was validated by comparing measured planar and SPECT data acquired with the dual-head Siemens Symbia™ T16 SPECT/CT gamma camera to SIMIND MC simulated data. A single gamma camera detector was used for measurements and simulations since acceptance test results indicated that the two detectors performed similarly. Three planar validation tests were performed and simulated according to performance measurement guidelines published by NEMA (National Electrical Manufacturers Association, 2012). The selected validation tests evaluate the system's performance regarding intrinsic and extrinsic energy resolution, system spatial resolution, and system sensitivity. Similar tests were also used by other researchers who reported on validations for gamma cameras for different MC codes (Rodrigues *et al.*, 2007; Toossi *et al.*, 2009; Ejeh, van Staden and du Raan, 2019; Ramonaheng *et al.*, 2020; Morphis *et al.*, 2021b). SPECT validation was performed using a Carlson phantom (Fluke Biomedical, 2005) with image quality inserts to compare the measured and simulated SPECT images' uniformity, cold contrast, resolution, and linearity.

In addition to planar and SPECT measurements, computed tomography (CT) images were acquired for each experimental setup. A CT scan protocol with a tube voltage of

130 kVp was used. The CT images were reconstructed with a filtered back-projection algorithm using a smoothing kernel (as defined by Siemens: B08s) and saved in a 512 × 512 matrix with a pixel size of 1.27 × 1.27 mm^2 and slice thickness of 5 mm. The CT images were used for attenuation correction (AC) of SPECT data where applicable. The reconstructed transaxial CT slices were also segmented to create voxel-based digital models used in the MC simulations. The voxel-based digital models were created from the CT data, as explained by Ramonaheng *et al.* (2020).

The SIMIND MC code (version 6.1) was used to model the Siemens Symbia gamma camera, located at Universitas Academic Hospital (UAH) (Bloemfontein, South Africa). The physical gamma camera parameters, such as crystal size, thickness, and collimator dimensions, were obtained from the Siemens Symbia T Series specification sheet (Siemens Healthcare, 2013) and were defined in SIMIND (relevant parameters are listed in Table 2-2). It was decided to use the I-123 intrinsic R_E measured on the Siemens Symbia gamma camera as input for SIMIND to emulate the R_E response of the gamma camera. All simulations were performed with a high number of histories to ensure datasets with low simulation noise.

Table 2-2: *Gamma camera and imaging parameters as defined in SIMIND.*

Parameter name	**SIMIND setup**	
Crystal material	NaI	
Crystal thickness	9.5 mm	
Crystal dimensions	591 x 445 mm^2	
Backscatter material	H_2O	
Backscatter thickness	400 mm	
Intrinsic spatial resolution (measured with Tc-99m)*	3.8 mm	
Collimator	**LEHR**	**ME**
Hole diameter X	1.11 mm	2.94 mm
Hole diameter Y	1.28 mm	3.29 mm
Thickness	24.05 mm	40.64 mm
Septal thickness	0.16 mm	1.14 mm

* *Obtained from acceptance test results.*

The system validation tests were measured and simulated using I-123 with both the LEHR and ME collimators. Images were obtained with a 15% energy window centred

over the 159 keV photopeak. Planar images were analysed using the freeware software ImageJ (Schneider, Rasband and Eliceiri, 2012). All SPECT images were reconstructed using the ordered subset expectation maximization (OSEM) reconstruction algorithm (Hudson and Larkin, 1994) incorporated in a dosimetry software package developed at Lund University (Sjögreen *et al.*, 2005). The reconstruction package performs AC using an attenuation map generated from CT data (Frey, Humm and Ljungberg, 2012), a scatter correction using the effective source scatter estimation (ESSE) proposed by Frey and Tsui (1993), and a collimator detector response (CDR) correction that corrects for the geometric response, collimator scatter and septal penetration.

I-123 activity was measured using a Biodex Atomlab™ 500 dose calibrator (Biodex Medical Systems, New York, NY, USA). The accuracy of the dose calibrator for I-123 can be traced to a secondary standard through the National Metrology Institute of South Africa (NMISA) in Cape Town, South Africa.

The percentage differences between measured and simulated results were calculated according to equation (*2-1*).

$$Percentage\ Difference\ (\%) = \frac{Simulated\ Value - Measured\ Value}{Measured\ Value} \times 100 \qquad (2\text{-}1)$$

Average values of experimental data were obtained from three independent measurements. Where appropriate, simulated and measured spectra distributions and images were visually evaluated and compared.

2.2.1 Gamma Camera Measurements

2.2.1.1 Energy Resolution

The intrinsic and extrinsic energy spectra were acquired with the gamma camera for I-123. For the intrinsic energy spectra, a point-like source of I-123 (2.7 MBq) was positioned on a Styrofoam block at 125 cm ± 0.5 cm from one of the gamma camera detectors, with no collimator fitted. Due to space limitations, the source could not be placed five times the camera's field of view away as recommended by NEMA (National Electrical Manufacturers Association, 2012). An intrinsic energy spectrum was acquired with 30 000 counts in the peak energy channel at 159 keV. Similarly, extrinsic energy spectra were acquired using a point-like source of 181.7 MBq I-123, with the

LEHR and ME collimators fitted consecutively to the gamma camera's detector. The extrinsic energy resolution acquisition setup is depicted in Figure 2-1.

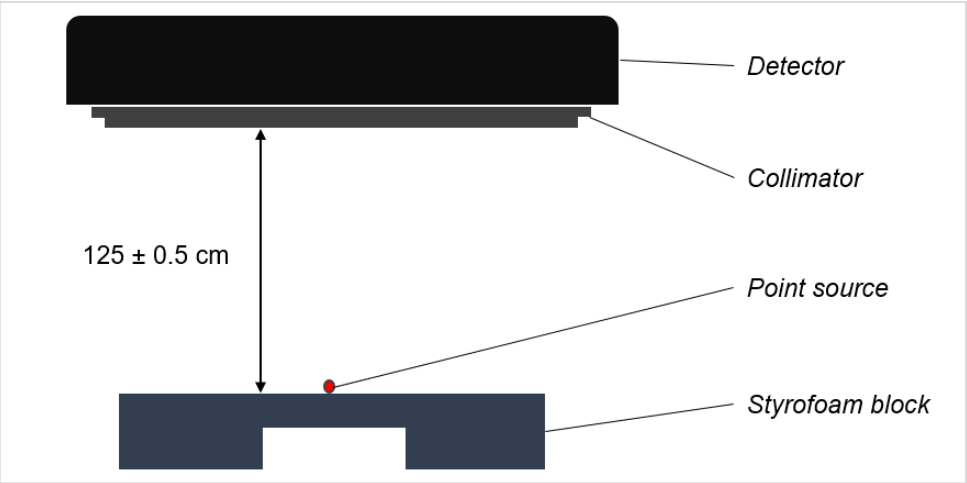

Figure 2-1: *Gamma camera setup used for the extrinsic energy resolution acquisitions.*

Using the public domain software ImageJ, a Gaussian function was fitted to the 159 keV photopeak to determine the full-width at half maximum (FWHM) for the I-123 photopeak (E) of each energy spectrum. The R_E was calculated using equation (*2-2*).

$$R_E\,(\%) = \frac{FWHM}{E} \times 100 \qquad (2\text{-}2)$$

R_E values were reported for the intrinsic spectrum as well as for the extrinsic spectra acquired with the LEHR and ME collimators. The measured intrinsic R_E value was further used as input in SIMIND to define the energy response of the gamma camera, as explained above.

2.2.1.2 Planar System Resolution

The planar system spatial resolution was calculated from images acquired with two capillary tubes (1 mm inner diameter), each filled with 27.0 MBq (53.98 MBq/ml) of I-123 for both the LEHR and ME collimators. The capillary tubes were placed 100 mm apart on a Styrofoam block on the patient bed. Static planar images were acquired in a 512 × 512 image matrix with a pixel size of 1.2 × 1.2 mm^2 at three different source-detector distances of 50 mm, 100 mm, and 150 mm ± 2 mm (see Figure 2-2). The images were acquired until 10 000 counts were reached in the peak location of each of the line spread functions (LSFs). The three different source-detector distances

allowed for the analysis of the simulation algorithm's ability to model scatter and septal penetration correctly.

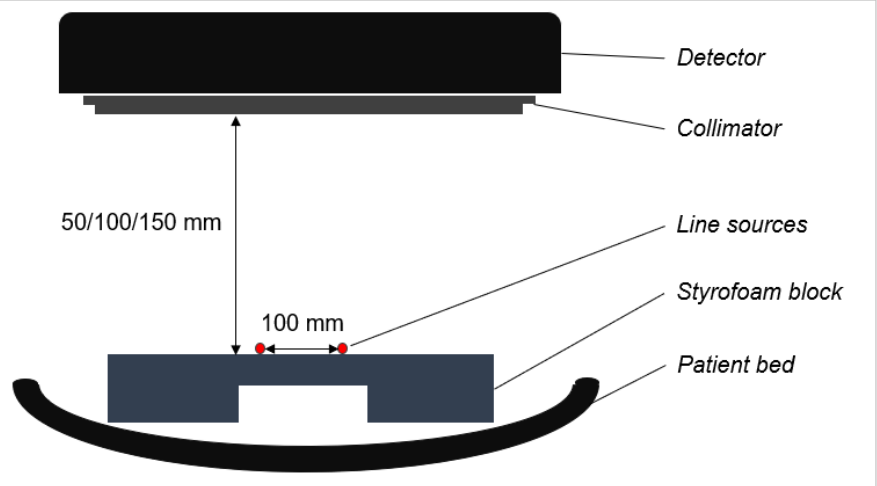

Figure 2-2: *Gamma camera setup used for the planar system resolution acquisitions.*

Three line-profiles, with widths of 10 pixels (12 mm) each, were drawn perpendicular across each image of the capillary tubes. The drawn profiles were equally spaced along the length of the capillary tube image to obtain the LSFs. Using ImageJ, a Gaussian function was fitted to each LSF, and the FWHM and full-width at tenth maximum (FWTM) values were determined from the fitted Gaussian functions. These average FWHM and FWTM values determined for the three measurements at different distances were reported in units of mm for both collimators.

2.2.1.3 Planar System Sensitivity

System sensitivity was obtained by adding 92.84 MBq of I-123 to 10 ml of water in a plastic petri dish with an inner diameter of 87 mm. The petri dish was placed on a Styrofoam block and positioned 100 ± 2 mm from the collimated detector (Figure 2-3). Planar static images with pixel size 2.4 × 2.4mm^2 (256 × 256 matrix) were acquired with the LEHR and ME collimators fitted, respectively. These images were acquired for 4 000 000 counts per image, and the acquisition times for the two collimators were noted. The planar images were analysed using ImageJ. The sensitivity value (cps/MBq) for each collimator was calculated by using equation *(2-3)* after applying a decay correction (taking into consideration the time-lapse between activity

measurement and imaging). Sensitivity values were obtained for both LEHR and ME collimators.

$$Sensitivity\ (cps/MBq) = \frac{total\ counts\ in\ image}{acquisition\ time\ (s) \times activity\ (MBq)} \qquad (2\text{-}3)$$

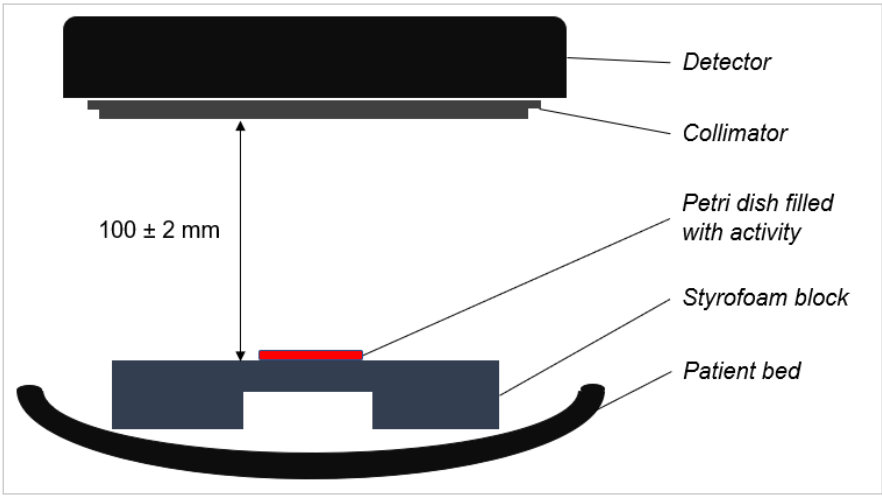

***Figure 2-3**: Gamma camera setup used for the planar system sensitivity acquisition.*

2.2.2 SPECT Image Quality

For the SPECT validation, a phantom study was conducted to qualitatively evaluate the overall performance of the gamma camera. The cylindrical Carlson phantom (Fluke Biomedical, 2005) with inserts was selected for this study. The Carlson phantom was designed for periodic performance testing of SPECT and PET systems (Fleming *et al.*, 2000; Sadremomtaz and Taherparvar, 2013). This phantom consists of a hollow cylinder with an inner diameter of 203 mm and a height of 318 mm. The phantom's inserts are shown in Figure 2-4 (Fluke Biomedical, 2005) and are designed

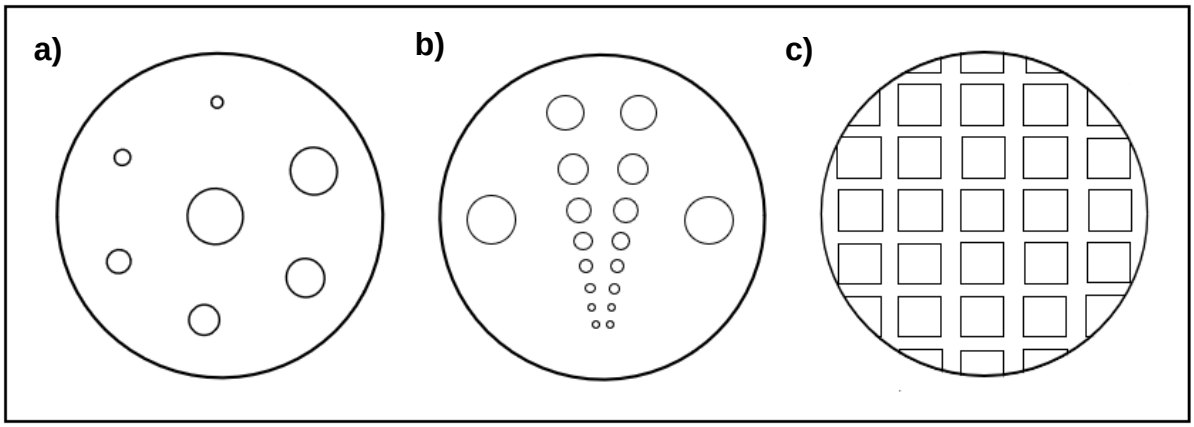

***Figure 2-4:** Superior view of three Carlson inserts: (a) cold lesion contrast insert, (b) hot lesion resolution insert and (c) linearity insert.*

to test different components of image quality. The phantom was filled with a radioactive water solution containing 97.31 MBq of I-123.

The first insert (a) represents cold (non-radioactive) lesions in a hot (radioactive) background and is used to evaluate cold contrast and resolution. Seven acrylic rods, with diameters of 5.9, 7.3, 9.2, 11.4, 14.3, 17.9, and 22.4 mm, represent the cold lesions. Seven solid spheres of the same diameters as the rods are attached via thin supports to the rods. The second insert (b) in the diagram embodies hot lesions through nine pairs of holes cut into an acrylic block (thickness of 63.5 mm) separated by a distance equal to the diameter of the hole (4.7, 5.9, 7.3, 9.2, 11.4, 14.3, 17.9, 22.4 and 38.5 mm). This insert is used for the qualitative evaluation of the system's spatial resolution. The third insert (c) is used to assess the linearity of the SPECT images. It consists of a 50.8 mm thick acrylic block with a crossed grid of channels cut 38.1 mm deep into a square pattern. After inserting all three inserts in the cylinder, there is also an area in the phantom with no inserts used to evaluate the SPECT images' uniformity.

SPECT projection images were acquired using a standard clinical imaging protocol (step and shoot mode, non-circular orbit of rotation, 64 projections, 40 seconds per projection, a matrix size of 128 × 128, and a pixel size of 4.8 × 4.8 mm^2). SPECT projections of the I-123 filled Carlson phantom were acquired with the LEHR and ME collimators, respectively. CT data were acquired following the SPECT acquisition for AC and to create a voxel-based phantom for the simulation study. The SPECT projection images were reconstructed with the OSEM iterative reconstruction algorithm as described previously.

Five consecutive reconstructed slices in each section (uniform section, cold lesion insert, hot lesion insert, and linearity insert) were averaged and analysed qualitatively for any significant discrepancies or differences.

2.2.3 Monte Carlo Simulations

As explained before, the gamma camera model was defined in SIMIND based on specifications and measurements of the physical gamma camera. A voxel-based model of each measurement setup and the radioactive concentration defined in a text file was used for the SIMIND input. For each validation test, the distance to the detector, source activity, and stop conditions were kept identical to the measured experimental setup. Additional information regarding the SIMIND setup parameters is

given in Appendix A. Image processing and analysis were performed similarly to the physical measurements.

Four datasets were created for each validation test, i.e., the measured and simulated LEHR collimator datasets (LEHR-M and LEHR-S) and the measured and simulated ME collimator datasets (ME-M and ME-S).

Results obtained for the different validation tests from the measured (LEHR-M and ME-M) and the simulated datasets (LEHR-S and ME-S) were compared and reported.

2.3 Results

2.3.1 Gamma Camera Measurements

2.3.1.1 Energy Resolution

The measured and simulated energy spectra for the I-123 point-like source in-air are compared in Figure 2-5. All graphs were normalised to the photopeak value at 159 keV for easy comparison. The intrinsic energy spectra are shown in Figure 2-5a, with the extrinsic data for the LEHR and ME collimators displayed in Figure 2-5b and 5c. The figures present the higher energy regions exhibiting low abundances (480 – 580 keV) as inserted graphs. Since there is a cut-off of photon energies below 20 keV for the Siemens Symbia gamma camera, these energies were not considered and were excluded in the display. Good agreement was found regarding the position of the photopeaks. Significant differences were observed between the measured and simulated energy spectra maxima values at low energy (20-40 keV) values.

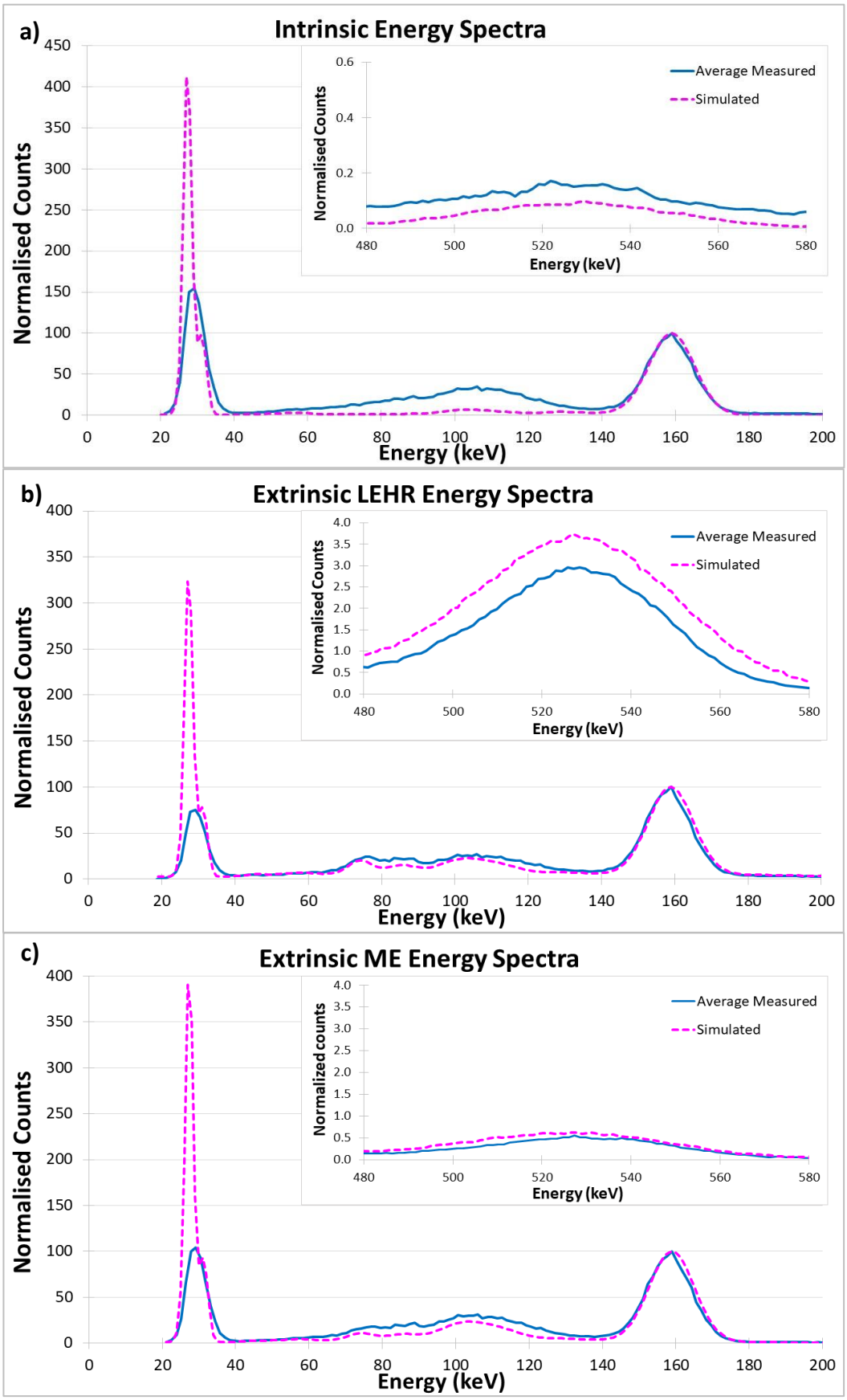

Figure 2-5: *Average measured (solid line) and simulated (dashed line) I-123 intrinsic (a) and extrinsic energy spectra acquired with LEHR (b) and ME (c) collimator, at a source-detector distance of 125 cm.*

The FWHM and R_E values were calculated for the 159 keV photopeak. The results are shown in Table 2-3, along with the percentage differences between the measured and simulated data. The measured intrinsic R_E value for I-123 was 9.1% compared to the simulated intrinsic value of 9.2%.

***Table 2-3**: Average measured and simulated I-123 intrinsic and extrinsic resolution values obtained for the 159 keV of I-123 with LEHR and ME collimators at a source-detector distance of 125 cm.*

	Measured*	**Simulated**	**% Difference**
Intrinsic Energy Spectra			
FWHM (keV)	14.4 ± 0.03	14.6	1.4
R_E (%)	9.1 ± 0.02	9.2	1.1
Extrinsic Energy Spectra: LEHR collimator			
FWHM (keV)	14.5 ± 0.04	15.0	3.4
R_E (%)	9.2 ± 0.02	9.5	3.3
Extrinsic Energy Spectra: ME collimator			
FWHM (keV)	14.3 ± 0.06	14.7	2.8
R_E (%)	9.1 ± 0.04	9.2	1.1

**average values reported with standard deviation*

The measured intrinsic R_E value of 9.1% was used as the input value in SIMIND for simulations for the remainder of the study. This choice of energy resolution input implies that a constant energy response was simulated for the different energy values for the I-123 energy spectra. Simulations with a constant energy response resulted in an improved energy resolution at lower energy values (20 – 40 keV), as shown in Figure 2-5.

2.3.1.2 Planar System Resolution

Figure 2-6 shows the measured and simulated planar system spatial resolution images and LSFs obtained for I-123 using the LEHR (Figure 2-6a and Figure 2-6c) and ME (Figure 2-6b and Figure 2-6d) collimators. The images and profiles are shown for images obtained at a source-detector distance of 100 mm.

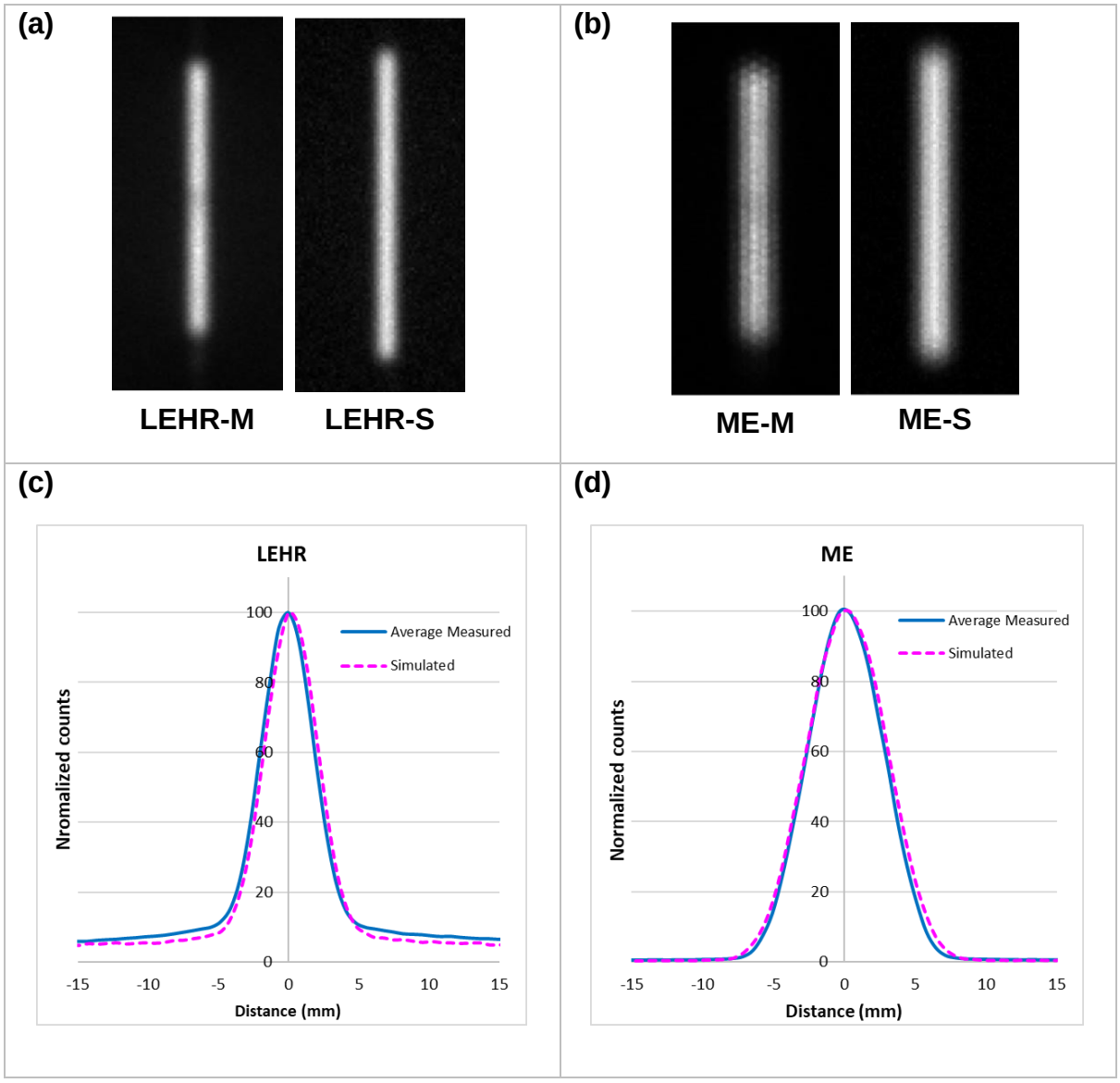

Figure 2-6: *Measured (M) and simulated (S) planar system resolution images obtained for I-123 at a source-detector distance of 100 mm with the LEHR (a) and ME (b) collimators with the corresponding line spread functions (c) and (d).*

The average FWHM and FWTM values obtained from the measured and simulated data are shown in Table 2-4 for both collimators, at source-detector distances of 50 mm, 100 mm, and 150 mm. Good agreement was obtained between the measured and simulated FWHM values for both the LEHR and ME collimators. The FWTM values for the LEHR collimator show up to 12.1% difference between the measured and simulated data, however this is an absolute difference of only 2.3 mm. The ME collimator measured and simulated FWTM values had better agreement with 7.1% difference (absolute difference of 1.4 mm).

Table 2-4: *Measured (M) and simulated (S) I-123 planar system resolution values obtained at 50, 100, and 150 mm with the LEHR and ME collimators. Percentage difference (%Diff) between measured and simulated data are also reported.*

	FWHM (mm)			FWTM (mm)		
	LEHR-M	**LEHR-S**	**%Diff**	**LEHR-M**	**LEHR-S**	**%Diff**
50 mm	6.3 ± 0.4	6.1	-3.2	14.6 ± 0.5	13.4	-8.2
100 mm	8.1 ± 0.1	8.1	0.0	19.0 ± 1.4	16.7	-12.1
150 mm	10.2 ± 0.1	10.1	-1.0	22.8 ± 0.9	20.1	-11.8
	ME-M	**ME-S**	**%Diff**	**ME-M**	**ME-S**	**%Diff**
50 mm	7.8 ± 0.0	8.3	6.4	14.1 ± 0.1	14.9	5.7
100 mm	11.2 ± 0.0	11.9	6.3	19.6 ± 0.0	21.0	7.1
150 mm	14.5 ± 0.1	14.9	2.8	25.3 ± 0.1	26.0	2.8

2.3.1.3 Planar System Sensitivity

The measured and simulated sensitivity values calculated for the LEHR and ME collimators are reported in Table 2-5. Table 2-5 shows good agreement between the measured and simulated sensitivity values. The measured sensitivity values were 184.7 ± 0.3 and 121.6 ± 0.2 cps/MBq for the LEHR and ME collimators, respectively. The corresponding simulated sensitivity values were 180.4 and 128.0 cps/MBq, showing minor differences of 2.3% and 5.3% with the measured values.

Table 2-5: *Average measured (M) and simulated (S) planar I-123 system sensitivity obtained with LEHR and ME collimators.*

	Sensitivity (cps/MBq)		% Diff
Collimator	**M***	**S**	
LEHR	184.7 ± 0.3	180.4	-2.3
ME	121.6 ± 0.2	128.0	5.3

**Averaged sensitivity values reported with standard deviation*

The images of the measured and simulated sensitivity acquisitions for the four datasets are displayed in Figure 2-7. The measured images shown in Figure 2-7 indicate that the activity was not evenly distributed in the petri dish during acquisitions. The activity distribution for the simulated images were perfectly uniform. This activity

distribution differences would however not affect the calculated sensitivity values as the total counts in these images are recorded.

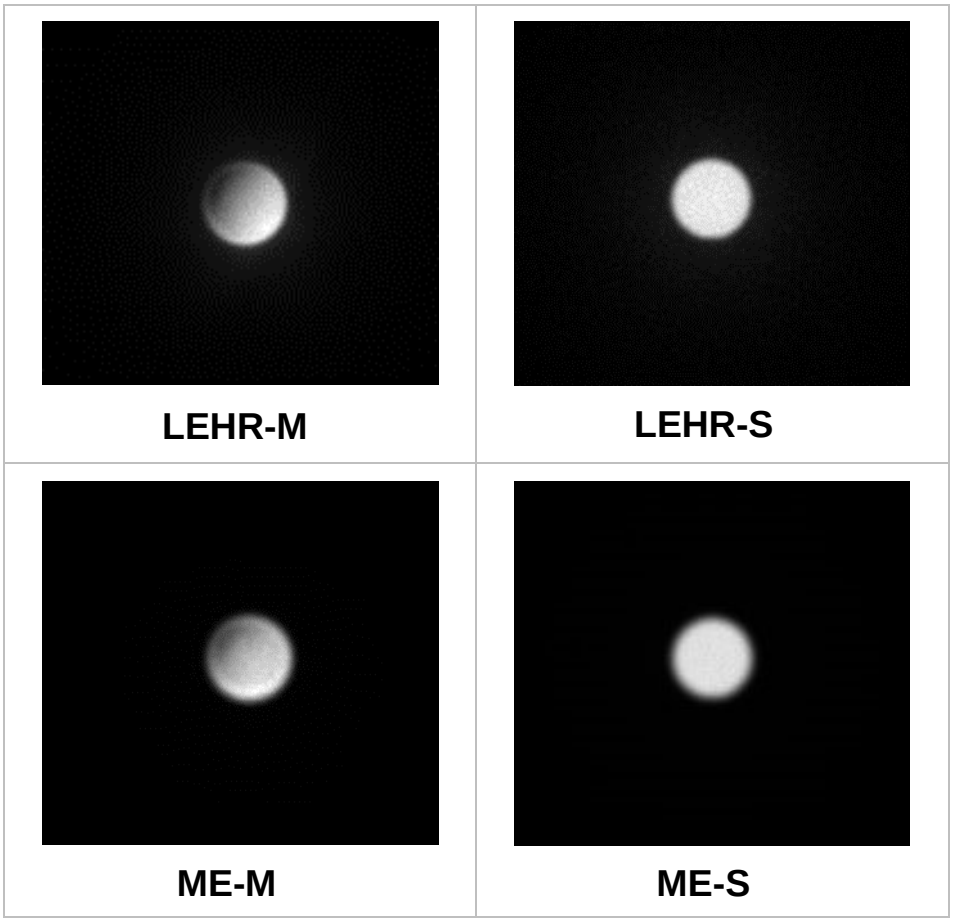

Figure 2-7: *Measured (M) and simulated (S) I-123 planar sensitivity images acquired with the LEHR and ME collimators*

2.3.2 SPECT Image Quality

Table 2-6 summarises the images obtained after SPECT reconstruction of the measured and simulated Carlson phantom projection data using the LEHR and ME collimators. Transaxially reconstructed slices of the uniform section, cold lesion contrast insert, hot lesion resolution insert, and linearity insert are shown for the LEHR-M, LEHR-S, ME-M, and ME-S datasets. Visually, the reconstructed image slices obtained from the measured and simulated datasets compared well for the LEHR as well as the ME collimator (Table 2-6).

Table 2-6: *The reconstructed images of the uniformity section, cold lesion contrast, hot lesion resolution and linearity inserts of the Carlson phantom for LEHR and ME, measured (M) and simulated (S) datasets.*

	Uniform Section	Cold lesion contrast	Hot lesion resolution	Linearity insert
LEHR-M		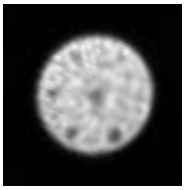	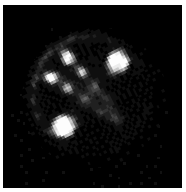	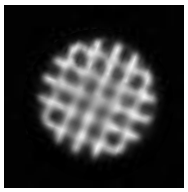
LEHR-S			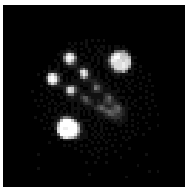	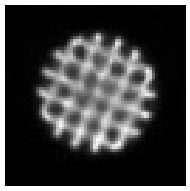
ME-M	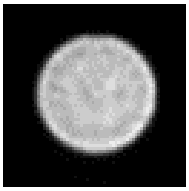	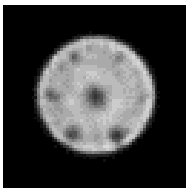	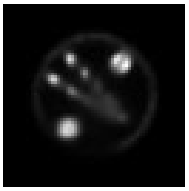	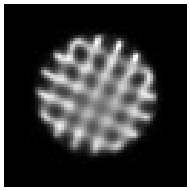
ME-S	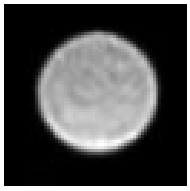	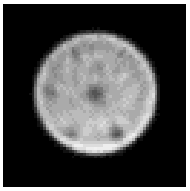	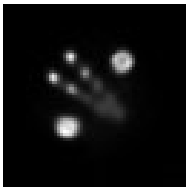	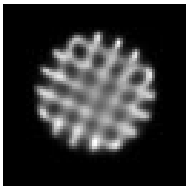

2.4 Discussion

2.4.1 Gamma Camera Measurements

2.4.1.1 Energy Resolution

In this study, the energy resolution was modelled with a constant energy response. Figure 2-5 a, b, and c show good agreement between the simulated and measured I-123 energy spectra for the intrinsic and extrinsic data. The intrinsic energy resolution compared very well, with only a 1.1% difference between the measured and simulated energy resolution values.

Low energy emissions are visible at 27-31 keV on all energy spectra. The individual low energy photopeaks (27.2, 27.5, 31.1 and 31.8 keV) could not be resolved due to the limited energy resolution of the gamma camera. The slight energy offset between

the measured and simulated spectra at these low energy photopeaks can be attributed to the non-linear energy response of the detector to Compton and photoelectric events, which was not considered in the simulations (Cherry, Sorenson and Phelps, 2012). This occurrence was also reported by Ramonaheng *et al.* (2020) for Lu-177. The significant difference in amplitude between the measured and simulated 27-31 keV photopeak for all three scenarios can be attributed to the energy response of the gamma camera that is not constant across all energies, as well as the normalisation of the graphs. The simulated spectra at energies below 159 keV are thus emulated with a better energy resolution than what was obtained in the measured data. For this reason, the amplitude of the simulated low energy photopeak (27-31 keV) exceeds that of the measured data. The simulated peak shows a slightly better energy resolution value for all three scenarios for the low energy emissions. Due to the improved energy resolution at lower energy values, the simulated energy spectra for the LEHR and ME collimators also show the contribution of the lead escape x-rays at ±75 keV (Cherry, Sorenson and Phelps, 2012). The simulation of these lead x-rays is essential to accurately reproduce experimental data below 100 keV. There is a notable difference between the measured and simulated intrinsic spectra between 55 keV and 130 keV. The reason for this is the backscatter of the 159 keV photons originating from the second detector, which is present during gamma camera measurements but absent during simulations. The second detector can also contribute to more characteristic lead x-rays. This difference is not seen for the extrinsic energy spectra due to the collimation that limits the contribution of backscatter and characteristic lead x-rays from the second detector.

The inserted graphs in Figure 2-5 show good agreement between the measured and simulated data for the high energy photons (480 – 580 keV) in the intrinsic and extrinsic spectra. The extrinsic energy spectra demonstrate a more prominent presence of the high energy photons with the LEHR collimator compared to the ME collimator (Figure 2-5b and 5c). The LEHR simulated profile has a poorer energy resolution at these high energies than the measured data. The gamma camera was modelled in SIMIND with a constant energy resolution response using the energy resolution measured for the 159 keV photopeak of I-123. Therefore, it is assumed that the energy resolution at all energies is the same, however it is known that the energy response of the detector is not linear (Cherry, Sorenson and Phelps, 2012).

The ME simulated and measured data show better agreement in the 480-580 keV range, even considering the slightly poorer energy resolution of the simulated data. Due to the design of the collimators, more septal penetration occurs in the LEHR collimator than in the ME collimator. The small differences between the amplitudes of the measured and simulated spectra in the high energy region can be attributed to the normalisation of the energy spectra at 159 keV and the non-linear energy response of the detector at these high energy values.

All graphs showed a good correlation between the measured and simulated data for the 159 keV photopeak area. This is also confirmed with the calculated FWHM and energy resolution values reported in Table 2-3.

The largest difference (3.4%) in the energy resolution value was obtained for the LEHR collimator. The ME collimator presented slightly better energy resolution than the LEHR collimator (< 2% difference between ME and LEHR simulated energy resolution). This can be attributed to the contribution of septal penetration and scatter of the high energy photopeaks in the LEHR collimator which was removed with the ME collimator.

2.4.1.2 Planar System Resolution

The LEHR collimator resulted in better FWHM and FWTM values than the ME collimator for the measured and simulated images. Both collimators showed increased FWHM and FWTM values (i.e., poorer resolution), when increasing the source-detector distance. This was expected due to the design of the collimators.

The measured and simulated FWHM spatial resolution results for the LEHR images compare well, with no difference at 100 mm. Similarly, good agreement was obtained between the measured and simulated FWHM values reported for the ME collimator (respective values of 11.2 mm and 11.9 mm at a source-detector distance of 100mm). These values compared well with literature reported I-123 spatial resolution values for the ME collimator. De Geeter *et al.* (1996) reported a FWHM of 11.1 mm for a Siemens Orbiter 3700 detector fitted with a ME collimator. The simulated FWHM values reported by Morphis *et al.* (2021b) compared well with these results.

The FWTM values showed discrepancies between the measured and simulated results obtained for the LEHR collimator, similar to what was obtained by Morphis *et al.* (2021b) . A difference of up to 12.1% was obtained at a source-detector distance

of 100 mm. Considering the LSFs shown in Figure 2-6c, the tail ends of the LSFs for the LEHR collimator were elevated compared to the ME LSFs. This can be explained by the presence of septal scatter and penetration when imaging I-123 using the LEHR collimator. The presence of septal interaction is slightly different in the simulated images compared to the measured images, confirmed by the percentage differences obtained for the FWTM values. These percentage differences are due to the simulations performed with a constant energy resolution, in addition to assuming a non-linear energy response. This resulted in the incorrect modelling of the energy resolution in the high energy range and the septal penetration is therefore not modelled correctly. The ME collimator showed a better comparison between measured and simulated FWTM results, with a percentage difference not exceeding 7.1%. It should be noted that the measurement of FWTM in the presence of septal scatter and penetration can be challenging and therefore, the FWTM is often not reported in these comparisons (Autret *et al.*, 2005).

Measured and simulated images obtained with the ME collimator show the distinct collimator hole pattern that is not visible with the LEHR collimator.

2.4.1.3 Planar System Sensitivity

The accuracy of the sensitivity calculation is strongly dependent on the accuracy of the dose calibrator. During the sensitivity measurements, a correction factor was incorporated that was obtained from calibration measurements performed by the National Metrology Laboratory of South Africa, and it was found that the dose calibrator underestimated the I-123 activity by 1.4%. This was taken into account when calculating the sensitivity.

The measured and simulated sensitivity values compared well for both the LEHR and ME datasets, with the largest difference (5.3%) obtained for the ME collimator. This difference was comparable to what was found by Morphis *et al.* (2021b) who used a fitted energy resolution model in the simulations. The larger sensitivity values measured and simulated for the LEHR collimator are due to the collimator design. However, between the measured and simulated data, there is only a 2.3% difference. The images show more septal penetration for the LEHR collimator than for the ME collimator, as is expected. The comparison of the sensitivity values between the measured and simulated data is acceptable.

2.4.2 SPECT Image Quality

The reconstructed simulated and measured I-123 LEHR and ME images visually compared well. Minor differences in the measured and simulated images of the cold lesion and hot lesion sections were noted.

In both the LEHR-M and LEHR-S reconstructed images obtained through the cold lesion section, the five largest rods (22.4 mm – 9.2 mm diameter) were visible. The 7.3 mm rod was partially visible in the LEHR-M image but not in the LEHR-S image.

The measured and simulated images obtained of the hot lesion and linearity inserts compared well for both collimator datasets. It is crucial to take into consideration that the voxel-based phantom created from the CT images of the Carlson phantom has resolution limitations that might affect the resolution of the simulated SPECT images.

It can be concluded from the reconstructed simulated I-123 LEHR and ME images shown in Table 2-6 that the gamma camera is well modelled.

2.5 Conclusion

This study shows that the SIMIND MC code can accurately simulate I-123 images obtained with both the LEHR and ME collimators in terms of energy spectra, system spatial resolution, system sensitivity, and realistic source distributions using a fixed energy resolution. The results agreed well with the results obtained by Morphis *et al.* (2021b) who used a fitted energy resolution model for generating the modelled gamma camera in SIMIND. Our simulation model can be deemed validated regarding modelling the intrinsic and extrinsic energy spectra with differences between measured and simulated R_E values of no more than 3.4%. The spatial resolution for both collimators compared well with a maximum percentage difference between measured and simulated FWHM values of 3.2% for the LEHR collimator and 6.4% for the ME collimator. The FWTM values showed a larger difference, but as mentioned before, the calculation of FWTM in the presence of septal scatter and penetration can be challenging. The planar sensitivity results were also acceptable, indicating that evaluation of quantification studies can be conducted with confidence.

Throughout, the measured planar test results presented with an acceptable small standard deviation. Overall, the virtual model of the gamma camera presented to be accurate when simulating planar images with either collimator.

The visual comparisons done between the reconstructed LEHR and ME collimated SPECT images proved to be a suitable method to perform validation of the simulation model.

Based on the good agreement between the measured and simulated results of the planar validation tests and the acceptable visual comparison of the SPECT images, it can be concluded that the SIMIND modelled gamma camera can be used for simulation of I-123 images using the LEHR and ME collimators. Simulated planar and SPECT I-123 images can thus be used for further evaluation of acquisition and processing protocols of typical NM procedures.

2.6 References

Ahn, B. C. (2016) 'Personalized Medicine Based on Theranostic Radioiodine Molecular Imaging for Differentiated Thyroid Cancer', *BioMed Research International*, 2016, pp. 1–9. doi: 10.1155/2016/1680464.

Australian Nuclear Science and Technology Organisation (no date) 'Radioisotopes: Their Role in Society Today', *Australian Nuclear Science and Technology Organisation*. Lucas Heights, NSW, pp. 1–12. Available at: https://apo.ansto.gov.au/dspace/handle/10238/2095.

Autret, D., Bitar, A., Ferrer, L., Lisbona, A. and Bardiès, M. (2005) 'Monte Carlo Modeling of Gamma Cameras for I-131 Imaging in Targeted Radiotherapy', *Cancer Biotherapy and Radiopharmaceuticals*, 20(1), pp. 77–84. doi: 10.1089/cbr.2005.20.77.

Bombardieri, E., Giammarile, F., Aktolun, C., Baum, R. P., Bischof Delaloye, A., Maffioli, L., Moncayo, R., Mortelmans, L., Pepe, G., Reske, S. N., Castellani, M. R. and Chiti, A. (2010) '131I/123I-Metaiodobenzylguanidine (mIBG) scintigraphy: Procedure guidelines for tumour imaging', *European Journal of Nuclear Medicine and Molecular Imaging*, 37(12), pp. 2436–2446. doi: 10.1007/s00259-010-1545-7.

Cherry, S., Sorenson, J. and Phelps, M. (2012) *Physics in Nuclear Medicine*. 4th edn. Edited by L. Barnes, C. Thoms, and D. Scholz. Philadelphia, PA: Elsevier Saunders. doi: 10.1016/C2009-0-51635-2.

Dobbeleir, A. A., Hambÿe, A. S. E. and Franken, P. R. (1999) 'Influence of high-energy photons on the spectrum of iodine-123 with low- and medium-energy collimators: Consequences for imaging with 123 I-labelled compounds in clinical practice', *European Journal of Nuclear Medicine*, 26(6), pp. 655–658. doi: 10.1007/s002590050434.

Ejeh, J. E., van Staden, J. A. and du Raan, H. (2019) 'Validation of SIMIND Monte Carlo Simulation Software for Modelling a Siemens Symbia T SPECT Scintillation Camera', in *World Congress on Medical Physics and Biomedical Engineering*.

Springer Singapore, pp. 573–576. doi: 10.1007/978-981-10-9035-6.

Fleming, J. S., Goatman, K. A., Julyan, P. J., Boivin, C. M., Wilson, M. J., Barber, R. W., Bird, N. J. and Fryer, T. D. (2000) 'A comparison of performance of three gamma camera systems for positron emission tomography', *Nuclear Medicine Communications*, 21(12), pp. 1095–1102. doi: 10.1097/00006231-200012000-00002.

Fluke Biomedical (2005) 'Nuclear Associates 76-823, 76-824 & 76-825 PET/SPECT Phantom Source Tank, Phantom Inserts and Cardiac Insert', *Manual*, p. 10. Available at: https://www.manualsdir.com/manuals/767906/fluke-biomedical-76-823.html.

Frangos, S. and Buscombe, J. R. (2019) 'Why should we be concerned about a "g"?', *European Journal of Nuclear Medicine and Molecular Imaging*. European Journal of Nuclear Medicine and Molecular Imaging, 46(519), p. 1. doi: 10.3345/cep.2020.00521.

Frey, E. C., Humm, J. L. and Ljungberg, M. (2012) 'Accuracy and Precision of Radioactivity Quantification in Nuclear Medicine Images', *Seminars in Nuclear Medicine*, 42(3), pp. 208–218. doi: 10.1053/j.semnuclmed.2011.11.003.Accuracy.

Frey, E. and Tsui, B. (1993) 'A Practical Method for Incorporating Scatter in a Projector-Backprojector for Accurate Scatter Compensation in SPECT', *IEEE Transactions on Nuclear Science*, 40(4), pp. 1107–1116. Available at: https://ieeexplore.ieee.org/stamp/stamp.jsp?arnumber=256720&casa_token=P-bf4OL6AioAAAAA:rAOxSR_pYwOPBXGBN4NwDFOITIJPxaJ7EFwJdmXW6V2zZQ57KjRawkkZ6E-rf7mVY5ES4oGB5Vif&tag=1.

De Geeter, F., Franken, P. R., Defrise, M., Andries, H., Saelens, E. and Bossuyt, A. (1996) 'Optimal collimator choice for sequential iodine-123 and technetium-99m imaging', *European Journal of Nuclear Medicine*, 23(7), pp. 768–774. doi: 10.1007/BF00843705.

Gerson, M. C., Dwivedi, A. K., Abdallah, M., Shukla, R. and Jacobson, A. F. (2013) 'Significance of I-123 metaiodobenzylguanidine (123I-MIBG) lung activity in subjects with heart failure in comparison to healthy control subjects', *Journal of Nuclear Cardiology*, 20(4), pp. 592–599. doi: 10.1007/s12350-013-9714-2.

Hakimabad, H. M., Panjeh, H. and Vejdani-Noghreiyan, A. (2007) 'Evaluation the nonlinear response function of a 3×3 in NaI scintillation detector for PGNAA applications', *Applied Radiation and Isotopes*, 65(8), pp. 918–926. doi: 10.1016/j.apradiso.2007.03.014.

Hudson, H. M. and Larkin, R. S. (1994) 'Accelerated Image Reconstruction Using Ordered Subsets of Projection Data', *IEEE transactions on medical imaging*, 13(4), pp. 601–609. Available at: https://ieeexplore.ieee.org/stamp/stamp.jsp?arnumber=363108&casa_token=T7Z-tI9VOLgAAAAA:y9ErK3Qs71X7dUsn8p4bkR1NOKQwLPgTmfeA27UxiYTfVq7midHvXeaqnH4d5kwOT66GrlO7G1a5&tag=1.

Laboratoire National Henri Becquerel (2004) *Table de Radionucléides - I-123*.

Available at: http://www.lnhb.fr/nuclides/I-123_tables.pdf (Accessed: 5 November 2018).

Laboratoire National Henri Becquerel (2014) *Table de Radionucléides - I-131*. Available at: http://www.lnhb.fr/nuclides/I-131_tables.pdf (Accessed: 20 November 2020).

Ljungberg, M. and Strand, S.-E. (1989) 'A Monte Carlo program for the simulation of scintillation camera characteristics', *Computer Methods and Programs in Biomedicine*, 29, pp. 257–272. doi: 10.1016/0169-2607(89)90111-9.

Ljungberg, M., Strand, Sven Erik and King, M. A. (2012) *Monte Carlo Calculations in Nuclear Medicine: Applications in Diagnostic Imaging*. 2nd edn. Edited by M. Ljungberg and S E Strand. Taylor & Francis.

Macey, D. J., Denardo, G. L., Denardo, S. J. and Hines, H. H. (1986) 'Comparison of Low- and Medium-Energy Coffimators for SPECT Imaging with Iodine-123-Labeled Antibodies', *Journal of Nuclear Medicine*, 27, pp. 1467–1475. Available at: https://jnm.snmjournals.org/content/jnumed/27/9/1467.full.pdf.

Matthay, K. K., Shulkin, B., Ladenstein, R., Michon, J., Giammarile, F., Lewington, V., Pearson, A. D. J. and Cohn, S. L. (2010) 'Criteria for evaluation of disease extent by 123 I-metaiodobenzylguanidine scans in neuroblastoma: A report for the International Neuroblastoma Risk Group (INRG) Task Force', *British Journal of Cancer*. Nature Publishing Group, 102(9), pp. 1319–1326. doi: 10.1038/sj.bjc.6605621.

Morphis, M., van Staden, J. A, du Raan, H. and Ljungberg, M. (2021a) 'Modelling of energy-dependent spectral resolution for SPECT Monte Carlo simulations using SIMIND', *Heliyon*. Elsevier Ltd, 7(January), p. e06097. doi: 10.1016/j.heliyon.2021.e06097.

Morphis, M., van Staden, J. A., du Raan, H. and Ljungberg, M. (2021b) 'Validation of a SIMIND Monte Carlo modelled gamma camera for Iodine-123 and Iodine-131 imaging', *Heliyon*. Elsevier Ltd, 7(6), p. e07196. doi: 10.1016/j.heliyon.2021.e07196.

Nakajima, K., Verschure, D. O., Okuda, K. and Verberne, H. J. (2017) 'Standardization of 123I-meta-iodobenzylguanidine myocardial sympathetic activity imaging: phantom calibration and clinical applications', *Clinical and Translational Imaging*. Springer Milan, 5(3), pp. 255–263. doi: 10.1007/s40336-017-0230-2.

National Electrical Manufacturers Association (2012) *NEMA Standards Publication NU 1-2012: Performance Measurements of Gamma Cameras*. 7th edn. Virginia: National Electrical Manufacturers Association.

Parisi, M. T., Eslamy, H., Park, J. R., Shulkin, B. L. and Yanik, G. A. (2016) 'I-131-Metaiodobenzylguanidine Theranostics in Neuroblastoma: Historical Perspectives; Practical Applications', *Seminars in Nuclear Medicine*. Elsevier, 46(3), pp. 184–202. doi: 10.1053/j.semnuclmed.2016.02.002.

Ramonaheng, K., van Staden, J. A., du Raan, H. and du Raan, H. (2020) 'Validation of a Monte Carlo modelled gamma camera for Lutetium-177 imaging', *Applied Radiation and Isotopes*. Elsevier Ltd, 163, pp. 1–9. doi: 10.1016/j.apradiso.2020.109200.

Rault, E., Staelens, S., Van Holen, R., De Beenhouwer, J. and Vandenberghe, S. (2011) 'Accurate Monte Carlo modelling of the back compartments of SPECT cameras', *Physics in Medicine and Biology*, 56, pp. 87–104. doi: 10.1088/0031-9155/56/1/006.

Rault, E., Vandenberghe, S., Van Holen, R., De Beenhouwer, J., Staelens, S. and Lemahieu, I. (2007) 'Comparison of Image Quality of Different Iodine Isotopes (I-123, I-124, and I-131)', *Cancer Biotherapy and Radiopharmaceuticals*, 22(3), pp. 423–430. doi: 10.1089/cbr.2006.323.

Rodrigues, S., Tome, B., Abreu, M. C., Santos, N., Mendes, P. R. and Peralta, L. (2007) 'Monte Carlo Simulation and Experimental Characterization of a Dual Head Gamma Camera', pp. 1–11. Available at: http://arxiv.org/abs/0711.2577 [physics.med-ph].

Sadremomtaz, A. and Taherparvar, P. (2013) 'The influence of filters on the SPECT image of Carlson phantom', *Journal of Biomedical Science and Engineering*, 06(03), pp. 291–297. doi: 10.4236/jbise.2013.63037.

Schneider, C. A., Rasband, W. S. and Eliceiri, K. W. (2012) 'NIH Image to ImageJ : 25 years of image analysis', *Nature Methods*. Nature Publishing Group, 9(7), pp. 671–675. doi: 10.1038/nmeth.2089.

Siemens Healthcare (2013) *Symbia T Series System Specifications*. Available at: http://www.edgemedicalsolutions.in/sym t.pdf.

Silberstein, E. B. (2012) 'Radioiodine: The classic theranostic agent', *Seminars in Nuclear Medicine*. Elsevier Inc., 42(3), pp. 164–170. doi: 10.1053/j.semnuclmed.2011.12.002.

Sjögreen, K., Ljungberg, M., Wingårdh, K., Minarik, D. and Strand, S. (2005) 'The LundADose Method for Planar Image Activity Quantification and Absorbed-Dose Assessment in Radionuclide Therapy', *Cancer Biotherapy & Radiopharmaceuticals*, 20(1), pp. 92–97. Available at: https://books.google.co.za/books?id=YzzNBQAAQBAJ&dq=Monte+Carlo+calculations+in+nuclear+medicine&lr=.

Tang, H. R., Silva, A. J. Da, Matthay, K. K., Price, D. C., Huberty, J. P., Hawkins, R. A. and Hasegawa, B. H. (2000) 'Neuroblastoma Imaging Using a Combined CT Scanner – Scintillation Camera and I131-MIBG', pp. 237–248. Available at: http://jnm.snmjournals.org/content/42/2/237.short.

Toossi, M. T. B., Islamian, J. P., Momennezhad, M., Ljungberg, M. and Naseri, S. H. (2009) 'SIMIND Monte Carlo simulation of a single photon emission CT', *Journal of*

Medical Physics, 35(1), pp. 42–47. doi: 10.4103/0971-6203.55967.

Yeong, C. H., Cheng, M. hua and Ng, K. H. (2014) ‘Therapeutic radionuclides in nuclear medicine: Current and future prospects’, *Journal of Zhejiang University: Science B*, 15(10), pp. 845–863. doi: 10.1631/jzus.B1400131.

Yordanova, A., Eppard, E., Kürpig, S., Bundschuh, R. A., Schönberger, S., Gonzalez-carmona, M. and Feldmann, G. (2017) ‘Theranostics in nuclear medicine practice’, *OncoTargets and Therapy*, (October), pp. 4821–4828.

Zaidi, H. (1999) ‘Relevance of accurate Monte Carlo modeling in nuclear medical imaging Addendum to “Relevance of accurate Monte Carlo modeling in nuclear medical imaging Relevance of accurate Monte Carlo modeling in nuclear medical imaging”’, *Medical Physics*, 26(816), pp. 2566–574. doi: 10.1118/1.598945.

Chapter 3: Paper 2

Optimisation of I-123 SPECT Image Reconstruction using LEHR and ME Collimators: A Monte Carlo study

Table of Content

Abstract

The study aimed to optimise the reconstruction of Monte Carlo I-123 SPECT studies acquired with LEHR and ME collimators. Firstly, the OSEM SPECT reconstruction parameters were optimised in terms of count density recovery, image noise, contrast and resolution. Secondly, the influence of different SPECT corrections (attenuation, scatter, geometric collimator-detector response (CDR) and CDR including septal scatter and penetration) was evaluated. The image quality parameters noise and contrast were quantitatively analysed, whereas resolution was qualitatively analysed. The reconstruction variables in this study were the number of iterations and the combinations of SPECT corrections. A validated SIMIND MC gamma camera model was used to simulate I-123 images of spheres ranging in size from 15 mm to 60 mm in a water-filled phantom, as well as a Carlson image quality phantom. All simulations were performed with LEHR and ME collimators. The sphere projections were reconstructed with an increasing number of effective iterations (keeping a constant number of subsets) to evaluate the recovery of the count density for the two collimators. The image quality phantom was reconstructed with varying equivalent iterations (EI) and SPECT corrections (attenuation, scatter and collimator-detector response) to optimise the image quality for both LEHR and ME collimators.

More than 90% count density recovery was obtained with 64 EI for both collimator datasets and spheres of 45mm and 60mm diameters. The *%Recovery* and noise reached convergence for all spheres at 64 EI. By implementing CT-based attenuation, scatter, and CDR corrections along with the 64 EI, the image quality of LEHR and ME images were equivalent, with a $\%RMS$ and contrast difference of 0.8% and 1.8%, respectively.

3.1 Introduction

Theragnostics in Nuclear Medicine (NM) (Frangos and Buscombe, 2019) is the process when a diagnostic agent is applied as a surrogate for a therapeutic agent (Ahn, 2016). It has been decided, quite recently, to use the standard term "radiopharmaceutical therapy" (RPT) when referring to theragnostics, molecular radiotherapy or similar forms of treatment (Wahl, Ahuja and Clarke, 2021). This emerging field of medicine is invaluable for the advancement of personalised medicine; it enables the localisation of the disease, helps determine if a patient will

benefit from the planned treatment, and monitors the patient's response to treatment (Yordanova *et al.*, 2017). By directly targeting the malignant cells with the radiopharmaceutical, the associated radiation risks to the patient and the medical costs related to the therapy may be reduced.

The diagnostic and therapeutic agents used in RPT are usually the same pharmaceutical labelled to isotopes of the same element, such as iodine-123 (I-123) and iodine-131 (I-131). Iodine radioisotopes are often labelled with metaiodobenzylguanidine (mIBG) to evaluate neuroendocrine tumours (Bombardieri *et al.*, 2010). Studies have also shown that I-123 mIBG is useful in the diagnosis and prognosis of cardiac illness (Chen *et al.*, 2006). With the increased use of these iodine radioisotopes for theragnostic purposes, accurate image quantification is vital to attain accurate dosimetry.

I-123 is frequently used for single-photon emission computed tomography (SPECT). It decays by electron capture and emits 159.0 keV gamma rays with an 83.3% abundance, which is well suited for gamma camera imaging. I-123 has characteristic x-ray emissions ranging from 27.2 keV to 31.8 keV and some low-abundance of high-energy gamma emissions present at 440.0 – 624.6 keV (2.4% abundance) and 628.3 – 783.6 keV (0.1% abundance) (Laboratoire National Henri Becquerel, 2004) The radionuclide's half-life of 13.2 hours makes it ideal for thyroid uptake imaging, keeping to the 24-hour imaging time-point. I-123 also has a significantly reduced radiation burden compared to I-131, primarily due to the lack of β^-emissions (Matthay *et al.*, 2010). SPECT studies using I-123, with its primary 159 keV photon emission, have shown that acquiring projection images with either the low-energy high resolution (LEHR) or medium-energy (ME) collimator is viable. However, acquired images have distinct characteristics; the LEHR collimator produces images with higher resolution (Macey *et al.*, 1986; Dobbeleir, Hambÿe and Franken, 1999; Rault *et al.*, 2007), while the ME collimated images have superior quantitative accuracy due to the collimator's thicker septa, which reduces penetration from the high energy emissions (440.0 – 624.6 keV) (De Geeter *et al.*, 1996). The choice of the collimator can depend on the clinical need, the type of study that needs to be performed (Brown, 2018) and the resources at hand.

The two-dimensional SPECT projection images are reconstructed to create 3D images, which add a depth factor to the radioactivity distribution (Bruyant, 2002). One widely used reconstruction algorithm is the iterative ordered subset expectation maximization (OSEM) algorithm (Hudson and Larkin, 1994). OSEM can compensate for the physical image degrading factors such as attenuation (Frey, Humm and Ljungberg, 2012), Compton scatter and CDR (Frey and Tsui, 1996; Ogawa, 2004; Söderberg *et al.*, 2012). These image degrading factors influence the quantitative information obtained from the SPECT images; thus, the factors must be adequately corrected for.

CDR can compensate for the geometric response of the detector as well as collimator septal penetration and scatter using pre-calculated kernels simulated with Monte Carlo (MC) software. CDR kernels are obtained by simulating a point-source in air at various distances from the detector and collimator (Minarik, Sjögreen Gleisner and Ljungberg, 2008).

Another critical factor to consider during OSEM reconstruction is the number of equivalent iterations (EI) (subset × iterations), also referred to as OSEM updates, used. The reconstructed image is updated after a single subset (grouping) of projections has been processed. Once all subsets have been processed (i.e. multiple updates of the reconstructed image have taken place), a single iteration has been performed (Hudson and Larkin, 1994; Hesse *et al.*, 2005; Söderberg *et al.*, 2012). The number of subsets determines the reconstruction time, and the number of equivalent iterations determines image quality components such as noise and contrast (Hutton, Hudson and Beekman, 1997; Leong, Kruger and O'Connor, 2001; Brambilla *et al.*, 2005). Using a low number of iterations will result in images with lower noise levels but with poor contrast (Seret, 2006). The number of EI have to be selected carefully by considering the imaging study and the clinical scenario (i.e., computation strength, available time).

Hesse *et al.* (2005) has stated that a minimum of two iterations is viable for OSEM reconstructions. Seret (2006) concurred with the sentiment and recommended that eight subsets be used when it comes to myocardial perfusion imaging. Hawman *et al.* (2014) stated that the number of subsets used during OSEM reconstruction should be less than a quarter of the number of projections. In an I-123 study by Niñerola-Baizán

et al. (2018), eight subsets with iterations ranging from 1 to 30 were used in dopaminergic neurotransmission SPECT studies.They proposed that an EI ranging between 48 and 128 should be used. An EI number must be selected to balance the processing time and the noise present in the final images. To summarise, optimising the reconstruction parameters (EI) of I-123 SPECT images acquired with either the LEHR or ME collimators makes it possible to find equal ground between image quality and quantification accuracy. Performing optimisation of image reconstruction requires that several scenarios and phantoms be analysed. MC simulation is a useful tool for such a study since the acquisition of multiple phantom studies and handling of radioactivity can be limited. A variety of activity concentrations and phantom geometries can easily be mimicked with MC simulation studies.

MC simulation studies have been established as a reliable tool for medical physicists to use in the research domain of NM. The applications of MC simulations have steadily increased since an article was published in 1976 (Raeside, 1976), which expanded on the principles of MC simulations and applications in medical physics. With modern computational strength, the growth in the interest of applying MC simulations in NM imaging problem solving has been exponential. MC techniques have been used extensively to simulate random processes (interactions) and quantify parameters that are otherwise too difficult/impossible to calculate through experimental measures (Zaidi, 1999). MC simulations can accurately model the stochastic nature of radiation emissions, the transport of radiation through matter, and the detection of emissions by a tomographic system. Authors have used MC codes to characterise the design of gamma camera collimators (Macey *et al.*, 1986; Razavi *et al.*, 2017), assess SPECT and planar image quality (Rault *et al.*, 2007; Holen, Vandenberghe and Staelens, 2008) and evaluate the role of various corrections on quantification accuracy (Ljungberg and Strand, 1990; Dewaraja *et al.*, 2002; Kalantari, Rajabi and Saghari, 2011; Kangasmaa, Sohlberg and Kuikka, 2011; Asl, Sadremomtaz and Bitarafan-Rajabi, 2013). MC simulations have also been incorporated to optimise acquisition and reconstruction parameters (Brown, 2018) of SPECT images.

The purpose of this study was to optimise and compare the OSEM iterative reconstruction algorithm for I-123 LEHR and ME collimated SPECT images using MC studies. Two objectives were identified to achieve this aim: (i) The OSEM SPECT reconstruction parameters were optimised in terms of count density recovery, image

noise, contrast and resolution. (ii) The influence of SPECT corrections on LEHR and ME I-123 images was evaluated by comparing the image quality of LEHR and ME SPECT corrected images.

3.2 Materials and Methods

Version 6.1 of SIMIND MC code was used to create a virtual model of the Siemens Symbia gamma camera located at Universitas Academic Hospital (Bloemfontein, South Africa). The simulation parameters and gamma camera design were identical to those used and validated in **Chapter 2**. All images in this study were simulated using the SIMIND MC software.

Voxel-based digital models were created by segmenting pre-acquired CT images (5 mm slice thickness) of a water-filled cylindrical Carlson phantom (internal diameter: 203 mm and height: 318 mm) (Fluke Biomedical, 2005), as explained by Ramonaheng *et al.* (2020). A registered attenuation map was derived from the CT data of the phantom and used to correct for photon attenuation in the SPECT image.

Spheres with volumes (and their corresponding diameters) of 1.8 ml (15 mm), 14.1 ml (30 mm), 47.7 ml (45 mm) and 113.1 ml (60 mm) were digitally added individually to the segmented cylinder phantom using ITK Snap (Yushkevich *et al.*, 2006) to generate four digital voxel-based models (see Figure 3-1). These will be referred to as the ***Cylinder phantoms***.

Secondly, a digital voxel-based model of the cylindrical Carlson phantom (Fluke, 2005) with specifically designed inserts to evaluate image quality was also used in this study (Figure 3-2). The Carlson phantom was designed for periodic performance testing of SPECT and PET systems (Fleming *et al.*, 2000; Sadremomtaz and Taherparvar, 2013). In this study, we will refer to the digital voxel-based model of the Carlson phantom with all fitted inserts as the ***Image quality (IQ) phantom***.

SPECT projection images of the four *Cylinder phantoms*, each with a different sphere size, and the *IQ phantom* were simulated for I-123 using the LEHR and ME collimator sets incorporated in the validated SIMIND gamma camera model. A 15% energy window was centred over the 159 keV photopeak, and a standard imaging acquisition protocol was used to set up the simulation parameters for SIMIND. Poisson noise was

added during simulations, and the projections were simulated with a high number of histories (> 1 billion).

The simulated SPECT projection images were reconstructed using a software package developed at Lund University (Sjögreen *et al.*, 2005). The software employs the OSEM iterative reconstruction as discussed before, and includes a CT-based density map attenuation correction, ESSE scatter correction and a CDR correction compensating for the detector's geometric response, as well as septal penetration and scatter.

The reconstructed images were analysed using the public domain software *Amide* (Loening and Gambhir, 2003) to obtain image count statistics such as mean, total and standard deviations of the count density, as well as the number of fractional voxels in a volume of interest (VOI). The software, *Amide*, assigns a weight to each voxel determined by its contribution to the total VOI, and the sum of the voxel weights is then referred to as fractional voxels in the VOI.

3.2.1 Optimisation of OSEM Reconstruction Parameters

An optimised image reconstruction protocol is required for accurate image quantification. In this study, the influence of the OSEM reconstruction parameters (number of EI) on image count density recovery, as well as percentage root mean square ($\%RMS$) as a measure of image noise was determined for reconstructed MC simulated images of the Cylinder phantom with radioactive spheres in a cold background. Furthermore, the *IQ phantom* was used to evaluate the influence of the number of EI and different correction algorithms on the following image quality parameters: uniformity, contrast, resolution, and linearity.

3.2.1.1 Recovery of Spherical Source Count Density in the Cylindrical Phantom

I-123 activity (0.17 MBq/ml) was allocated to each sphere in the four *Cylinder phantoms* (Gilland *et al.*, 1994). SPECT images (64 projections) were simulated in step-and-shoot mode with a non-circular orbit of rotation (Todd-Pokropek, 1983), an equivalent of 40 seconds acquisition time per projection was used, a matrix size of 128 × 128 and pixel size of 4.8 × 4.8 mm^2. The acquisition setup is shown in Figure

3-1. The SPECT projections were simulated for each of the four phantoms using both the LEHR and ME collimators.

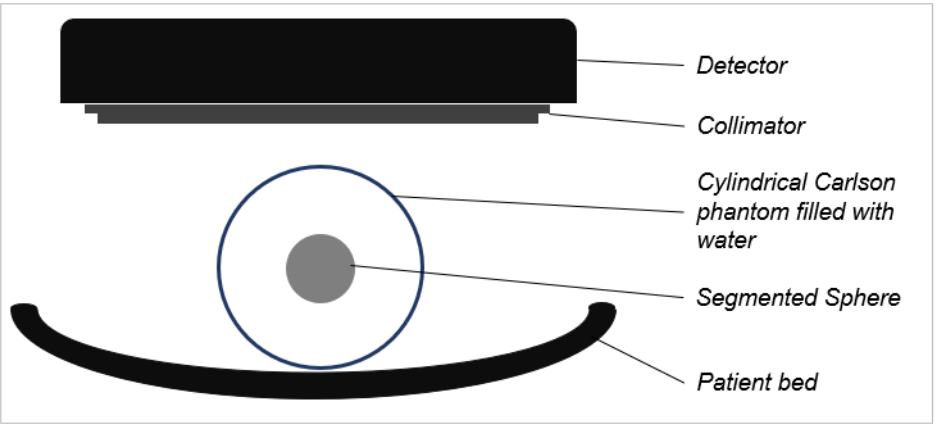

Figure 3-1: *Acquisition setup of the cylindrical phantom*

The sphere datasets were reconstructed using the OSEM iterative reconstruction algorithm as discussed. Attenuation, scatter and full CDR corrections were incorporated as part of the reconstruction process,

A series of reconstructed datasets were created for each phantom and collimator, with a fixed number of subsets (eight) and a varying number of iterations (ranging from 2 to 10). This resulted in the number of EI ranging from 16 to 80. A fixed number of subsets was used as proposed by Matsutomo *et al.* (2015).

VOIs corresponding to the physical size of each sphere was used to obtain the count statistics with *Amide*. The recovery of the count density was calculated using equation (3-1),

$$Recovery = \frac{mean \times fractional\ voxel}{volume\ (ml)} \qquad (3\text{-}1)$$

with $mean$ referring to the mean count density in the VOI, $fractional\ voxel$ as defined before and $volume$, the known volume of the sphere. The $Recovery$ was normalised to the overall maximum value obtained across all VOI sizes (Ljungberg *et al.*, 2016) and reported as "percentage recovery" (*%Recovery*).

Typically, noise is evaluated by assessing the change in the noise level within a uniform area of a single slice, using the $\%RMS$ (Leong, Kruger and O'Connor, 2001; Brambilla *et al.*, 2005). However, Ramonaheng *et al*. (2021) evaluated the change in noise due to inherent OSEM probabilities by comparing the $\%RMS$ values obtained

for spherical objects. As proposed by Ramonaheng *et al*. (2021), the noise levels in each sphere were evaluated using the $\%RMS$ defined in equation *(3-2)*. Morphis *et al.* (2021) used the term relative standard deviation instead of $\%RMS$.

$$\%RMS = \frac{StdDev}{mean} \times 100 \qquad (3\text{-}2)$$

In equation *(3-2)* $StdDev$ and $mean$ are the standard deviation and mean count density of the reconstructed counts within the spherical VOI. As indicated by Sjögreen *et al.* (1996), the $\%RMS$ is an estimate of reconstructed noise and should not be considered as a true representation of noise in an image. The OSEM SPECT reconstruction algorithm used in this study includes a CDR correction which results in so-called Gibbs artefacts (Liu and Farncombe, 2007; Kangasmaa, Sohlberg and Kuikka, 2011), which will influence the $\%RMS$ values (Ljungberg *et al.*, 2016; Morphis *et al.*, 2021).

The normalised recovered counts and the $\%RMS$ values were plotted as a function of the EI per sphere size for both collimators (LEHR and ME).

3.2.1.2 Image Quality Phantom

Image quality was evaluated as part of the optimisation of the OSEM reconstruction algorithm using the Carlson phantom with the image quality inserts (*IQ phantom*). The three inserts, each designed to test a feature of image quality, is shown in Figure 3-2 (Fluke Biomedical, 2005).

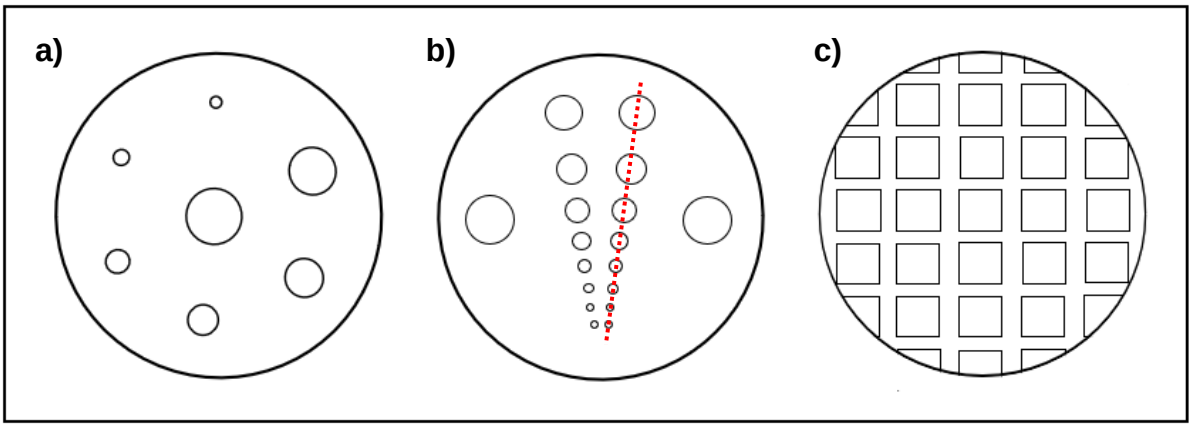

Figure 3-2: *Diagrams of the superior view of three Carlson inserts: (a) cold lesion contrast insert, (b) hot lesion resolution insert and (c) linearity insert*

The IQ phantom was described in **Chapter 2**. The SPECT cold contrast was evaluated using insert (a) by calculating the contrast of the largest rod (22.4 mm diameter) in the

centre of the phantom. With the second insert (b), the system's spatial resolution was evaluated qualitatively by comparing the detectability of the nine hot hole pairs (4.7, 5.9, 7.3, 9.2, 11.4, 14.3, 17.9, 22.4 and 38.5 mm) in a cold background. The third insert (c), consisting of a 50.8 mm thick acrylic block with a crossed grid of channels cut 38.1 mm deep into a square pattern enabled us to assess the linearity of the SPECT images. The insert-free area in the IQ phantom was used to assess the SPECT uniformity qualitatively.

SPECT projections of the *IQ phantom* were simulated with an equivalent of 833.3 MBq of activity (I-123) and an acquisition time of 120 s per projection to ensure good count statistics. A 15% energy window was centred over the 159 keV I-123 photopeak. The same imaging parameters were used in the simulation as for the cylinder phantom (i.e., 64 SPECT projections, matrix size of 128 × 128, step-and-shoot mode with a non-circular orbit of rotation). Two SPECT projection datasets were simulated using the modelled Siemens Symbia gamma camera fitted with a LEHR and ME collimator respectively.

The *IQ phantom* projections were processed using the same reconstruction procedure as described above for the *Cylindrical phantoms*. Reconstructed datasets were therefore generated for the different EI, ranging from 16 to 80, for each collimator. For each dataset, five consecutive reconstructed slices were summed in each section of the phantom (uniform, cold lesion, warm lesion and linearity sections) to provide good count statistics in the images for comparison and evaluation. Each section of the reconstructed datasets was analysed, and the following parameters were reported: uniformity, contrast, resolution, and linearity.

i Uniformity Section

A five-pixel wide intensity profile was drawn across the summed reconstructed slices through the uniform section of the *IQ phantom* for the different OSEM EI reconstruction datasets to obtain line spread functions (LSFs) for evaluation of the uniformtiy. These LSFs were plotted on a graph for each collimator and visually compared with one another.

A circular region of interest (ROI) with a diameter of 75% of the physical phantom was drawn centrally on the summed reconstructed images. The $\%RMS$ value in each of the ROIs for the different reconstruction datasets was calculated using equation *(3-2)*.

ii Cold Lesion Contrast Insert

A two-pixel wide intensity profile was drawn across the summed image where the cold rods were visible to evaluate the ***cold lesion contrast*** in the images. The profile was drawn to intersect the largest rod (diameter 22.4 mm) in the centre of the image, excluding all the other rods. This was repeated for the different OSEM EI reconstruction datasets for both collimators and the LSFs were plotted and compared.

Cold contrast for the largest rod was calculated using equation *(3-3)* (IAEA, 2009). A small circular ROI (diameter = 3 pixels) was drawn on the cold rod to obtain the mean count density over the cold rod (R_{mean}). The ROI was copied to the warm surroundings and the background activity-filled area's mean count density (B_{mean}) was calculated.

$$contrast\ (\%) = \frac{(B_{mean} - R_{mean})}{(B_{mean} + R_{mean})} \times 100 \qquad (3\text{-}3)$$

iii Hot Lesion Resolution Insert

For the hot lesion ***resolution*** evaluation, a two-pixel wide intensity profile was drawn across the summed slices of the hot lesion insert through the radioactive regions formed by the eight hole-pairs visible in the V-pattern (see dashed line in Figure 3-2 b). The profiles obtained for the different OSEM update reconstruction datasets were compared graphically to evaluate the resolution qualitatively.

iv Linearity Insert

The summed slices of the linearity section of the IQ phantom were visually compared for the different OSEM EI reconstruction datasets.

Based on the results obtained from the count recovery and image quality parameters an optimal EI reconstruction combination was selected and used in the next section of the study.

3.2.2 Influence of SPECT Corrections on Image Quality

The images simulated with the Carlson *IQ phantom* were reconstructed using the OSEM iteration and subset combination as recommended from the results obtained in section 3.2.1. The image reconstruction was repeated four times for each collimator dataset, incorporating the different correction techniques to demonstrate the effect of each correction on the images. The image reconstruction was performed with (i) only the CT-based attenuation correction (A); (ii) the attenuation and ESSE scatter

corrections (A-S); (iii) the attenuation, scatter and geometric CDR corrections (A-S-Geo) and (iv) the attenuation, scatter and CDR corrections taking into consideration the geometric effect, as well as collimator septal penetration and scatter (A-S-CDR). The images were analysed for the different phantom sections as indicated in section 3.2.1.2. Results obtained for the LEHR and ME datasets were compared.

3.3 Results

3.3.1 Optimisation of OSEM Reconstruction Parameters

3.3.1.1 Recovery of Spherical Source Count Density in the Cylindrical Phantom

To establish the relationship between the number of EI used in the OSEM reconstruction and the effects on recovered count density in the OSEM reconstruction, the change in *%Recovery* and $\%RMS$ was measured inside each sphere as a function of increasing EI. The *%Recovery* and $\%RMS$ values for the different sphere sizes were plotted as a function of the EI used in the OSEM reconstruction of the different datasets (Figure 3-3). Figure 3-3(a) and Figure 3-3(b) show the results for the hot spheres in a cold background for the LEHR and ME collimator datasets, respectively. The vertical

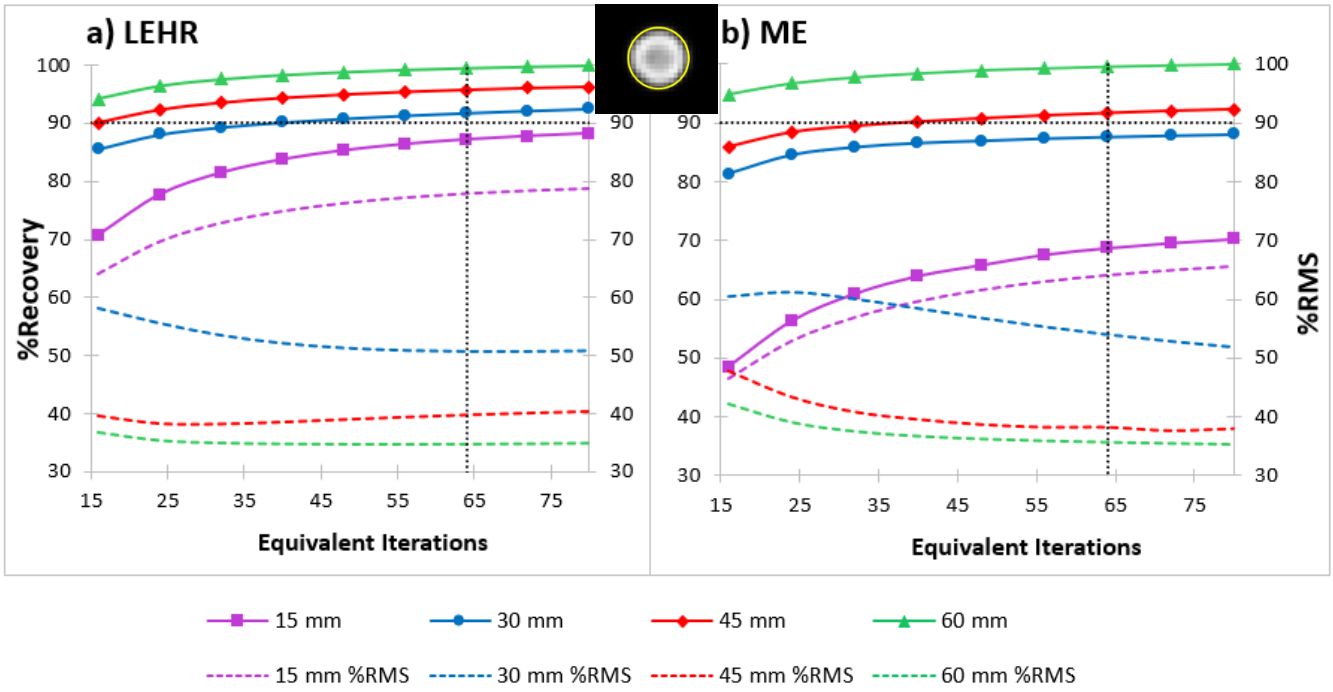

Figure 3-3: *Percentage recovered count density (%Recovery) (solid lines) and Percentage root mean square (%RMS) (dashed lines) as function of OSEM equivalent iterations for (a) the LEHR and (b) the ME collimator. Results are shown for different sphere diameters filled with activity in a cold background. Inserted image shows ROI placement.*

dashed lines in Figure 3-3 a) and b) indicate the optimised number of effective iterations.

Figure 3-3 shows that the *%Recovery* for the three largest spheres reaches convergence (approaching an asymptote) faster than the smallest sphere. For the LEHR dataset (Figure 3-3a), 16 EI results in more than 90.0% count recovery for the 45 mm and 60 mm diameter spheres. Figure 3-3a also shows that the 30 mm sphere achieves a 90.2% recovery at 40 EI, whereas the 15 mm sphere only reaches a maximum of 88.2% at the highest number of EI (80).

In the ME dataset, only the 60 mm diameter sphere has more than 90% recovery at 16 EI (Figure 3-3b). The 45 mm sphere in the ME collimator data recovers 90.2% at 40 EI while the 30 mm and 15 mm spheres recover a maximum of 88.0% and 70.3%, respectively, at 80 EI.

Literature states that with an increase in the number of iterations, the noise in the image will also increase (Brambilla *et al.*, 2005; Seret, 2006; Dewaraja *et al.*, 2012). Therefore, the $\%RMS$ values were also investigated. The LEHR and ME datasets indicate that the $\%RMS$ for the 45 mm and 60 mm spheres steadily decrease as the EI increase (Figure 3-3). At 80 EI the $\%RMS$ for the 60 mm sphere is 35% for both of the LEHR and ME datasets. The 45 mm sphere has a $\%RMS$ value of 40.5% (LEHR) and 38.0% (ME) after 80 EI. In Figure 3-3a the $\%RMS$ of the LEHR 30 mm sphere follows the same declining trend as the two larger spheres of the same dataset, though at a higher level (the $\%RMS$ value decreases from 58% to 51% when moving from 16 to 80 EI). Figure 3-3b shows the 30 mm sphere's $\%RMS$ value for the ME collimator also displays a decreasing trend for the $\%RMS$. The $\%RMS$ for the 30 mm sphere decreases from 61.4% (24 EI) to 52.0% (80 EI) (Figure 3-3b). The smallest sphere (15 mm) shows an increase in $\%RMS$ with an increase in the EI for both collimators (maxima of 78.8% and 65.7% for LEHR and ME, respectively). For the LEHR spheres using more than 64 EI during the reconstruction process would increase the count recovery by only 0.8% for the three largest spheres (1.6% increase in $\%RMS$ for the 45 mm sphere) and 1.2% for the 15 mm sphere (an increase of 1.1% in $\%RMS$).

Similar trends can also be seen for the ME data; the 60 mm sphere had only 0.4% increase in the count recovery, and a 1.0% reduction in the $\%RMS$ when increasing

the EI from 64 to 80. The difference for the 45 mm sphere was a 0.7% increase in count recovery and 0.6% reduction in $\%RMS$. When increasing the EI from 64 to 80, the 30 mm sphere had a 0.5% increase in the *%Recovery* with a 2.4% increase in $\%RMS$.

In summary, for the LEHR and ME datasets increasing the EI value beyond 64 does not improve count recovery by more than 0.8% for the three largest spheres, and by 2.2% for the smallest sphere.

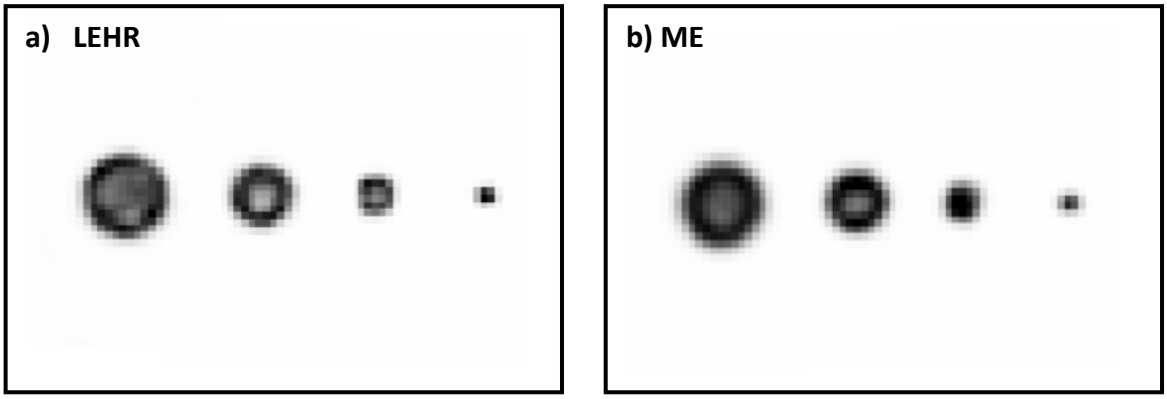

Figure 3-4*: Examples of Gibbs artefacts present in the reconstructed (64 EI) transverse slice of the 60 mm, 45 mm, 30 mm and 15 mm diameter spheres for (a) the LEHR and (b) ME collimators.*

From Figure 3-4a and 3-4b, it can be seen that the Gibbs ringing artefact is present in the images of the 45 mm and 60 mm spheres for both collimator datasets, as well as in the image of the 30 mm LEHR sphere (Figure 3-4a). The Gibbs ringing artefact is, however, absent on the smaller spheres (30 mm for ME and 15 mm for both collimators). This could be attributed to the limited spatial resolution of the gamma camera and a merging of the increased activity on the edges of the smaller spheres (Kangasmaa, Sohlberg and Kuikka, 2011).

3.3.1.2 Image Quality Phantom

i Uniformity Section

Figure 3-5 shows the LSFs obtained across the reconstructed images of the uniform section in the phantom obtained for different numbers of OSEM EI.

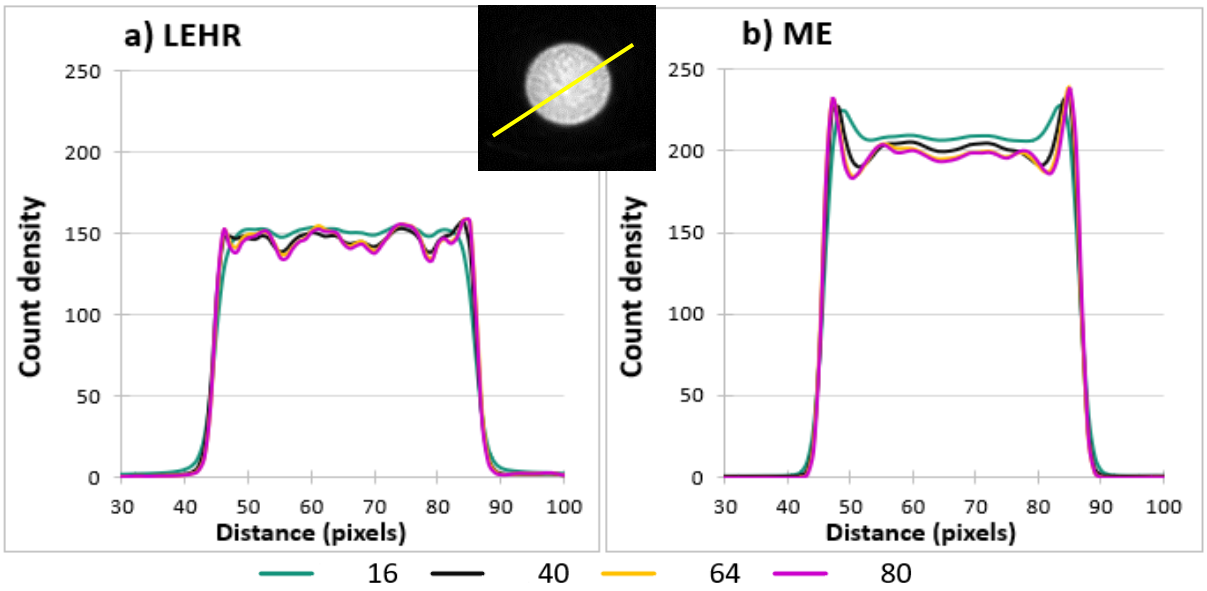

Figure 3-5: *LSFs drawn through the uniform section of the reconstructed IQ phantom SPECT images simulated with the (a) LEHR and (b) ME collimators. LSFs are shown for different OSEM equivalent iterations (i.e., 16, 40, 64 and 80). Inserted image indicates the profile position.*

Table 3-1 summarises the $\%RMS$ values that were obtained from the reconstructed images through the uniform section of the phantom. The $\%RMS$ determined for the LEHR collimator data increased with an increase in the number of EI. For the ME collimator, the $\%RMS$ decreased as the number of EI increased. The Gibbs ringing artefact is also visible in the reconstructed images through the uniform section of the phantom for both the LEHR and ME collimator datasets, as shown in Table 3-1.

***Table 3-1**: Reconstructed slices through the uniform section of the Carlson phantom and the noise (%RMS) determined from a 75% ROI are shown for the datasets reconstructed with different number of equivalent iterations. Results and images are shown for the reconstructed LEHR and ME collimated SPECT data.*

	%RMS			
Equivalent Iterations	**LEHR Collimator**		**ME Collimator**	
16		4.7%	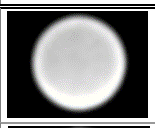	6.2%
40	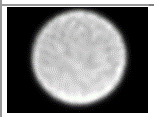	5.5%	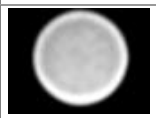	5.7%
64	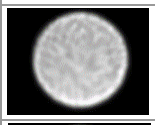	6.6%	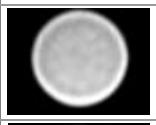	5.8%
80	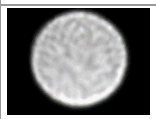	7.4%	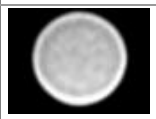	5.8%

ii Cold Lesion Contrast Insert

Figure 3-6 shows the line profiles through the largest rod of the cold lesion section in the phantom, while Table 3-2 reports the contrast values that were obtained for this

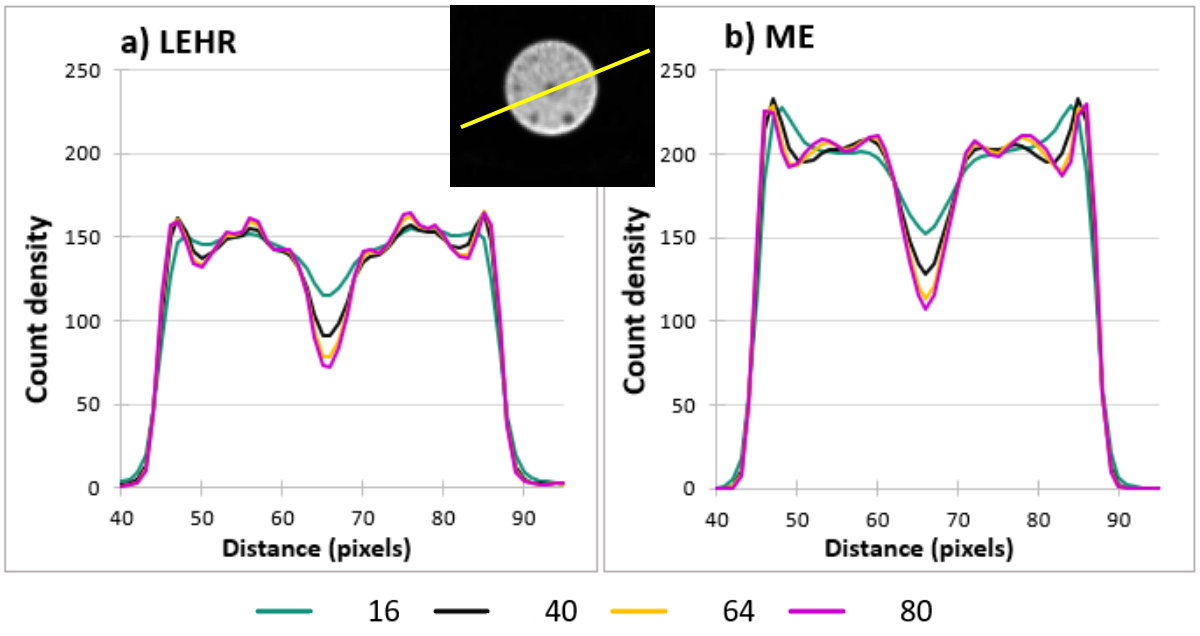

***Figure 3-6:** LSFs through the largest rod in the cold lesion insert of the reconstructed IQ phantom SPECT images simulated with the (a) LEHR and (b) ME collimators. LSFs are shown for different OSEM equivalent iterations (i.e., 16, 40, 64 and 80). Inserted image indicates the profile position.*

largest sphere (diameter 22.4 mm) for the different reconstructed datasets for both the LEHR and ME collimator.

A clear improvement in contrast with an increase in the number of EI was visible. When comparing the LEHR and ME datasets, a 6.7% and 2.3% improvement in contrast was seen when moving from 64 to 80 EI, respectively.

***Table 3-2**: Contrast (%) obtained for the largest sphere (22.4 mm diameter) of the IQ phantom for each of the datasets reconstructed with a different number of equivalent iterations. Results and images are shown for the reconstructed LEHR and ME collimated SPECT data.*

	Contrast (%)			
Equivalent Iterations	**LEHR Collimator**		**ME Collimator**	
16	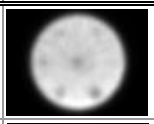	8.8%	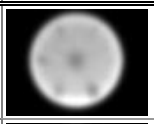	10.1%
40	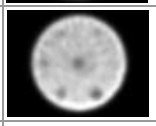	16.0%	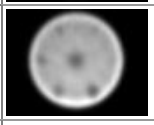	17.3%
64	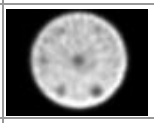	21.0%	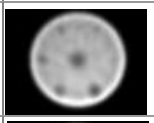	22.8%
80	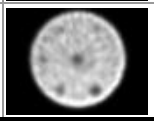	27.7%	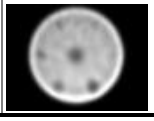	25.1%

iii Hot Lesion Resolution Insert

The images of the resolution insert reconstructed with different OSEM EI for the LEHR and ME collimators are shown in Figure 3-7.

For the LEHR dataset at 64 EI, the system is capable of distinguishing hole-pairs of up to 14.3 mm, whereas at 80 EI the system can distinguish 11.4 mm hole-pairs (indicated by yellow arrows in Figure 3-7). Thus, for the LEHR collimator, the spatial resolution improves as the EI increases. For the ME collimator, however, the spatial resolution does not improve beyond 64 EI where the 14.3 mm hole-pairs are distinguishable (indicated by green arrows). There is only an improvement in contrast when implementing 80 EI.

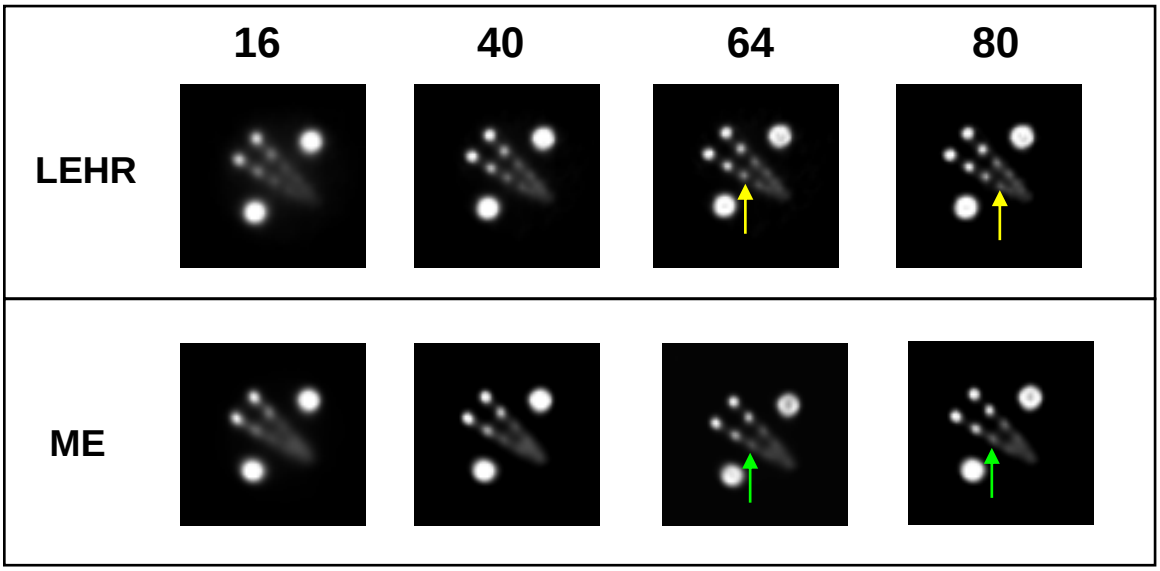

Figure 3-7: *Reconstructed images of the resolution insert section of the IQ phantom. SPECT images simulated with the LEHR and ME collimators reconstructed with different equivalent iterations (i.e., 16, 40, 64 and 80) are shown. The hole-pair diameters are: 38.5; 22.4; 17.9; 14.3; 11.4; 9.2; 7.3 and 5.9 mm.*

The LSFs obtained for the hot lesion insert of the phantom are shown in Figure 3-8 for both the LEHR and ME collimator. Figure 3-8(a) and (b) show the profiles through the hot lesions that are aligned in a V-shape in the phantom. For both datasets there is an improvement in the resolution as more EI are implemented during reconstruction. The graphs in Figure 3-8 confirm the visual results in Figure 3-7. However, for both collimators' A-S-CDR datasets, the peak over the 11.4mm hole can be identified.

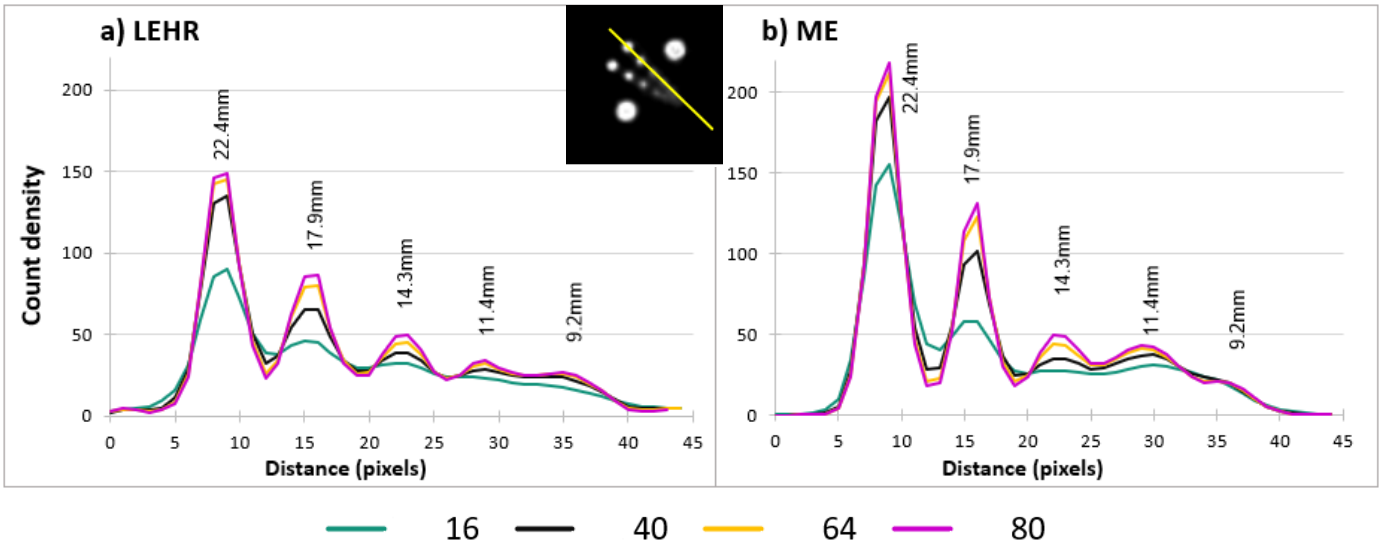

Figure 3-8: *LSFs across the hot lesion resolution section of the reconstructed IQ phantom SPECT images simulated with the LEHR (a) and ME (b) collimators. LSFs are shown for different OSEM equivalent iterations (i.e., 16, 40, 64 and 80). Inserted image indicates the profile position.*

iv Linear Insert

The summed slices of the linear insert were visually evaluated and compared for the different number of EI reconstructions. Figure 3-9 shows a visual improvement in the image contrast with an increase in iterations, however, the linearity was not affected.

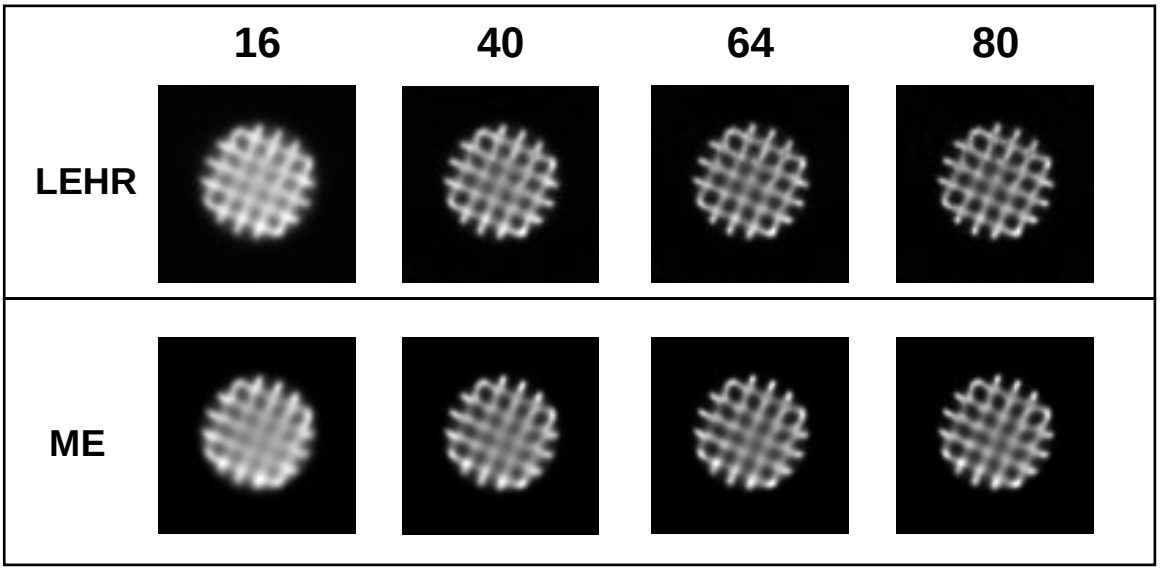

Figure 3-9: *Reconstructed images of the linearity insert section of the IQ phantom. SPECT images simulated with the LEHR and ME collimators reconstructed with different equivalent iterations (i.e., 16, 40, 64 and 80) are shown.*

When looking at the IQ parameters of uniformity, contrast, resolution, and linearity, there are improvements as the number of EI increases during reconstruction. However, the improvement becomes less prominent with a higher number of EI.

The $\%RMS$ values calculated in the uniform section of the phantom obtained with the LEHR collimator increased with increase in the number of EI, while the values stay relatively constant for the ME collimator. There are substantial improvements in the quantitative contrast when comparing the 40 and 64 EI datasets, for both collimators. The contrast for the LEHR dataset improves from 16.0% to 21.0% (5% absolute improvement) while the ME contrast improves with 5.5% (17.3% to 22.8%). The contrast improvement observed from 64 to 80 EI is 6.7% and 2.4% for the LEHR and ME collimator, respectively. The resolution LSFs show there are only slight differences between the 64 EI and 80 EI data. For both collimator datasets the contrast of the linearity insert images visually improved when a higher number of EI were implemented.

Considering the *%Recovery* of the spheres, the $\%RMS$, and the IQ parameters, the number of EI selected for further reconstruction of I-123 SPECT images acquired with either a LEHR or ME collimator is 64; eight subsets and eight iterations.

Any SPECT projection reconstructions performed during the remainder of the study were done using 64 EI.

3.3.2 Influence of SPECT Corrections on Image Quality

The *IQ phantom* projection images were reconstructed with 64 EI and with the different combinations of corrections (A; A-S; A-S-Geo; A-S-CDR). The data was analysed in terms of $\%RMS$, contrast, resolution and linearity and the results are presented below.

3.3.2.1 Uniformity Section

The LSFs obtained across the reconstructed images of the uniform section in the phantom reconstructed with different corrections applied for both collimators, are given in Figure 3-10.

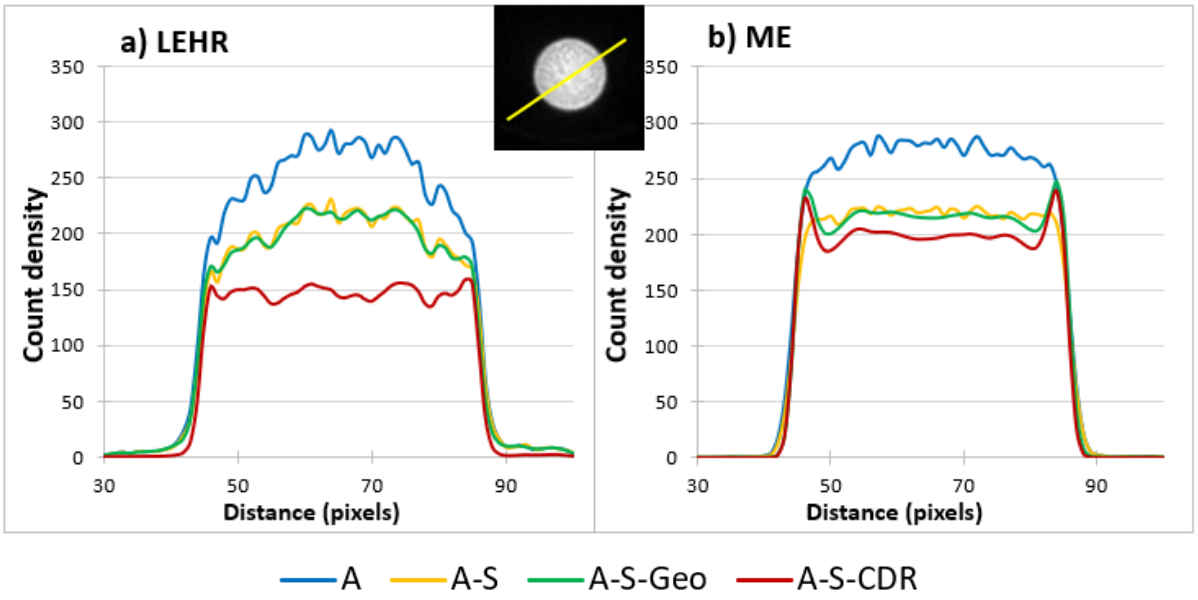

***Figure 3-10**: LSFs through the uniform section of the reconstructed IQ phantom. SPECT images simulated with the (a) LEHR and (b) ME collimators reconstructed with the different correction combinations applied. (Attenuation correction only (A), attenuation and ESSE scatter correction (A-S), attenuation, scatter and collimator-detector response correction considering the geometric effect (A-S-Geo) and attenuation, scatter and full collimator-detector response correction (A-S-CDR)). Inserted image indicates the profile position.*

The A-S-CDR LEHR graph in Figure 3-10a shows a relatively flat profile when compared to the profiles through the A; A-S and A-S-Geo data sets. This can be

attributed to the removal of the septal penetration contribution in the LEHR images when incorporating the full CDR correction. This is also reflected in the improvement in the $\%RMS$ value reported in Table 3-3. The difference between A-S-Geo and A-S-CDR for the ME data is mainly an intensity difference. Application of the geometric detector response correction during reconstruction resulted in a prominent ringing near the phantom edge especially for the ME data, creating peaks in the profile (Figure 3-10b). The LEHR A-S-CDR profile also indicates this Gibbs ringing artefact.

The $\%RMS$, calculated using equation *(3-2),* for the LEHR and ME image sets reconstructed with different corrections, is reported in Table 3-3.

Table 3-3: *Reconstructed slices through the uniform section of the IQ phantom and the noise (%RMS) determined from a 75% ROI are shown for the datasets reconstructed with the different correction combinations. (Attenuation correction only (A), attenuation and ESSE scatter correction (A-S), attenuation, scatter and collimator-detector response correction considering the geometric effect (A-S-Geo) and attenuation, scatter and full collimator-detector response correction (A-S-CDR)). Results and images are shown for the reconstructed LEHR and ME collimated SPECT data.*

	%RMS			
Corrections Applied	**LEHR Collimator**		**ME Collimator**	
A	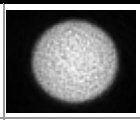	9.8%		6.9%
A-S	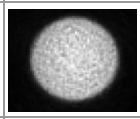	9.8%	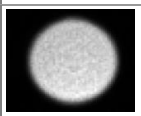	6.3%
A-S-Geo		7.1%		5.7%
A-S-CDR		6.6%	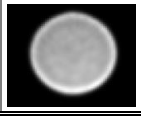	5.8%

The LEHR images reconstructed with all of the corrections (A-S-CDR) had the lowest percentage noise and had the most uniform profile. For the ME collimator, the $\%RMS$ slightly decreases when incorporating the scatter correction (A-S) in comparison to when only attenuation correction was applied (A). A further decline in

$\%RMS$ is seen when incorporating the geometric detector response correction, but it remains relatively stable when all corrections are applied (A-S-CDR).

3.3.2.2 Cold Lesion Contrast Insert

Figure 3-11 displays the LSFs through the largest cold sphere (22.4 mm diameter) in the LEHR and ME reconstructed images. The contrast values, determined for this sphere from the LEHR and ME corrected images, are tabulated in Table 3-4.

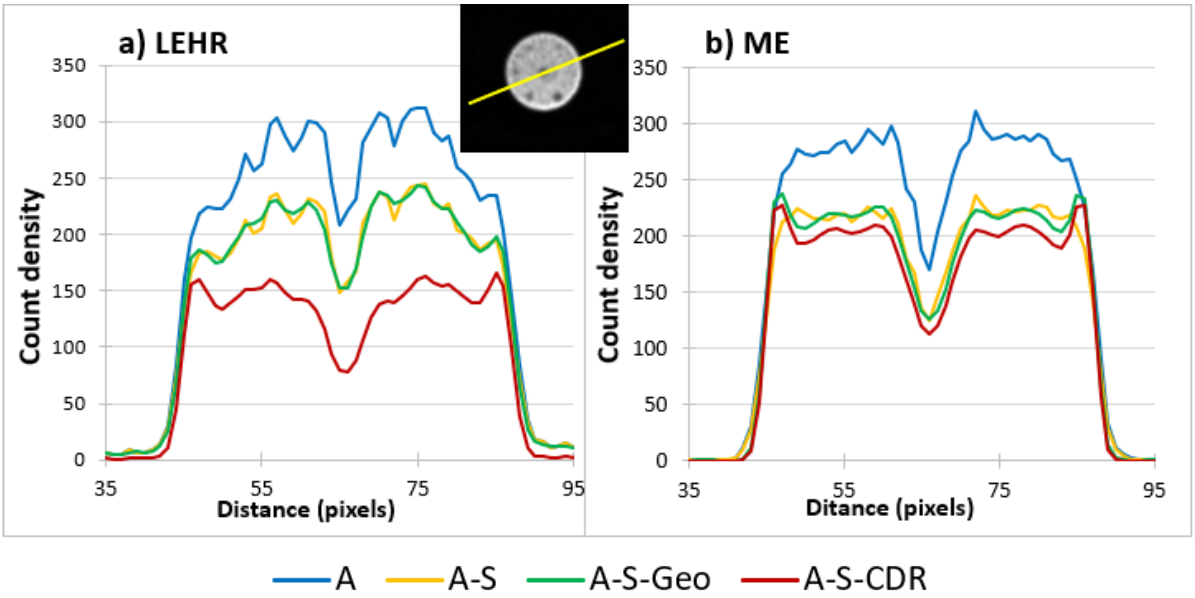

Figure 3-11: *LSFs through the largest rod in the cold lesion insert of the reconstructed IQ phantom. SPECT images simulated with the (a) LEHR and (b) ME collimators reconstructed with the different correction combinations applied (Attenuation correction only (A), attenuation and ESSE scatter correction (A-S), attenuation, scatter and collimator-detector response correction considering the geometric effect (A-S-Geo) and attenuation, scatter and full collimator-detector response correction (A-S-CDR)). Inserted image indicates the profile position.*

The values in Table 3-4 indicate that the contrast improves as the different corrections are applied during reconstruction. The contrast difference between the A-S-Geo and A-S-CDR for the LEHR data is 11.7%, while the contrast difference between the same correction combination images for the ME data is 0.2%. The LEHR images clearly benefit from septal penetration and scatter compensation as part of the CDR correction, whereas the contrast difference between the A-S-Geo and A-S-CDR datasets for the ME collimator was small.

Table 3-4: *Contrast (%) values obtained from the largest cold sphere (22.4mm diameter) of the IQ phantom for each of the datasets reconstructed with the different correction combinations (Attenuation correction only (A), attenuation and ESSE scatter correction (A-S), attenuation, scatter and collimator-detector response correction considering the geometric effect (A-S-Geo) and attenuation, scatter and full collimator-detector response correction (A-S-CDR)). Results and images are shown for the reconstructed LEHR and ME collimated SPECT data.*

	Contrast (%)			
Corrections Applied	**LEHR Collimator**		**ME Collimator**	
A	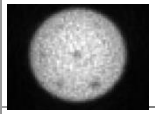	6.0%	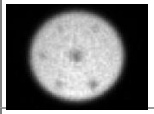	17.8%
A-S	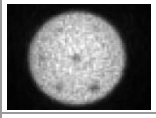	8.3%	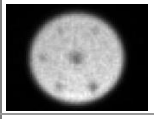	19.2%
A-S-Geo	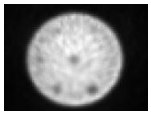	9.3%	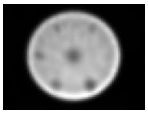	23.0%
A-S-CDR	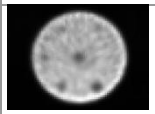	21.0%	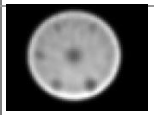	22.8%

3.3.2.3 Hot Lesion Resolution Insert

Reconstructed slices of the resolution insert for the LEHR and ME collimators, with different corrections applied, are given in Figure 3-13 and graphs of the four resolution LSFs obtained from each of the LEHR and ME datasets can be seen in Figure 3-12.

The hole pairs in the LEHR and ME reconstructed images become more distinct as each correction is applied, as shown in Figure 3-13. Figure 3-13 also shows that, based on the diameter of the smallest hole-pair visible, when the geometric correction (A-S-Geo) is applied, the spatial resolution is 14.3 mm and 17.9 mm for the LEHR and ME datasets, respectively (indicated by the yellow arrows). The 11.4 mm diameter hole-pair can be discerned for the A-S-CDR LEHR data, while the 14.3 mm diameter hole is visible on the ME A-S-CDR image (indicated by the green arrows). The graphs in Figure 3-12 confirm the visual perception of the resolution. However, for the A-S-Geo and A-S-CDR datasets, it is possible to distinguish the peak over the 11.4 mm hole-pair, for both collimators.

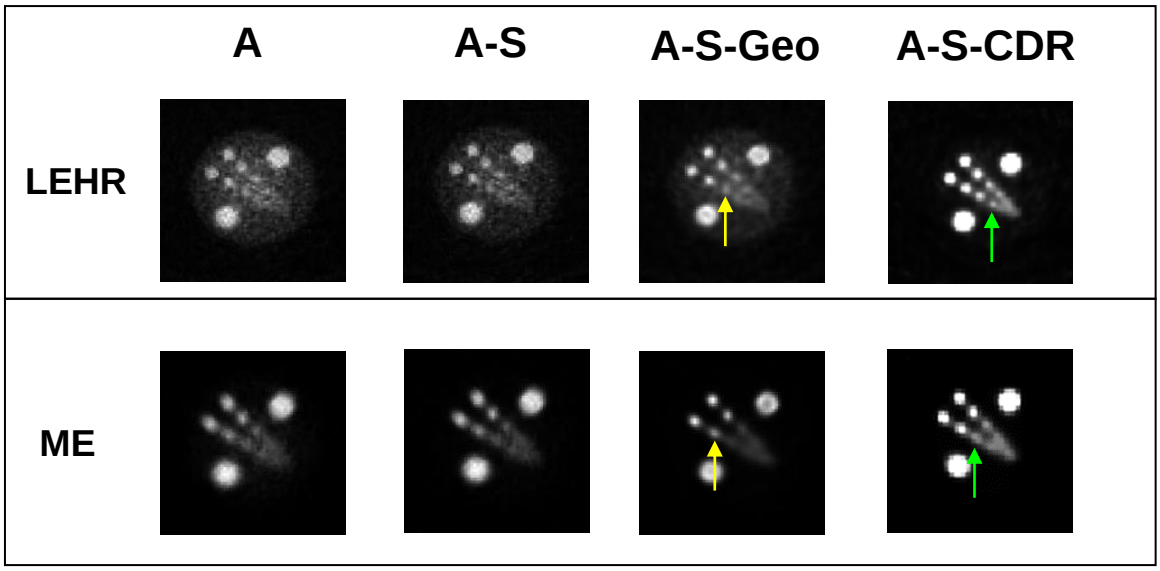

Figure 3-13: *Reconstructed images of the resolution insert section of the IQ phantom. SPECT images simulated with the LEHR and ME collimators reconstructed with different correction combinations applied (Attenuation correction only (A), attenuation and ESSE scatter correction (A-S), attenuation, scatter and collimator-detector response correction considering the geometric effect (A-S-Geo) and attenuation, scatter and full collimator-detector response correction (A-S-CDR)) are shown. The hole-pair diameters are: 38.5; 22.4; 17.9; 14.3; 11.4; 9.2; 7.3 and 5.9 mm*

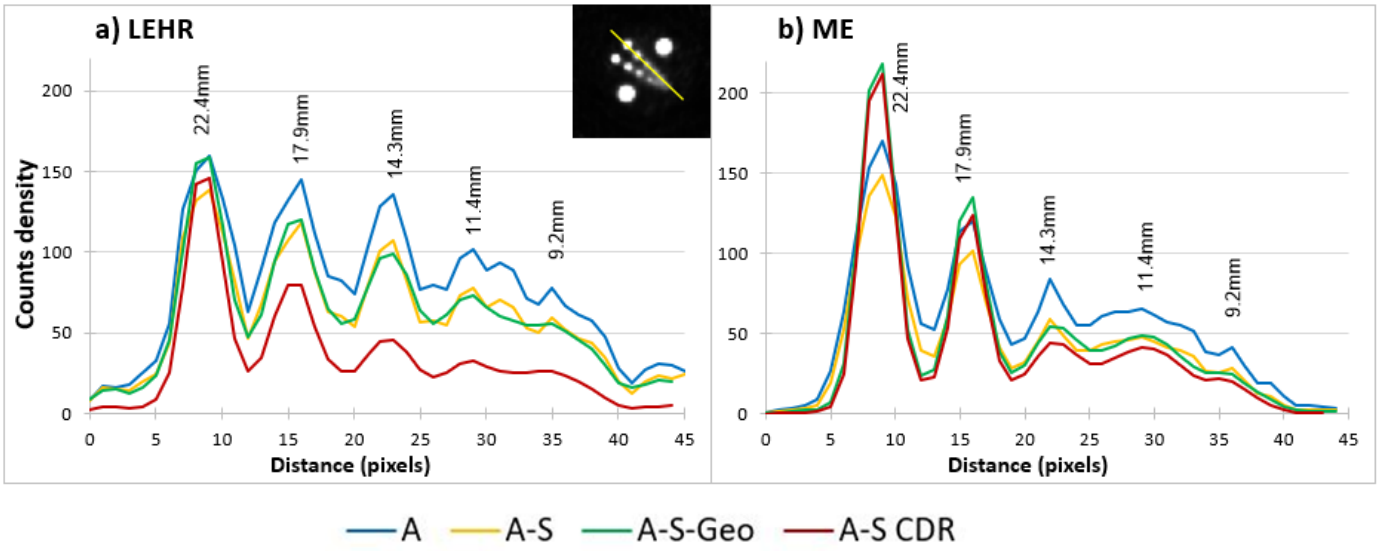

Figure 3-12: *LSFs across the hot lesion resolution section of the reconstructed IQ phantom SPECT images simulated with the (a) LEHR and (b) ME collimator with the different correction combinations applied. (Attenuation correction only (A), attenuation and ESSE scatter correction (A-S), attenuation, scatter and collimator-detector response correction considering the geometric effect (A-S-Geo) and attenuation, scatter and full collimator-detector response correction (A-S-CDR)). Inserted image indicates the profile position.*

3.3.2.4 Linearity Insert

Figure 3-14 shows the summed slices of the reconstructed linear insert for the LEHR and ME collimators with different SPECT correction combinations applied. The reconstructed images were visually evaluated and compared for the different correction combinations, for both collimators.

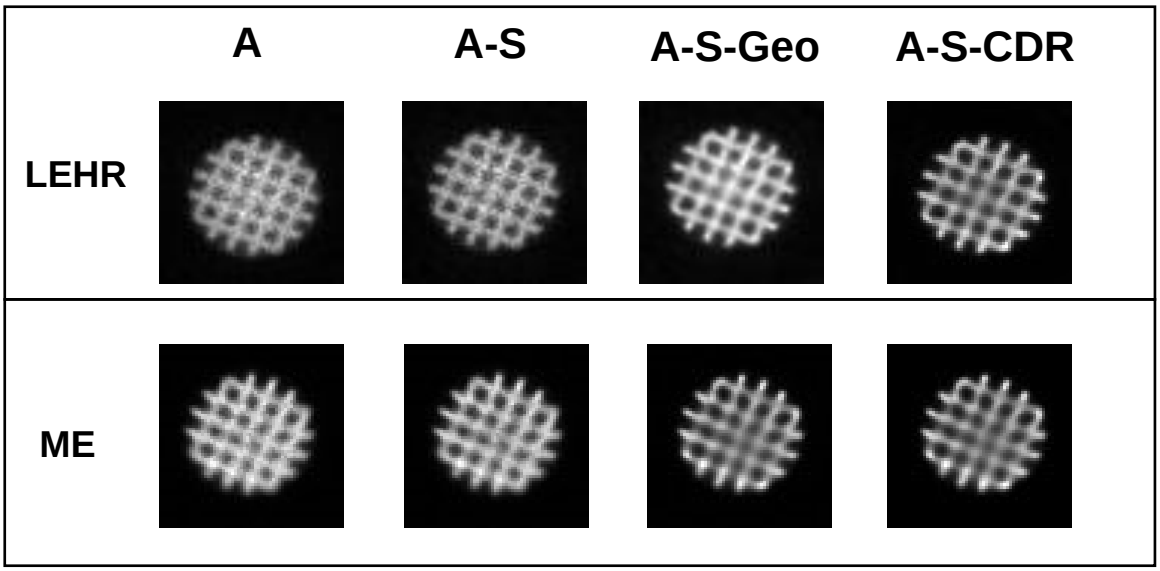

Figure 3-14: *Reconstructed images of the linearity insert section of the IQ phantom. SPECT images simulated with the LEHR and ME collimators reconstructed with different correction combinations applied (Attenuation correction only (A), attenuation and ESSE scatter correction (A-S), attenuation, scatter and collimator-detector response correction considering the geometric effect (A-S-Geo) and attenuation, scatter and full collimator-detector response correction (A-S-CDR)) are shown.*

It can be seen in Figure 3-14, that the contrast in the reconstructed linearity images improves with every correction added. The A-S-CDR image, for the LEHR dataset, has better contrast in comparison to the image reconstructed with just the geometric response. There is no notable difference for the ME dataset between the contrast of the A-S-Geo and A-S-CDR images. The blurring seen in the A-S-Geo and A-S-CDR images is typical for images reconstructed with CDR correction (geometric and/or septal penetration) (Frey and Tsui, 2006).

Figure 3-15 shows the normalised LSFs obtained from the LEHR and ME A-S-CDR corrected images of the uniform section, contrast insert and resolution insert. It is evident from the figure that when the CDR correction, which includes geometric response, septal penetration and septal scatter, is applied, the image quality is improved to such a degree that images from the two collimators are comparable.

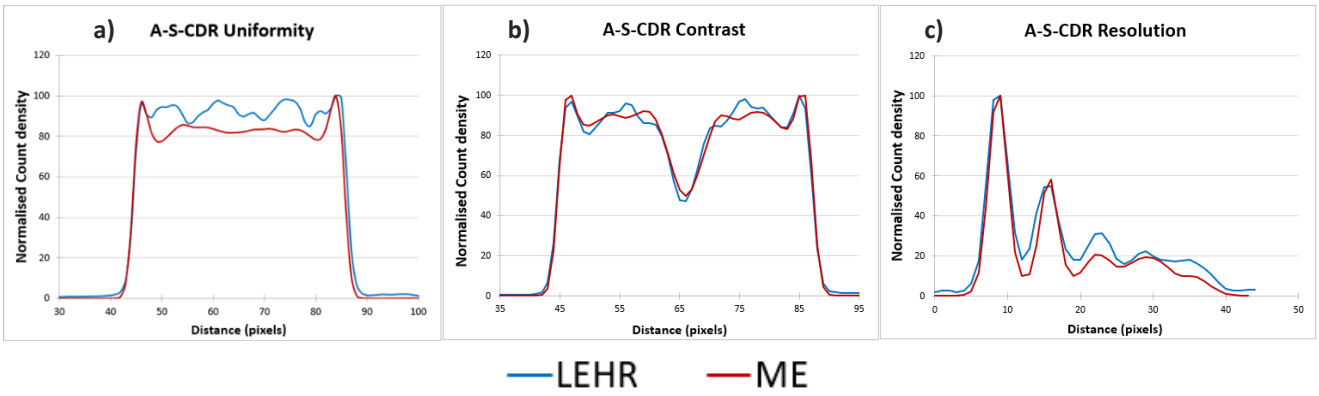

Figure 3-15: *Normalised LSFs through the (a) uniform section, (b) contrast insert and (c) resolution insert obtained from LEHR and ME images reconstructed with A-S-CDR*

3.4 Discussion

This study aimed to optimise and compare the OSEM reconstruction of I-123 SPECT studies acquired with LEHR and ME collimators. The number of EI were optimised for I-123 based on count density recovery and the image quality parameters of $\%RMS$, contrast (%) and resolution. The influence of SPECT reconstruction corrections on I-123 image quality was evaluated by comparing reconstructed images of an *IQ phantom* simulated with both the LEHR and ME collimators. The results thereof played a deciding role in finalising the optimised reconstruction parameters.

3.4.1 Recovery of Spherical Source Count Density

From the results in section Figure 3-3, it is clear that the number of EI will affect the accuracy of quantification. Literature states that a large number of iterations is required to improve the quantification accuracy in small objects, which is reflected in our results (He *et al.*, 2005; Pereira *et al.*, 2010; Dewaraja *et al.*, 2012). It has also been reported that for larger objects (> 60 ml), *%Recovery* is likely to be greater than 90% after 30 equivalent iterations (Dewaraja *et al.*, 2012). In our study, the *%Recovery* of the 45 mm and 60 mm spheres were already greater than 90% at 16 EI for both collimator types.

It is well known that increasing the number of iterations will increase the noise in the images (Brambilla *et al.*, 2005; Seret, 2006; Dewaraja *et al.*, 2012). If a ringing artefact is present, it will gain prominence as the EI increases, further affecting the noise level

(Dewaraja *et al.*, 2012). In our study, $\%RMS$ was used as a parameter to evaluate the noise, however it is not a true representation of noise, but rather an estimation of reconstruction noise and thus the results may deviate from what is stated in literature. From Figure 3-3, the $\%RMS$ slightly decreases as the EI increases, except for the 15 mm sphere where the $\%RMS$ increases with the number of EI.

It should be noted that the CDR correction aims to recover the sharp boundaries in the SPECT images. This may introduce Gibbs ringing artefacts, which creates a "hole" in the sphere and a bright ring at the sphere edges (see Figure 3-4) and is generated when the CDR correction attempts to recover fine details that have been lost because the system has a limited spatial resolution (Kangasmaa, Sohlberg and Kuikka, 2011; Kangasmaa, 2014; Ljungberg *et al.*, 2016; Marquis *et al.*, 2021). From the *cylindrical- and IQ phantom images* (Figure 3-4 and figures in Table 3-3), it can be seen that the Gibbs ringing artefact appears to be more prominent for the ME collimator. This is attributed to the ME collimator's poorer spatial resolution and higher image contrast when compared to the LEHR collimator (Liu and Farncombe, 2007; Zeng, 2011). This phenomenon is more pronounced when no filtering is applied to the data, which is generally the situation when the reconstruction aim is to obtain quantitative accurate results (Tran-Gia and Lassmann, 2018), as is the primary goal in this study. Due to the sphere-background ratio in these studies, a sharp edge is formed between the spheres and background, which enhance the presence of the Gibbs artefact. In typical scenarios, there is likely to be a higher background contribution, which will then result in fewer ringing artefacts.

The results in Figure 3-3 indicate that the optimisation of EI is dependent on object size and collimator type. Considering the change in *%Recovery* and $\%RMS$ of the spheres, the optimal EI chosen in this study for count recovery of I-123 SPECT studies performed with the LEHR and ME collimators is 64. This is similar to what has been found in literature (Niñerola-Baizán *et al.*, 2018; Morphis *et al.*, 2021).

3.4.2 Image Quality

The increase in noise with an increase in EI is also observed for the uniformity insert of the *IQ phantom*, although only for the LEHR collimator. There was little effect on the noise for the ME collimator dataset as the EI increased. From the images reconstructed with different correction combinations (Table 3-3), the $\%RMS$ is in

general lower for the ME data. The $\%RMS$ is comparable between the LEHR and ME data when full CDR corrections are applied (Figure 3-15).

The contrast obtained for the LEHR and ME collimators compared well when considering the different number of EI and all the corrections were applied. Without the full CDR correction, it is however clear that the ME collimator resulted in superior contrast. The better contrast is owed to the ME collimator's ability to reduce septal penetration (Inoue *et al.*, 2003; Rault *et al.*, 2007). From Table 3-2, it can be seen that for both collimators, the contrast improves as more EI are applied. Even though the maximum EI used in this study was 80, it has been shown in a Tc-99m study that improvement in cold contrast does not reach a plateau, even after 100 EI (Brambilla *et al.*, 2005). The LEHR contrast improves with every added correction applied during reconstruction. From Figure 3-15 it can be seen that when all corrections (A-S-CDR) are applied, the contrast obtained with the LEHR and ME collimators are comparable. When including corrections for septal penetration and scatter (A-S-CDR), there is no gain in contrast for the ME dataset. The contrast improvement when applying the CDR correction is confirmed with the LEHR images obtained of the linearity insert.

It is well known that the LEHR collimator produces images with a higher spatial resolution compared to the ME collimator. The qualitative results in Figure 3-7 corroborate the expected result (Macey *et al.*, 1986; Inoue *et al.*, 2004; Rault *et al.*, 2007). Studies done by El Fakhri *et al.* (1999, 2000) indicated that a CDR correction has to be applied when optimal spatial resolution is required. The findings of this study indicate that while applying A-S-CDR corrections improve the resolution of LEHR images, it has no effect on ME images. Qualitatively, the LEHR dataset reconstructed with A-S-CDR (Figure 3-13) resulted in better spatial resolution when compared to the A-S-CDR ME dataset (Figure 3-15).

3.5 Conclusion

This study's results show that the OSEM reconstruction of LEHR and ME I-123 SPECT studies with regards to count density recovery and image quality is optimal at 64 EI. The reconstruction is further improved by applying attenuation, scatter and CDR corrections. Including modelling of collimator septal scatter and penetration improved the image quality of the LEHR dataset remarkable.

When all of the mentioned reconstruction corrections are applied, the image quality of LEHR and ME images (reconstructed with 64 EI), with regards to $\%RMS$, contrast and resolution, is comparable. This leads to the belief that accurate I-123 quantification SPECT studies can be acquired with either LEHR or ME collimators. This theory will be evaluated in future work (**Chapter 4**).

3.6 References

Ahn, B. C. (2016) 'Personalized Medicine Based on Theranostic Radioiodine Molecular Imaging for Differentiated Thyroid Cancer', *BioMed Research International*, 2016, pp. 1–9. doi: 10.1155/2016/1680464.

Asl, M. N., Sadremomtaz, A. and Bitarafan-Rajabi, A. (2013) 'Evaluation of six scatter correction methods based on spectral analysis in 99mTc SPECT imaging using SIMIND Monte Carlo simulation', *Journal of Medical Physics*, 38(4), pp. 189–198. doi: 10.4103/0971-6203.121197.

Bombardieri, E., Giammarile, F., Aktolun, C., Baum, R. P., Bischof Delaloye, A., Maffioli, L., Moncayo, R., Mortelmans, L., Pepe, G., Reske, S. N., Castellani, M. R. and Chiti, A. (2010) '131I/123I-Metaiodobenzylguanidine (mIBG) scintigraphy: Procedure guidelines for tumour imaging', *European Journal of Nuclear Medicine and Molecular Imaging*, 37(12), pp. 2436–2446. doi: 10.1007/s00259-010-1545-7.

Brambilla, M., Cannillo, B., Dominietto, M., Leva, L., Secco, C. and Inglese, E. (2005) 'Characterization of ordered-subsets expectation maximization with 3D post-reconstruction Gauss filtering and comparison with filtered backprojection in 99mTc SPECT', *Annals of Nuclear Medicine*, 19(2), pp. 75–82. doi: 10.1007/BF03027384.

Brown, C. M. (2018) *Application of Novel Corrections for Quantification of 123 I SPECT*, *Thesis, PhD*. University of Glasgow. Available at: https://theses.gla.ac.uk/8923/.

Bruyant, P. P. (2002) 'Analytic and Iterative Reconstruction Algorithms in SPECT', *Journal of Nuclear Medicine*, 43(10), pp. 1343–1358.

Chen, J., Garcia, E. V., Galt, J. R., Folks, R. D. and Carrio, I. (2006) 'Optimized acquisition and processing protocols for I-123 cardiac SPECT imaging', *Journal of Nuclear Cardiology*, 13(2), pp. 251–260. doi: 10.1016/j.nuclcard.2006.01.017.

Dewaraja, Y. K., Frey, E. C., Sgouros, G., Brill, A. B., Roberson, P., Zanzonico, P. B. and Ljungberg, M. (2012) 'MIRD Pamphlet no. 23: Quantitative SPECT for Patient-Specific 3-Dimensional Dosimetry in Internal Radionuclide Therapy', *Journal of Nuclear Medicine*, 53(8), pp. 1310–1325. doi: 10.2967/jnumed.111.100123.

Dewaraja, Y. K., Ljungberg, M., Majumdar, A., Bose, A. and Koral, K. F. (2002) 'A parallel Monte Carlo code for planar and SPECT imaging: Implementation, verification and applications in I-131 SPECT', *Computer Methods and Programs in Biomedicine*,

67(2), pp. 115–124. doi: 10.1016/S0169-2607(01)00121-3.

Dobbeleir, A. A., Hambÿe, A. S. E. and Franken, P. R. (1999) 'Influence of high-energy photons on the spectrum of iodine-123 with low- and medium-energy collimators: Consequences for imaging with 123I-labelled compounds in clinical practice', *European Journal of Nuclear Medicine*, 26(6), pp. 655–658. doi: 10.1007/s002590050434.

El Fakhri, G., Buvat, I., Benali, H., Todd-Pokropek, A. and Di Paola, R. (2000) 'Relative Impact of Scatter, Attenuation, Collimator Response and Finite Spatial Resolution Corrections in Cardiac SPECT', *Journal of Nuclear Medicine* 41(8), pp. 1400-1408. Available at: https://jnm.snmjournals.org/content/41/8/1400.long.

El Fakhri, G. N., Buvat, I., Pélégrini, M., Benali, H., Almeida, P., Bendriem, B., Todd-Pokropek, A. and Di Paola, R. (1999) 'Respective roles of scatter, attenuation, depth-dependent collimator response and finite spatial resolution in cardiac single-photon emission tomography quantitation: A Monte Carlo study', *European Journal of Nuclear Medicine*, 26(5), pp. 437–446. doi: 10.1007/s002590050409.

Fleming, J. S., Goatman, K. A., Julyan, P. J., Boivin, C. M., Wilson, M. J., Barber, R. W., Bird, N. J. and Fryer, T. D. (2000) 'A comparison of performance of three gamma camera systems for positron emission tomography', *Nuclear Medicine Communications*, 21(12), pp. 1095–1102. doi: 10.1097/00006231-200012000-00002.

Fluke Biomedical (2005) 'Nuclear Associates 76-823, 76-824 & 76-825 PET/SPECT Phantom Source Tank,Phantom Inserts and Cardiac Insert', *Manual*, p. 10. Available at: https://www.manualsdir.com/manuals/767906/fluke-biomedical-76-823.html.

Frangos, S. and Buscombe, J. R. (2019) 'Why should we be concerned about a "g"?', *European Journal of Nuclear Medicine and Molecular Imaging*, 46(519), p. 1. doi: 10.3345/cep.2020.00521.

Frey, E. C., Humm, J. L. and Ljungberg, M. (2012) 'Accuracy and precision of radioactivity quantification in nuclear medicine images', *Seminars in Nuclear Medicine*. Elsevier Inc., 42(3), pp. 208–218. doi: 10.1053/j.semnuclmed.2011.11.003.

Frey, E. C. and Tsui, B. M. W. (1996) 'A New Method for Modeling the Spatially-Variant, Object-Dependent Scatter Response Function in SPECT', *IEEE Nuclear Science Symposium Conference Record*, pp. 1082–1086.

Frey, E. C. and Tsui, B. M. W. (2006) 'Collimator-Detector Response Compensation in SPECT', in Zaidi, H. *Quantitative Analysis in Nuclear Medicine Imaging.* Springer. pp 141-166. doi:10.1007/0-387-25444-7_5

De Geeter, F., Franken, P. R., Defrise, M., Andries, H., Saelens, E. and Bossuyt, A. (1996) 'Optimal collimator choice for sequential iodine-123 and technetium-99m imaging', *European Journal of Nuclear Medicine*, 23(7), pp. 768–774. doi: 10.1007/BF00843705.

Gilland, D. R., Jaszczak, R. J., Turkington, T. G., Greer, K. L. and Coleman, R. E. (1994) 'Volume and Activity Quantitation with I-123 SPECT', *Journal of Nuclear Medicine*, 35(10), pp. 1707–1713. Available at: https://jnm.snmjournals.org/content/jnumed/35/10/1707.full.pdf.

Hawman, E., Vija, A. H., Daffach, R. and Ray, M. (2014) 'Flash 3D TM Technology Optimizing SPECT Quality and Accuracy', (December), p. date accessed: 23/02/2016. Available at: http://www.siemensmedical.com/nuclear.

He, B., Du, Y., Song, X., Segars, W. P. and Frey, E. C. (2005) 'A Monte Carlo and Physical Phantom Evaluation of Quantitative In-111 SPECT', *Physics in Medicine and Biology*, 50(17), pp. 4169–4185. doi: 10.1088/0031-9155/50/17/018.

Hesse, B., Tägil, K., Cuocolo, A., Anagnostopoulos, C., Bardiés, M., Bax, J., Bengel, F., Sokole, E. B., Davies, G., Dondi, M., Edenbrandt, L., Franken, P., Kjaer, A., Knuuti, J., Lassmann, M., Ljungberg, M., Marcassa, C., Marie, P. Y., McKiddie, F., O'Connor, M., Prvulovich, E., Underwood, R. and Van Eck-Smit, B. (2005) 'EANM/ESC procedural guidelines for myocardial perfusion imaging in nuclear cardiology', *European Journal of Nuclear Medicine and Molecular Imaging*, 32(7), pp. 855–897. doi: 10.1007/s00259-005-1779-y.

Holen, R. Van, Vandenberghe, S. and Staelens, S. (2008) 'Comparing planar image quality of rotating slat and parallel hole collimation : influence of system modeling', *Physics in Medicine and Biology*, 53, pp. 1989–2002. doi: 10.1088/0031-9155/53/7/013.

Hudson, H. M. and Larkin, R. S. (1994) 'Accelerated Image Reconstruction Using Ordered Subsets of Projection Data', *IEEE transactions on medical imaging*, 13(4), pp. 601–609. Available at: https://ieeexplore.ieee.org/stamp/stamp.jsp?arnumber=363108&casa_token=T7Z-tI9VOLgAAAAA:y9ErK3Qs71X7dUsn8p4bkR1NOKQwLPgTmfeA27UxiYTfVq7midHvXeaqnH4d5kwOT66GrlO7G1a5&tag=1.

Hutton, B. E., Hudson, H. M. and Beekman, F. J. (1997) 'Occasional survey A clinical perspective of accelerated statistical reconstruction', *European Journal of Nuclear Medicine*, 24(7), pp. 797–808.

IAEA (2009) *Quality Assurance for SPECT Systems*, *IAEA Human Health Series. No. 6*. Available at: http://www-pub.iaea.org/MTCD/publications/PDF/Pub1394_web.pdf.

Inoue, Y., Shirouzu, I., Machida, T., Yoshizawa, Y., Akita, F., Minami, M. and Ohtomo, K. (2004) 'Collimator choice in cardiac SPECT with I-123-labeled tracers', *Journal of Nuclear Cardiology*, 11(4), pp. 433–439. doi: 10.1016/j.nuclcard.2004.04.009.

Inoue, Y., Suzuki, A., Shirouzu, I., Machida, T., Yoshizawa, Y., Akita, F., Ohnishi, S., Yoshikawa, K. and Ohtomo, K. (2003) 'Effect of collimator choice on quantitative assessment of cardiac iodine 123 MIBG uptake', *Journal of Nuclear Cardiology*, 10(6), pp. 623–632. doi: 10.1016/S1071-3581(03)00652-4.

Kalantari, F., Rajabi, H. and Saghari, M. (2011) ‘Quantification and reduction of the collimator-detector response effect in SPECT by applying a system model during iterative image reconstruction : a simulation study’, *Nuclear Medicine Communications*, 33(3), pp. 228–238. doi: 10.1097/MNM.0b013e32834e755f.

Kangasmaa, T. (2014) *Evaluation and optimization of novel reconstruction methods for myocardial perfusion SPECT*. Edited by P. Pertti, P. Kilpeläinen, K. Peiponen, and M. Vornanen.*Academic Disserattion*, Finland: Eastern Finland University Library.

Kangasmaa, T., Sohlberg, A. and Kuikka, J. T. (2011) ‘Reduction of Collimator Correction Artefacts with Bayesian Reconstruction in Spect’, *International Journal of Molecular Imaging*, 2011, pp. 1–6. doi: 10.1155/2011/630813.

Laboratoire National Henri Becquerel (2004) *Table de Radionucléides - I-123*. Available at: http://www.lnhb.fr/nuclides/I-123_tables.pdf (Accessed: 5 November 2018).

Leong, L. K., Kruger, R. L. and O’Connor, M. K. (2001) ‘A Comparison of the Uniformity Requirements for SPECT Image Reconstruction Using FBP and OSEM Techniques’, *Journal of Nuclear Medicine Technology*, 29(2), pp. 79–83. Available at: https://tech.snmjournals.org/content/29/2/79.

Liu, S. and Farncombe, T. H. (2007) ‘Collimator-Detector Response Compensation in Quantitative SPECT Reconstruction’, *IEEE Nuclear Science Symposium Conference Record*, 5, pp. 3955–3960. doi: 10.1109/NSSMIC.2007.4436983.

Ljungberg, M., Celler, A., Konijnenberg, M. W., Eckerman, K. F., Dewaraja, Y. K. and Sjögreen-Gleisner, K. (2016) ‘MIRD Pamphlet no. 26: Joint EANM/MIRD Guidelines for Quantitative 177Lu SPECT Applied for Dosimetry of Radiopharmaceutical Therapy’, *Journal of Nuclear Medicine*, 57(1), pp. 151–162. doi: 10.2967/jnumed.115.159012.

Ljungberg, M. and Strand, S. E. (1990) ‘Scatter and Attenuation Correction in SPECT Using Density Maps and Monte Carlo Simulated Scatter Functions.’, *Journal of nuclear medicine*, 31(9), pp. 1560–1567.

Loening, A. M. and Gambhir, S. S. (2003) ‘AMIDE: A Free Software Tool for Multimodality Medical Image Analysis’, *Molecular Imaging*, 2(3), pp. 131–137. doi: 10.1162/153535003322556877.

Macey, D. J., Denardo, G. L., Denardo, S. J. and Hines, H. H. (1986) ‘Comparison of Low- and Medium-Energy Coffimators for SPECT Imaging with Iodine-123-Labeled Antibodies’, *Journal of Nuclear Medicine*, 27, pp. 1467–1475. Available at: https://jnm.snmjournals.org/content/jnumed/27/9/1467.full.pdf.

Marquis, H., Deidda, D., Gillman, A., Willowson, K. P., Gholami, Y., Hioki, T., Eslick, E., Thielemans, K. and Bailey, D. L. (2021) ‘Theranostic SPECT reconstruction for improved resolution: application to radionuclide therapy dosimetry’, *EJNMMI Physics*, 8(1), pp. 1–17. doi: 10.1186/s40658-021-00362-x.

Matsutomo, N., Nagaki, A., Yamao, F. and Sasaki, M. (2015) 'Optimization of iterative reconstruction parameters with 3-dimensional resolution recovery, scatter and attenuation correction in 123I-FP-CIT SPECT', *Annals of Nuclear Medicine*. Springer Japan, 29(7), pp. 636–642. doi: 10.1007/s12149-015-0987-1.

Matthay, K. K., Shulkin, B., Ladenstein, R., Michon, J., Giammarile, F., Lewington, V., Pearson, A. D. J. and Cohn, S. L. (2010) 'Criteria for evaluation of disease extent by 123 I-metaiodobenzylguanidine scans in neuroblastoma: A report for the International Neuroblastoma Risk Group (INRG) Task Force', *British Journal of Cancer*. Nature Publishing Group, 102(9), pp. 1319–1326. doi: 10.1038/sj.bjc.6605621.

Minarik, D., Sjögreen Gleisner, K. and Ljungberg, M. (2008) 'Evaluation of quantitative Y-90 SPECT based on experimental phantom studies', *Physics in Medicine and Biology*, 53(20), pp. 5689–5703. doi: 10.1088/0031-9155/53/20/008.

Morphis, M., van Staden, J., du Raan, H. and Ljungberg, M. (2021) 'Evaluation of Iodine-123 and Iodine-131 SPECT activity quantification: a Monte Carlo study', *EJNMMI Physics*. Springer International Publishing, 8(61), pp. 1–20. doi: 10.1186/s40658-021-00407-1.

Niñerola-Baizán, A., Gallego, J., Cot, A., Aguiar, P., Lomeña, F., Javier, P. and Domènec, R. (2018) 'Optimization of the reconstruction parameters in 123I-FP-CIT', *Physics in Medicine and Biology*, 63, pp. 1–10. doi: 10.1088/1361-6560/aab799.

Ogawa, K. (2004) 'Image distortion and correction in single photon emission CT', *Annals of Nuclear Medicine*, 18(3), pp. 171–185.

Pereira, J., Stabin, M., Lima, F., Guimaraes, M. and Forrester, J. (2010) 'Image Quantification for Radiation Dose Calculations - Limitations and Uncertainties', *Health Physics*, 99(5), pp. 688–701. doi: 10.1097/HP.0b013e3181e28cdb.

Raeside, D. E. (1976) 'Monte Carlo Principles and Applications', *Physics in Medicine and Biology*, 21(2), pp. 181–197. doi: 10.1088/0031-9155/21/2/001.

Ramonaheng, K., van Staden, J. A., du Raan, H. and du Raan, H. (2020) 'Validation of a Monte Carlo modelled gamma camera for Lutetium-177 imaging', *Applied Radiation and Isotopes*. Elsevier Ltd, 163, pp. 1–9. doi: 10.1016/j.apradiso.2020.109200.

Ramonaheng, K., van Staden, J. A., du Raan, H. and du Raan, H. (2021) 'The effect of calibration factors and recovery coefficients on 177Lu SPECT activity quantification accuracy: a Monte Carlo study', *EJNMMI Physics*., 8(1), p. 23. doi: 10.1186/s40658-021-00365-8.

Rault, E., Vandenberghe, S., Van Holen, R., De Beenhouwer, J., Staelens, S. and Lemahieu, I. (2007) 'Comparison of Image Quality of Different Iodine Isotopes (I-123, I-124, and I-131)', *Cancer Biotherapy and Radiopharmaceuticals*, 22(3), pp. 423–430. doi: 10.1089/cbr.2006.323.

Razavi, S. H., Kalantari, F., Bagheri, M., Namiranian, N., Nafisi-Moghadam, R., Mardanshahi, A., Emami-Ardekani, A., Sobhan Ardekani, M. and Razavi-Ratki, S. K. (2017) 'Characterization of low, medium and high energy collimators for common isotopes in nuclear medicine: A Monte Carlo study', *Iranian Journal of Nuclear Medicine*, 25(2), pp. 100–104.

Sadremomtaz, A. and Taherparvar, P. (2013) 'The influence of filters on the SPECT image of Carlson phantom', *Journal of Biomedical Science and Engineering*, 06(03), pp. 291–297. doi: 10.4236/jbise.2013.63037.

Seret, A. (2006) 'Letter to the editor - The number of subsets required for OSEM reconstruction in nuclear cardiology', *European Journal of Nuclear Medicine*, pp. 231–231. doi: 10.3368/er.22.2.82.

Sjögreen, K., Ljungberg, M. and Strand, S. E. (1996) 'Parameters Influencing Volume and Activity Quantitation in SPECT', *Acta Oncologica*, 35(3), pp. 323–330. doi: 10.3109/02841869609101649.

Sjögreen, K., Ljungberg, M., Wingårdh, K., Minarik, D. and Strand, S. (2005) 'The LundADose Method for Planar Image Activity Quantification and Absorbed-Dose Assessment in Radionuclide Therapy', *Cancer Biotherapy & Radiopharmaceuticals*, 20(1), pp. 92–97. Available at: https://books.google.co.za/books?id=YzzNBQAAQBAJ&dq=Monte+Carlo+calculations+in+nuclear+medicine&lr=.

Söderberg, M., Mattsson, S., Oddstig, J., Uusijärvi-Lizana, H., Valind, S., Thorsson, O., Garpered, S., Prautzsch, T., Tischenko, O. and Leide-Svegborn, S. (2012) 'Evaluation of image reconstruction methods for 123I-MIBG-SPECT: A rank-order study', *Acta Radiologica*, 53(7), pp. 778–784. doi: 10.1258/ar.2012.120078.

Todd-Pokropek, A. (1983) 'Non-circular orbits for the reduction of uniformity artefacts in SPECT', *Physics in Medicine and Biology*, 28(3), pp. 309–313. doi: 10.1088/0031-9155/28/3/013.

Tran-Gia, J. and Lassmann, M. (2018) 'Optimizing Image Quantification for 177Lu SPECT/CT Based on a 3D Printed 2-Compartment Kidney Phantom', *Journal of Nuclear Medicine*, 59(4), pp. 616–624. doi: 10.2967/jnumed.117.200170.

Wahl, R. L., Ahuja, S. and Clarke, B. (2021) 'Current Landscape of Radiopharmaceutical Therapies: SNMMI Therapy Task Force Survey', *Journal of Medical Physics*, 62(5), pp. 11–16.

Yordanova, A., Eppard, E., Kürpig, S., Bundschuh, R. A., Schönberger, S., Gonzalez-carmona, M. and Feldmann, G. (2017) 'Theranostics in nuclear medicine practice', *OncoTargets and Therapy*, (October), pp. 4821–4828.

Yushkevich, P. A., Piven, J., Hazlett, C., Smith, G., Ho, S., Gee, J. C. and Gerig, G. (2006) 'User-guided 3D active contour segmentation of anatomical structures : Significantly improved efficiency and reliability', *NeuroImage*, 31, pp. 1116–1128. doi:

10.1016/j.neuroimage.2006.01.015.

Zaidi, H. (1999) ‘Relevance of accurate Monte Carlo modeling in nuclear medical imaging Addendum to “Relevance of accurate Monte Carlo modeling in nuclear medical imaging Relevance of accurate Monte Carlo modeling in nuclear medical imaging”’, *Medical Physics*, 26(816), pp. 2566–574. doi: 10.1118/1.598945.

Zeng, G. L. (2011) ‘Gibbs Artifact Reduction by Nonnegativity Constraint’, *Journal of Nuclear Medicine Technology*, 39(3), pp. 213–219. doi: 10.2967/jnmt.110.086439.

Chapter 4: Paper 3

Quantification Accuracy of I-123 Patient Phantom SPECT Studies using LEHR and ME Collimators

Table of Contents

Abstract

The purpose of the study was to determine the quantification accuracy of I-123 SPECT studies in patient phantoms acquired with LEHR and ME collimators. SPECT studies of voxel-based patient phantoms containing 30 mm (14.2 ml) and 50 mm (65.5 ml) diameter spheres were simulated with the Monte Carlo code SIMIND. The simulated SPECT projections were reconstructed with the OSEM iterative algorithm which was optimised in **Chapter 3** for the number of equivalent iterations and corrections for image degrading factors. Calibration factors and recovery coefficients were determined for LEHR and ME collimators using voxel-based cylindrical phantoms fitted with spheres. Two scenarios of the voxel-based patient phantoms, with sphere-to-background ratios of 100:1 and 50:1, were simulated. The quantification accuracy was evaluated for the spheres. It was found that with appropriate image degrading corrections, including partial volume effect corrections, quantification errors not exceeding 3.8% were obtained in patient studies for the LEHR and ME collimators. The quantification errors for I-123 LEHR and I-123 ME studies were comparable, implying that LEHR collimators could be used for I-123 studies in institutions that do not have access to ME collimators if appropriate corrections are incorporated in the reconstruction algorithm.

4.1 Introduction

Metaiodobenzylguanidine (mIBG) labelled with Iodine-131 (I-131) is used to both diagnose and treat neuroblastomas. Although effective for therapy due to its maximum energy β-emissions (606.3 keV; 89.4%), I-131 is less effective as a diagnostic (imaging) radionuclide due to its high-energy gamma-ray contamination. I-131 has high-energy, high-abundance gamma emissions at 364.5 keV (81.2%), 637.0 keV (7.2%) and 722.9 keV (1.8%) (Laboratoire National Henri Becquerel, 2014). This necessitates the use of a high-energy collimator during single photon emission computed tomography (SPECT) imaging. The thicker septa of these collimators degrade the spatial resolution of the images making the image quality inferior. Iodine-123 (I-123) has far more desirable characteristics as a diagnostic radionuclide. I-123 decays through electron capture and have more suitable gamma emissions at 159.0 keV (at 83.3% abundance) for imaging. In addition, I-123 has a lower radiation burden than I-131 (Matthay *et al.*, 2010), as it does not emit any β-particles and has a

physical half-life (13.2 hours) more suitable compared to I-131 (8.0 days) (Laboratoire National Henri Becquerel, 2004). It is well established in literature that I-123 is more effective at detecting lesions than I-131 (Kushner *et al.*, 2009) due to the better image quality. Because of their similar biological and chemical properties, the radioisotopes I-123 and I-131 are ideal theragnostic partners and can be used interchangeably in radiopharmaceutical therapy (RPT). RPT is a new term established to refer to certain therapies including theragnostics (Wahl, Ahuja and Clarke, 2021), which is the molecular identification of a target by a diagnostic radiopharmaceutical and the treatment by an identical therapeutic radiopharmaceutical (Frangos and Buscombe, 2019).

Neuroblastomas originate from the sympathetic nervous system, and metastases have been found in cortical bone, bone marrow and the liver. This is one of the most prolific malignancies diagnosed in early childhood (Matthay, 1997; Kushner *et al.*, 2009). mIBG is analogous to norepinephrine and is taken up in central nervous system tissue (Vallabhajosula, 2009). mIBG labelled to I-123 and I-131, allows for detection and treatment of metastases in soft tissue and even in bone and bone marrow. It has been proven that the efficacy of a treatment plan increases if the same agent is used during imaging (diagnosis) and treatment (Parisi *et al.*, 2016; Marquis *et al.*, 2021).

In Nuclear Medicine (NM), the purpose of quantifying radioactivity concentration found in cancerous tissue is to support diagnostic and treatment decisions and to assess the disease response to therapy (Theerakulpisut *et al.*, 2018). With this being said, high accuracy of activity quantification is desirable. SPECT reconstruction parameters, calibration factors (CF), and partial volume effects (PVE) are all factors that can influence the quantification accuracy. SPECT reconstruction that adequately corrects for physically degrading factors such as attenuation, scatter and collimator-detector response (CDR) must be performed. Incorporating corrections for these image degrading factors in the iterative reconstruction algorithm is the first step in improving the quantification accuracy (Frey, Humm and Ljungberg, 2012).

Another step towards improving the accuracy of activity quantification in SPECT images is determining a CF that converts voxel count values into in-vivo radioactivity concentrations. It is determined by acquiring planar/ tomographic images of a phantom/source with known activity concentration. The CF is isotope specific and is

further influenced by the gamma camera and collimator design specifications. It has been reported that a CF can be determined using different source geometries, such as a point-source in air, a sphere in air/water or water-filled cylindrical phantoms (Zhao *et al.*, 2018; Morphis *et al.*, 2021b; Ramonaheng *et al.*, 2021). Adequate compensation for attenuation and scatter should be applied to reduce the source geometry's effect on quantification results (Zeintl *et al.*, 2010; Dewaraja *et al.*, 2012; D'Arienzo *et al.*, 2016). The most reliable method of determining the CF would be to use a source geometry that more acurately represents the attenuation and scatter events in a patient (Dewaraja *et al.*, 2013). There have also been investigations into the effect of changing the volume of interest (VOI) size on CF accuracy where VOIs smaller or larger than the source were used (D'Arienzo *et al.*, 2016; Morphis *et al.*, 2021b). It is advisable that the same VOI delineation method used during the calculation of the CF be applied in patient quantification studies (Dewaraja *et al.*, 2012).

Quantification of tumour activity concentration is also affected by the limited spatial resolution of the system. This limitation causes the PVE, which results in the blurring of the boundary of activity. Objects of interest smaller than two times the system's spatial resolution are affected by PVEs and appear to contain less than the actual activity (due to spill-out) (Saha, 2006, chap. 12; Pretorius and King, 2009). PVEs are partly compensated for when distance-dependent CDR corrections are applied during image reconstruction (Dewaraja *et al.*, 2012). A practical method to perform partial volume corrections (PVC) is to determine recovery coefficients (RC) from sources with simple geometries and known activity concentrations. RCs can either be determined from experimental measurements or Monte Carlo (MC) simulation studies and present the ratio of the measured/estimated activity concentration in a VOI to the true (known) activity concentration. Size-specific RCs can be applied to the recovered activity and can account for the underestimations from small sources, improving the accuracy of activity quantification in small structures such as tumours. Routine practice is to perform PVC with RCs determined from spherical sources with known activities, and then apply these corrections to non-spherical objects of interest. However, this practice has its limits; literature has shown that RCs are not only dependent on object size but also shape (Dewaraja *et al.*, 2012; Brolin *et al.*, 2015).

MC simulation studies have shown to effectively model detector systems and simulating images obtained with specific radioisotopes (Staelens *et al.*, 2003; Sundin

and Ljungberg, 2007; Minarik, Sjögreen Gleisner and Ljungberg, 2008; Ejeh, van Staden and du Raan, 2019; Ramonaheng *et al.*, 2020; Morphis *et al.*, 2021b). Numerous studies have been published where MC codes were used to assess factors that influence the image quality and quantification accuracy of planar and SPECT images (Autret *et al.*, 2005; Asl, Sadremomtaz and Bitarafan-Rajabi, 2013; Dewaraja *et al.*, 2013; Liu, 2013; Ljungberg *et al.*, 2016; Kangasmaa, Constable and Sohlberg, 2018; Zhao *et al.*, 2018; Ramonaheng *et al.*, 2021). SIMIND's ability (the MC code used in this study) to accurately simulate scintillation camera imaging has been extensively reported on (Ljungberg *et al.*, 2002; Toossi *et al.*, 2009; Asl, Sadremomtaz and Bitarafan-Rajabi, 2013; Ejeh, van Staden and du Raan, 2019; Ramonaheng *et al.*, 2020; Morphis *et al.* 2021a). Validation of SIMIND for I-123 using both the LEHR and ME collimators has been reported in **Chapter 2** of this thesis. Using homogenous phantoms, the reconstruction protocol has been optimised in terms of equivalent iterations and SPECT corrections (**Chapter 3**). The next step is to evaluate the accuracy of this optimised protocol by assessing the quantification accuracy of sources in patients.

This study aimed to evaluate the accuracy of SPECT activity quantification for I-123 with both LEHR and ME collimators. The objectives included i) the calculation of calibration factors, ii) the determination of recovery coefficient curves, and iii) the assessment of activity quantification of geometrically simple spheres (mimicking tumours) in voxel-based patient phantoms. SIMIND MC code was used to generate the SPECT projection images for the study.

4.2 Materials and Methods

A validated model of a Siemens Symbia gamma camera, based on a gamma camera located at Universitas Academic Hospital (UAH) (Bloemfontein, South Africa), was modelled using the SIMIND MC code (version 6.1). Details regarding the modelled gamma camera's parameters and the validation tests performed, are described in **Chapter 2**.

CT images (5 mm slice thickness) of a water-filled cylindrical phantom (with a height of 318 mm and internal diameter of 203 mm) (Fluke Biomedical, 2005) were segmented to create a voxel-based digital phantom. The segmentation was performed using ITK-Snap software (version 3.6.0) (Yushkevich *et al.*, 2006), as described by

Ramonaheng *et al.* (2020). Voxel-based phantoms were also created from patient CT images, selected retrospectively from the Nuclear Medicine UAH patient database. The institution's ethical committee approved the use of anonymised patient images for this purpose. Spheres of various diameters were added digitally to these voxel-based phantoms to mimic tumours that could be filled with radioactivity.

All SPECT projections were simulated using I-123 and the modelled gamma camera fitted with the LEHR and ME collimators. These datasets will be referred to as the LEHR and ME datasets. With a step-and-shoot imaging protocol 64 SPECT projections were simulated, using a non-circular rotational orbit. Each projection mimicked a 40 second acquisition time, and the data was stored in a 128×128 matrix size (4.8×4.8 mm^2 pixel size). Images were acquired in a 15% energy window centred over the 159 keV photopeak of I-123. All the simulations were performed with a high number of histories to ensure low simulation noise data (~ 10^9 photons per projection).

The SPECT projections were reconstructed using software developed at Lund University, Sweden (Sjögreen *et al.*, 2005), incorporating the OSEM iterative reconstruction algorithm developed by Frey and Tsui (1996). The reconstruction parameters were based on the optimisation results of eight subsets and eight iterations from **Chapter 3**. The algorithm employed a CT-based attenuation correction, a model-based effective scatter source estimation (ESSE), as well as CDR corrections (Frey and Tsui, 1996; Frey, Humm and Ljungberg, 2012). The CDR correction compensates for the geometric response of the detector as well as for septal scatter and penetration. The ESSE and CDR kernels were pre-generated using SIMIND. The reconstructed SPECT images were analysed using the public domain software *Amide* (Loening and Gambhir 2003). VOIs with dimensions equal to that of the segmented spheres were used to encompass the spheres in the phantom.

4.2.1 Calibration Factor

ITK-Snap was used to digitally add a 113.1 ml sphere (60 mm diameter) to the cylindrical voxel-based phantom (see Figure 4-1) . This sphere size was chosen to limit the PVE's influence on quantification accuracy (Willowson, Bailey and Baldock, 2008; Frey, Humm and Ljungberg, 2012). The sphere in the cylinder was simulated with an I-123 activity concentration of 0.17 MBq/ml (Gilland *et al.*, 1994), with no activity in the background.

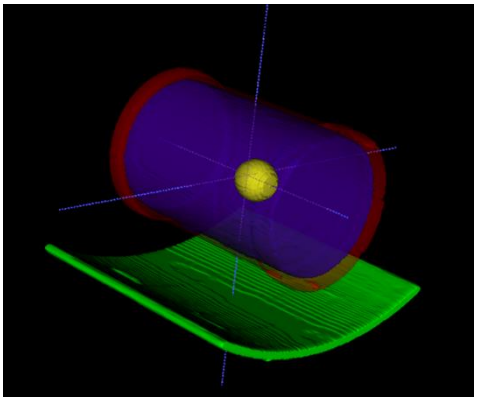

Figure 4-1: *A 3D representation of the segmented 60 mm diameter sphere in the cylindrical phantom.*

The simulations were performed for both LEHR and ME collimators, and the two projection datasets (LEHR and ME) were reconstructed using the above-mentioned optimised OSEM algorithm. A 113 ml spherical VOI encompassing the sphere was used to obtain count statistics (mean count density and fractional voxels). The CF (cps/MBq) was calculated according to equation *(4-1)*,

$$CF = \frac{counts}{time \times Volume \times [True]} \qquad (4\text{-}1)$$

where the $counts$ are determined by multiplying the mean counts per voxel (count density) in the VOI by the number of fractional voxels, $time$ is the simulated acquisition time (s), $Volume$ is the actual volume of the sphere (ml) and $[True]$ is the simulated activity concentration (MBq/ml). A CF was determined for each collimator type.

4.2.2 Recovery Coefficient Curves

RCs were determined for each collimator type by simulating the cylindrical water phantom with nine different sized spheres. The sphere diameters ranged between 15 mm (1.8 ml) and 100 mm (523.6 ml). The same sphere-to-background activity concentration ratio and simulation parameters as in section 4.2.1 were used. RCs depend on object and background activity concentrations (Frey, Humm and Ljungberg, 2012); however, no background actvity was added because it is difficult to predict which source-background ratios will be present in subsequent clinical quantification studies.

As explained before, the SPECT projections were reconstructed, and count statistics were recorded for each sphere for the two collimators' reconstructed SPECT datasets. The VOIs were selected to be equal to the physical size of the spheres. After

reconstruction, the pre-determined CF values (section 4.4.1) were applied to convert the image counts to recovered activity concentration. The RC was determined using equation *(4-2)* and expressed as a fraction of the recovered activity concentration ($[Recovered]$) to the true activity concentration ($[True]$), both reported in MBq/ml.

$$RC = \frac{[Recovered]}{[True]} \qquad (4\text{-}2)$$

The RCs determined for each collimator were plotted as a function of sphere size, and fitted with a mono-exponential equation, such as that given by equation *(4-3)*, yielding a recovery curve. This fit allows interpolation between different sphere sizes.

$$y = a - be^{-cx} \qquad (4\text{-}3)$$

In equation *(4-3)* a, b and c are the curve fitting parameters, x is the sphere diameter (cm), and y the RC value (Willowson, Bailey and Baldock, 2008).

4.3 Patient Phantom Quantification

The third objective of this study was to evaluate the quantification accuracy of simulated tumour sources in a voxel-based patient phantom. Two identically sized spherical sources, mimicking tumours, were digitally added to the voxel-based patient phantom; one was placed between the lungs, and the second was inferior to the liver of the patient phantom. These spheres will be referred to as the lung-sphere and liver-sphere. Two voxel-based patient phantoms were created, as explained by Morphis *et al.* (2021b) and Ramonaheng *et al.* (2021), using the same patient's CT data, each with different size spheres. The sphere diameters for the two phantoms were 30 mm (14.1 ml) and 50 mm (65.5 ml), respectively. The spheres are henceforth refered to as the "3cm spheres" and "5cm spheres" as shown in Figure 4-2. Two scenarios based on different activity ratios were simulated. Both phantoms were simulated with two different sphere-to-background ratios, namely 100:1 and 50:1. The activity concentration ratios of the sphere-to-lung and sphere-to-liver were kept constant at 30:1 and 13:1, respectively.

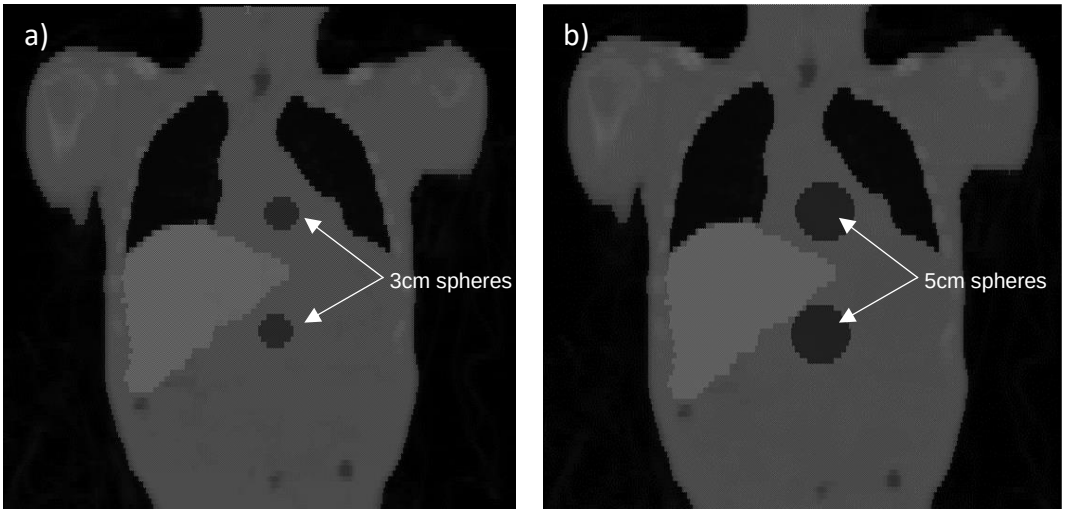

Figure 4-2: *Coronal slices of the two voxel-based patient phantoms with the a) 3cm spheres and b) 5cm spheres positioned between the lungs and inferior to the liver.*

The activity concentrations are based on clinical I-123 mIBG kinetic data recorded 24-hours post-injection, as suggested by (Morphis *et al.*, 2021b). The different sphere-to-background ratios mimic different tumour uptake.

The patient phantoms' LEHR and ME collimated SPECT projections were simulated and reconstructed with the same parameters and protocols as mentioned before. Using VOIs equal to the physical sphere sizes, count statistics were recorded for each patient phantom in each scenario. The collimator specific CFs were applied to determine the activity concentration. PVEs were corrected for, using the relevant RC for the sphere size as obtained from the fitted recovery curve. The quantification error of the recovered activity was calculated as the percentage difference between the recovered activity concentration ($[Recovered]$) and the true simulated activity concentration ($[True]$) (Equation (*4-4*)).

$$Quantification\ Error\ (\%) = \frac{[Recovered]-[True]}{[True]} \times 100 \qquad (4\text{-}4)$$

4.4 Results

4.4.1 Calibration Factor

The CFs determined for each of the collimators are shown in Table 4-1. Axial slices of the reconstructed spheres (LEHR and ME datasets) given in Figure 4-3 show ringing artefacts due to the Gibbs phenomenon on these images.

***Table 4-1**: I-123 calibration factors (cps/MBq) determined for LEHR and ME datasets.*

Calibration Factor	LEHR Dataset	ME Dataset
$\boldsymbol{cps/MBq}$	74.2	102.4

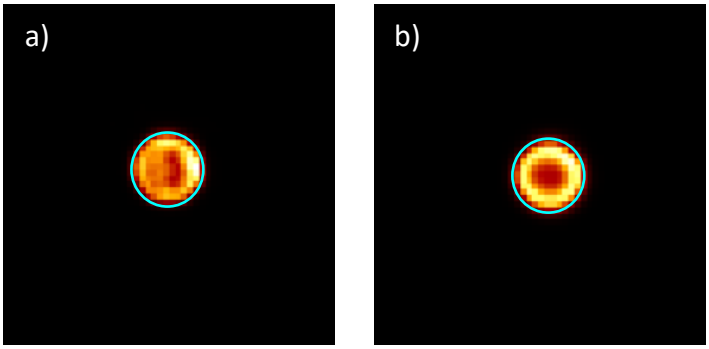

***Figure 4-3:** Axial slice through the 6cm sphere used to determine the calibration factor for the a) LEHR and b) ME datasets. ROI placement indicated in blue.*

4.4.2 Recovery Coefficient Curves

The RCs obtained for the LEHR and ME datasets and their respective curve fits are presented in Figure 4-4. The fitted curves, generated by equation *(4-3)*, are displayed as solid lines for the LEHR and ME datasets. R^2 values of greater than 0.9 were obtained for both collimators. From Figure 4-4, it can be seen that, for the LEHR dataset, more than 90% of the true activity concentration is recovered for spheres with a diameter of 4.0 cm and larger. The recovered activity concentration is comparable for the same sphere size in the ME dataset (RC = 0.89).

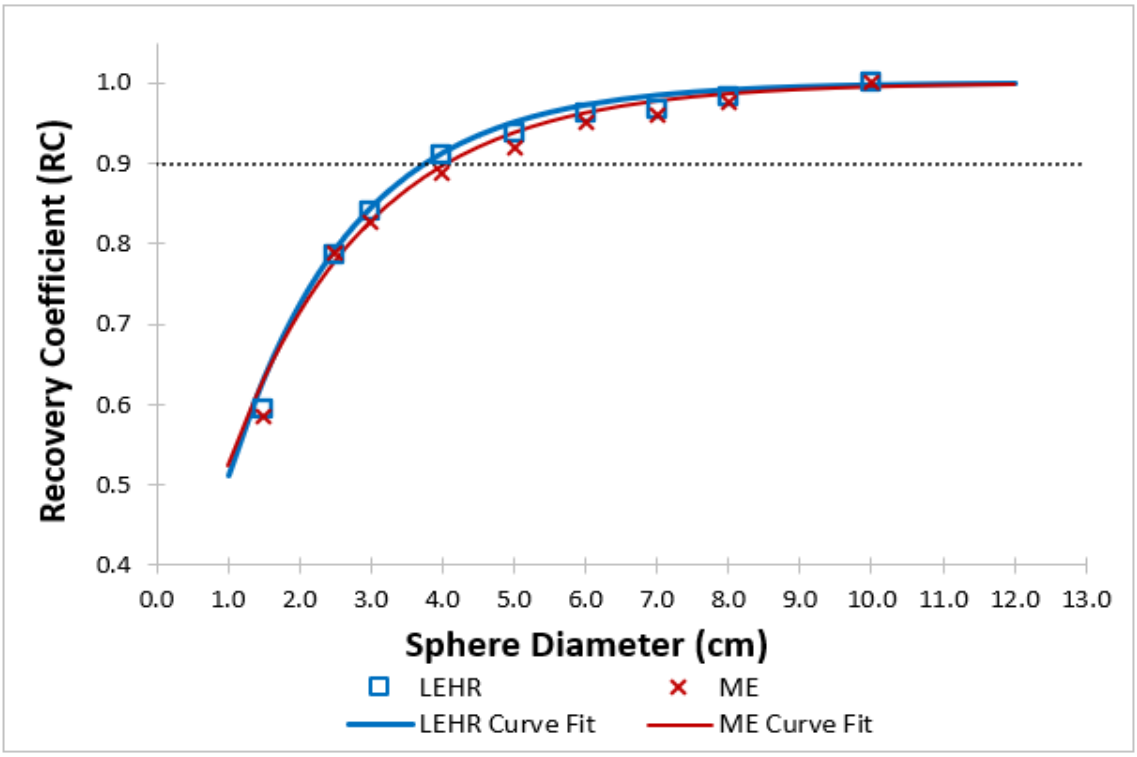

Figure 4-4: *RC as a function of sphere diameter determined for I-123 with LEHR (blue) and ME (red) collimators, with the fitted RC curves depicted as solid lines.*

The curves indicate the fraction of the true I-123 activity concentration that can be recovered per sphere size. These curves were used to correct for PVEs when quantifying the spheres in the patient phantoms.

4.4.3 Patient Quantification

Segmented and reconstructed transverse slices of the two voxel-based patient phantoms with the 3cm and 5cm spheres are shown in Figure 4-5 and Figure 4-6, respectively.

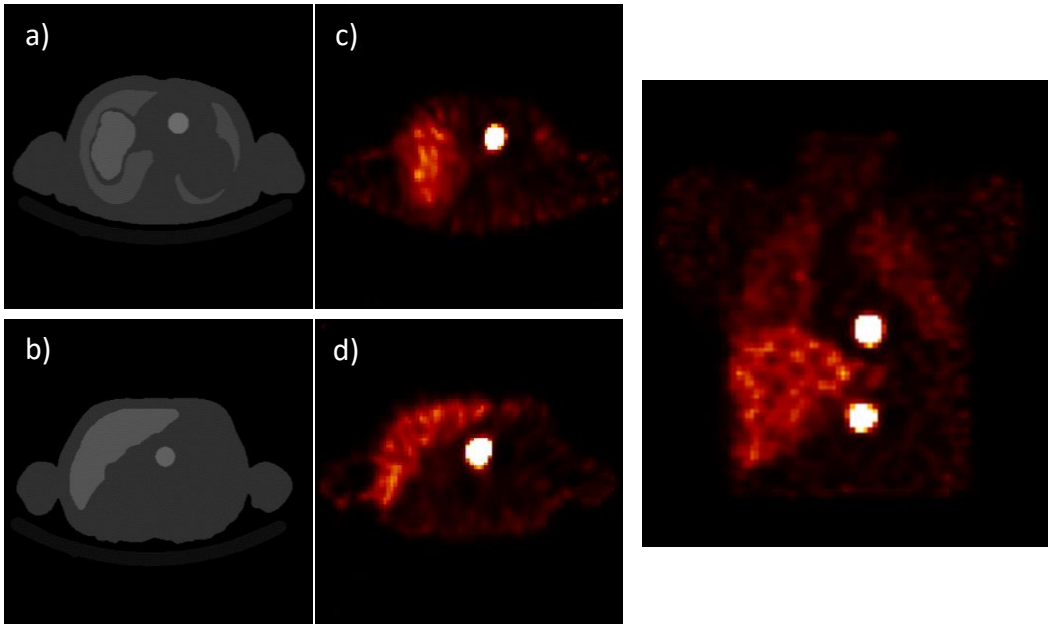

Figure 4-5: *Transverse slices of the segmented patient phantom indicating the positions of the (a) 3cm lung-sphere and (b) 3cm liver-sphere. Transverse SPECT reconstructed slices through the (c) 3cm lung-sphere and (d) 3cm liver-sphere, along with (e) a coronal reconstructed slice showing both 3cm spheres in the 100:1 activity scenario.*

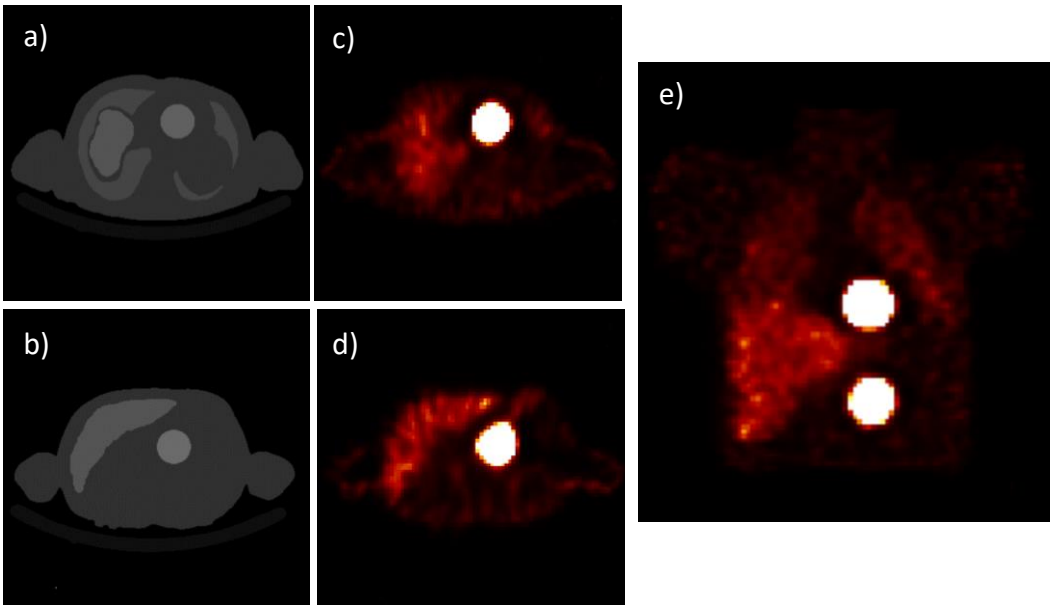

Figure 4-6: *Transverse slices of the segmented patient phantom indicating the positions of the (a) 5cm lung-sphere and (b) 5cm liver-sphere. Transverse SPECT reconstructed slices through the (c) 5cm lung-sphere and (d) 5cm liver-sphere, along with (e) a coronal reconstructed slice showing both 5cm spheres in the 100:1 activity scenario.*

Figure 4-7 shows the quantification errors determined for the 3cm and 5cm spheres in these two patient phantoms simulated with the 100:1 and 50:1 activity concentrations.

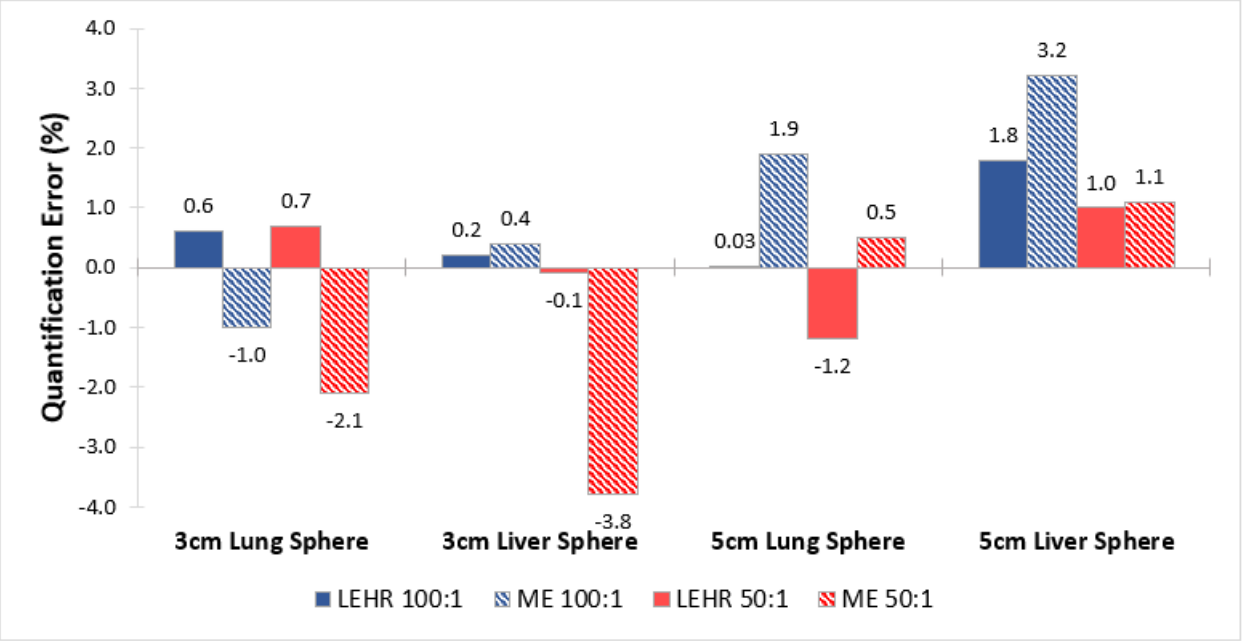

***Figure 4-7**: Quantification errors (%) determined for patient phantom spheres simulated with different sphere-to-background activity concentration ratios for I-123 LEHR and ME SPECT data.*

The LEHR dataset in the 50:1 scenario shows only minor differences between the true and recovered activity concentrations for the 3cm spheres (quantification error ≤ 0.7%). The 50:1 ratio ME dataset resulted in underestimated activity concentration values for both the 3cm lung- and liver-sphere (quantification error ≤ 3.8%). The quantification error of the 5cm spheres in both datasets did not exceed 1.2%.

In the 100:1 scenario, the LEHR dataset had quantification errors of less than 2% for the 3cm and 5cm spheres. The quantification error of the 3cm spheres in ME dataset did not surpass 1.0%, while the 5cm lung- and liver-spheres had quantification errors smaller than 3.2%.

In this study, the 3cm and 5cm spheres have quantification errors less than 3.8% for both the LEHR and ME collimators, independent of their placement within the patient phantom or the sphere-to-background activity ratio.

4.5 Discussion

4.5.1 Calibration Factor

CFs are affected by the gamma camera's efficiency with regards to the specific radioisotope, the collimator fitted during acquisition, the energy window used (Zhao *et al.*, 2018), the corrections applied, and the dimensions of the VOI used to record count statistics (Ramonaheng *et al.*, 2021). The factors that influence the CF imply that the CF determined here can only be applied clinically if the same gamma camera, collimator, isotopes, imaging- and reconstruction protocols as well as analysis methods were used during acquisitions.

The results in Table 4-1 were determined from a sphere with known activity concentration in a cylindrical water phantom using a VOI equal to the physical sphere size. A study by Morphis *et al.* (2021b) reported a CF value of 84.4 cps/MBq for I-123 studies acquired with a LEHR collimator, and 118.2 cps/MBq for the ME collimator. The reason for the difference in comparison to the study by Morphis *et al.* (2021b) is that, unlike in this study, count statistics were obtained using a VOI that had a 3 cm margin added to the physical size of the sphere. Using a larger VOI can complicate the quantification of objects in clinical studies where background activity can erroneously contribute to the activity within the quantified structures. Using a uniformed delineation approach for the quantified spheres, defining the VOI for the CF as the physical dimensions of the sphere proved helpful. The sphere's physical size of 113.1 ml was also selected in order to keep the PVEs to a minimum.

Despite the Gibbs artefact being present in the reconstructed spheres, determining a CF with this specific VOI delineation was still possible.

4.5.2 Recovery Coefficients

It is known that RCs depend on source shape, size and source-to-background activity ratios; therefore applying simple geometry RCs to irregular sources in various background concentrations may result in larger quantification errors (Dewaraja, Ljungberg and Koral, 2001; Ritt *et al.*, 2011). RCs need to be determined for each camera/collimator and data acquisition/reconstruction combination (Li *et al.*, 2017).

In this study, PVC was performed using RCs determined from different-sized spherical sources in a cold background (Figure 4-4). The plot of the gamma camera's RCs is as predicted, with at least 90% activity concentration recovered (RC > 0.9) for spheres 4 cm and larger. Morphis *et al.* (2021b) similarly determined RCs for LEHR and ME collimated I-123 spheres; however, they reported RC > 0.9 for sphere sizes of 5 cm and larger. The difference in RC can be attributed to the VOI delineation used; they used a circular VOI with a diameter equal to the physical sphere size, while their CF was determined from a VOI with an additional 3 cm margin.

Even though RCs were determined from simple source geometries in this study, they sufficiently reduced the object-size dependence and improved quantification accuracy.

4.5.3 Patient Quantification

Figure 4-7 shows that the largest quantification error found for the sphere in the activity-filled background is 3.8%. Du, Tsui and Frey, (2006) determined an absolute quantification error of ± 3.5% for I-123 SPECT brain studies. Shcherbinin (2008) reported a 3% to 5% quantification error of I-123 filled sources in a torso phantom, using similar corrections as in this study. I-123 absolute quantification errors of up to 10% have been reported for spheres with diameters ranging between 17- and 37 mm (Brady and Shulkin, 2019). Morphis *et al.* (2021b) reported quantification errors of up to 5.4% for LEHR and ME collimated I-123 spheres in patient phantom studies.

The quantification errors determined in this study for I-123 LEHR and ME phantom patient studies are similar to, and in some cases, smaller than what has been published in scientific literature. It should be noted that different phantoms, imaging parameters, activity concentrations, sphere sizes and VOI delineations, as well as energy resolution models were used in the studies reported in the literature. The smaller quantification errors found in this study could be attributed to the VOI definition and optimisation of the SPECT reconstruction protocol.

4.6 Conclusion

Assumptions made in this study were: the tumours quantified are geometrically uniform, the borders are well distinguished from neighbouring organs/ healthy tissue, and the background activity uptake is uniform throughout the organs. In clinical situations, this is will not necessarily be true.

The voxel-based patient phantoms used during this study were created from a single patient's CT data, implying that the positioning and size of the anatomy were the same throughout. The patient studies also lacked clinically realistic movement artefacts brought on by the patient's breathing and organ movement. This study can be expanded by using CT data from more patients to create voxel-based patient phantoms with varying anatomy. Should access to patient data be limited, hybrid phantoms such as the 4D XCAT (Segars *et al.*, 2010) can also be implemented to incorporate clinically realistic factors such as patient movement and varying anatomy.

Further studies can also be performed where the RC simulation parameters are appropriately adjusted for clinically realistic source-background activity ratios, and irregularly shaped tumours are quantified using the same optimised reconstruction protocol.

Based on this comparative study, accurate quantification of I-123 images can be achieved clinically with either LEHR or ME collimators, if the appropriate SPECT corrections and reconstruction protocols are implemented. Sufficient correction must be applied for image degrading factors such as attenuation, scatter, and CDR (including geometric response, septal penetration and scatter).

4.7 References

Asl, M. N., Sadremomtaz, A. and Bitarafan-Rajabi, A. (2013) 'Evaluation of six scatter correction methods based on spectral analysis in 99mTc SPECT imaging using SIMIND Monte Carlo simulation', *Journal of Medical Physics*, 38(4), pp. 189–198. doi: 10.4103/0971-6203.121197.

Autret, D., Bitar, A., Ferrer, L., Lisbona, A. and Bardiès, M. (2005) 'Monte Carlo Modeling of Gamma Cameras for I-131 Imaging in Targeted Radiotherapy', *Cancer Biotherapy and Radiopharmaceuticals*, 20(1), pp. 77–84. doi: 10.1089/cbr.2005.20.77.

Brady, S. L. and Shulkin, B. L. (2019) 'Analysis of quantitative [I-123] mIBG SPECT/CT in a phantom and in patients with neuroblastoma', *EJNMMI Physics*, 6(31), p. 14. doi: 10.1186/s40658-019-0267-6.

Brolin, G., Gustafsson, J., Ljungberg, M. and Sjögreen Gleisner, K. (2015) 'Pharmacokinetic digital phantoms for accuracy assessment of image-based dosimetry in 177 Lu-DOTATATE peptide receptor radionuclide therapy', *Physics in Medicine and Biology*, 60(15), pp. 6131–6149. doi: 10.1088/0031-9155/60/15/6131.

D'Arienzo, M., Cazzato, M., Cozzella, M. L., Cox, M., D'Andrea, M., Fazio, A., Fenwick, A., Iaccarino, G., Johansson, L., Strigari, L., Ungania, S. and De Felice, P. (2016) 'Gamma camera calibration and validation for quantitative SPECT imaging with 177Lu', *Applied Radiation and Isotopes*. Elsevier, 112, pp. 156–164. doi:

10.1016/j.apradiso.2016.03.007.

Dewaraja, Y. K., Frey, E. C., Sgouros, G., Brill, A. B., Roberson, P., Zanzonico, P. B. and Ljungberg, M. (2012) 'MIRD Pamphlet no. 23: Quantitative SPECT for Patient-Specific 3-Dimensional Dosimetry in Internal Radionuclide Therapy', *Journal of Nuclear Medicine*, 53(8), pp. 1310–1325. doi: 10.2967/jnumed.111.100123.

Dewaraja, Y. K., Ljungberg, M., Green, A. J., Zanzonico, P. B., Frey, E. C., Bolch, W. E., Brill, A. B., Dunphy, M., Fisher, D. R., Howell, R. W., Meredith, R. F., Sgouros, G. and Wessels, B. W. (2013) 'MIRD Pamphlet No. 24: Guidelines for Quantitative 131I SPECT in Dosimetry Applications', *Journal of Nuclear Medicine*, 54(12), pp. 2182–2188. doi: 10.2967/jnumed.113.122390.

Dewaraja, Y. K., Ljungberg, M. and Koral, K. F. (2001) 'Monte Carlo evaluation of object shape effects in iodine-131 SPET tumor activity quantification', *European Journal of Nuclear Medicine*, 28(7). doi: 10.1007/s002590100551.

Du, Y., Tsui, B. M. W. and Frey, E. C. (2006) 'Model-based compensation for quantitative 123 I brain SPECT imaging', *Physics in Medicine and Biology*, 51, pp. 1269–1282. doi: 10.1088/0031-9155/51/5/016.

Ejeh, J. E., van Staden, J. A. and du Raan, H. (2019) 'Validation of SIMIND Monte Carlo Simulation Software for Modelling a Siemens Symbia T SPECT Scintillation Camera', in *World Congress on Medical Physics and Biomedical Engineering*. Springer Singapore, pp. 573–576. doi: 10.1007/978-981-10-9035-6.

Fluke Biomedical (2005) 'Nuclear Associates 76-823, 76-824 & 76-825 PET/SPECT Phantom Source Tank,Phantom Inserts and Cardiac Insert', *Manual*, p. 10. Available at: https://www.manualsdir.com/manuals/767906/fluke-biomedical-76-823.html.

Frangos, S. and Buscombe, J. R. (2019) 'Why should we be concerned about a "g"?', *European Journal of Nuclear Medicine and Molecular Imaging*, 46(519), p. 1. doi: 10.3345/cep.2020.00521.

Frey, E. C., Humm, J. L. and Ljungberg, M. (2012) 'Accuracy and precision of radioactivity quantification in nuclear medicine images', *Seminars in Nuclear Medicine*. Elsevier Inc., 42(3), pp. 208–218. doi: 10.1053/j.semnuclmed.2011.11.003.

Frey, E. C. and Tsui, B. M. W. (1996) 'A New Method for Modeling the Spatially-Variant, Object-Dependent Scatter Response Function in SPECT', *IEEE Nuclear Science Symposium Conference Record*, pp. 1082–1086.

Gilland, D. R., Jaszczak, R. J., Turkington, T. G., Greer, K. L. and Coleman, R. E. (1994) 'Volume and Activity Quantitation with I-123 SPECT', *Journal of Nuclear Medicine*, 35(10), pp. 1707–1713. Available at: https://jnm.snmjournals.org/content/jnumed/35/10/1707.full.pdf.

Kangasmaa, T. S., Constable, C. and Sohlberg, A. O. (2018) 'Evaluation of quantitative 123 i and 131 i SPECT with Monte Carlo-based down-scatter compensation', *Nuclear Medicine Communications*, 39(12), pp. 1097–1102. doi: 10.1097/MNM.0000000000000920.

Kushner, B. H., Kramer, K., Modak, S. and Cheung, N. K. V. (2009) 'Sensitivity of surveillance studies for detecting asymptomatic and unsuspected relapse of high-risk neuroblastoma', *Journal of Clinical Oncology*, 27(7), pp. 1041–1046. doi:

10.1200/JCO.2008.17.6107.

Laboratoire National Henri Becquerel (2004) *Table de Radionucléides - I-123*. Available at: http://www.lnhb.fr/nuclides/I-123_tables.pdf (Accessed: 5 November 2018).

Laboratoire National Henri Becquerel (2014) *Table de Radionucléides - I-131*. Available at: http://www.lnhb.fr/nuclides/I-131_tables.pdf (Accessed: 20 November 2020).

Li, T., Ao, E. C. I., Lambert, B., Brans, B., Vandenberghe, S. and Mok, G. S. P. (2017) 'Quantitative Imaging for Targeted Radionuclide Therapy Dosimetry - Technical Review', *Theranostics*, 7(18), pp. 4551–4565. doi: 10.7150/thno.19782.

Liu, Z. (2013) *Monte Carlo Scatter Correction for SPECT*. Doctoral Dissertation, University of Massachusetts Lowell.

Ljungberg, M., Celler, A., Konijnenberg, M. W., Eckerman, K. F., Dewaraja, Y. K. and Sjögreen-Gleisner, K. (2016) 'MIRD Pamphlet no. 26: Joint EANM/MIRD Guidelines for Quantitative 177Lu SPECT Applied for Dosimetry of Radiopharmaceutical Therapy', *Journal of Nuclear Medicine*, 57(1), pp. 151–162. doi: 10.2967/jnumed.115.159012.

Ljungberg, M., Sjögreen, K., Liu, X., Frey, E., Dewaraja, Y. and Strand, S.-E. (2002) 'A 3-Dimensional Absorbed Dose Calculation Method Based on Quantitative SPECT for Radionuclide Therapy: Evaluation for 131I Using Monte Carlo Simulation ', *Journal of Nuclear Medicine* , 43(8), pp. 1101–1109. Available at: http://jnm.snmjournals.org/content/43/8/1101.abstract.

Loening, A. M. and Gambhir, S. S. (2003) 'AMIDE: A Free Software Tool for Multimodality Medical Image Analysis', *Molecular Imaging*, 2(3), pp. 131–137. doi: 10.1162/153535003322556877.

Marquis, H., Deidda, D., Gillman, A., Willowson, K. P., Gholami, Y., Hioki, T., Eslick, E., Thielemans, K. and Bailey, D. L. (2021) 'Theranostic SPECT reconstruction for improved resolution: application to radionuclide therapy dosimetry', *EJNMMI Physics*, 8(1), pp. 1–17. doi: 10.1186/s40658-021-00362-x.

Matthay, K. K. (1997) 'Neuroblastoma: biology and therapy', *Oncology (Williston Park, N.Y.)*, 11(12), pp. 1857—66; discussion 1869—72, 1875. Available at: http://europepmc.org/abstract/MED/9436190.

Matthay, K. K., Shulkin, B., Ladenstein, R., Michon, J., Giammarile, F., Lewington, V., Pearson, A. D. J. and Cohn, S. L. (2010) 'Criteria for evaluation of disease extent by 123 I-metaiodobenzylguanidine scans in neuroblastoma: A report for the International Neuroblastoma Risk Group (INRG) Task Force', *British Journal of Cancer*. Nature Publishing Group, 102(9), pp. 1319–1326. doi: 10.1038/sj.bjc.6605621.

Minarik, D., Sjögreen Gleisner, K. and Ljungberg, M. (2008) 'Evaluation of quantitative Y-90 SPECT based on experimental phantom studies', *Physics in Medicine and Biology*, 53(20), pp. 5689–5703. doi: 10.1088/0031-9155/53/20/008.

Morphis, M., van Staden, J. A., du Raan, H. and Ljungberg, M. (2021a) 'Modelling of energy-dependent spectral resolution for SPECT Monte Carlo simulations using SIMIND', *Heliyon*. Elsevier Ltd, 7(January), p. e06097. doi:

10.1016/j.heliyon.2021.e06097.

Morphis, M., van Staden, J. A., du Raan, H. and Ljungberg, M. (2021b) 'Evaluation of Iodine-123 and Iodine-131 SPECT Activity Quantification: a Monte Carlo study', *EJNMMI Physics*, 8(1). doi: doi.org/10.1186/s40658-021-00407-1.

Parisi, M. T., Eslamy, H., Park, J. R., Shulkin, B. L. and Yanik, G. A. (2016) 'I-131-Metaiodobenzylguanidine Theranostics in Neuroblastoma: Historical Perspectives; Practical Applications', *Seminars in Nuclear Medicine*. Elsevier, 46(3), pp. 184–202. doi: 10.1053/j.semnuclmed.2016.02.002.

Pretorius, P. H. and King, M. A. (2009) 'Diminishing the impact of the partial volume effect in cardiac SPECT perfusion imaging', *Medical Physics*, 36(1), pp. 105–115. doi: 10.1118/1.3031110.

Ramonaheng, K., van Staden, J. A., du Raan, H. and du Raan, H. (2020) 'Validation of a Monte Carlo modelled gamma camera for Lutetium-177 imaging', *Applied Radiation and Isotopes*. Elsevier Ltd, 163, pp. 1–9. doi: 10.1016/j.apradiso.2020.109200.

Ramonaheng, K., van Staden, J. A., du Raan, H. and du Raan, H. (2021) 'The effect of calibration factors and recovery coefficients on 177Lu SPECT activity quantification accuracy: a Monte Carlo study', *EJNMMI Physics*, 8(1), p. 23. doi: 10.1186/s40658-021-00365-8.

Ritt, P., Vija, H., Hornegger, J. and Kuwert, T. (2011) 'Absolute quantification in SPECT', *European Journal of Nuclear Medicine and Molecular Imaging*, 38(Suppl 1), pp. 69–77. doi: 10.1007/s00259-011-1770-8.

Saha, G. B. (2006) *Physics and Radiobiology of Nuclear Medicine*. 3rd edn. Cleveland: Springer Science and Business Media, Inc. doi: 10.1007/978-0-387-36281-6.

Segars, W. P., Sturgeon, G., Mendonca, S., Grimes, J. and Tsui, B. M. W. (2010) '4D XCAT Phantom for Multimodality Imaging Research', *Medical Acupuncture*, 37(9), pp. 4902–4915. doi: 10.1118/1.3480985.

Shcherbinin, S. (2008) 'Accuracy of Quantitative Reconstructions in SPECT / CT Imaging', *Physics in Medicine and Biology*, 53, pp. 4595–4604. doi: 10.1088/0031-9155/53/17/009.

Sjögreen, K., Ljungberg, M., Wingårdh, K., Minarik, D. and Strand, S. (2005) 'The LundADose Method for Planar Image Activity Quantification and Absorbed-Dose Assessment in Radionuclide Therapy', *Cancer Biotherapy & Radiopharmaceuticals*, 20(1), pp. 92–97. Available at: https://books.google.co.za/books?id=YzzNBQAAQBAJ&dq=Monte+Carlo+calculations+in+nuclear+medicine&lr=.

Staelens, S., Strul, D., Santin, G., Vandenberghe, S., Koole, M., D'Asseler, Y., Lemahieu, I. and Van de Walle, R. (2003) 'Monte Carlo Simulations of a Scintillation Camera Using GATE: Validation and Application Modelling', *Physics in Medicine and Biology*, 48(18), pp. 3021–3042. doi: 10.1088/0031-9155/48/18/305.

Sundin, K. and Ljungberg, M. (2007) 'SIMIND Based Pinhole Imaging: Development and Validation', *IEEE Nuclear Science Symposium Conference Record*, 5, pp. 3998–4005. doi: 10.1109/NSSMIC.2007.4436991.

Theerakulpisut, D., Raruenrom, Y., Wongsurawat, N. and Somboonporn, C. (2018) 'Value of SPECT/CT in Diagnostic I-131 MIBG Scintigraphy in Patients with Neuroblastoma', *Nuclear Medicine and Molecular Imaging*, 52(5), pp. 350–358. doi: 10.1007/s13139-018-0532-y.

Toossi, M. T. B., Islamian, J. P., Momennezhad, M., Ljungberg, M. and Naseri, S. H. (2009) 'SIMIND Monte Carlo simulation of a single photon emission CT', *Journal of Medical Physics*, 35(1), pp. 42–47. doi: 10.4103/0971-6203.55967.

Vallabhajosula, S. (2009) *Molecular Imaging - Radiopharmaceuticals for PET and SPECT*. New York: Springer International. doi: 10.1007/978-3-540-76735-0.

Wahl, R. L., Ahuja, S. and Clarke, B. (2021) 'Current Landscape of Radiopharmaceutical Therapies: SNMMI Therapy Task Force Survey', *Journal of Medical Physics*, 62(5), pp. 11–16.

Willowson, K., Bailey, D. L. and Baldock, C. (2008) 'Quantitative SPECT reconstruction using CT-derived corrections', *Physics in Medicine and Biology*, 53(12), pp. 3099–3112. doi: 10.1088/0031-9155/53/12/002.

Yushkevich, P. A., Piven, J., Hazlett, C., Smith, G., Ho, S., Gee, J. C. and Gerig, G. (2006) 'User-guided 3D active contour segmentation of anatomical structures : Significantly improved efficiency and reliability', *NeuroImage*, 31, pp. 1116–1128. doi: 10.1016/j.neuroimage.2006.01.015.

Zeintl, J., Vija, A. H., Yahil, A., Hornegger, J. and Kuwert, T. (2010) 'Quantitative Accuracy of Clinical Tc-99m SPECT / CT Using Ordered-Subset Expectation Maximization with 3-Dimensional Resolution Recovery , Attenuation , and Scatter Correction', *Journal of Nuclear Medicine*, 51(6), pp. 921–929. doi: 10.2967/jnumed.109.071571.

Zhao, W., Esquinas, P. L., Hou, X., Uribe, C. F., Gonzalez, M., Beauregard, J., Dewaraja, Y. K. and Celler, A. (2018) 'Determination of gamma camera calibration factors for quantitation of therapeutic radioisotopes', *EJNMMI Physics*, 5(8), pp. 1–16.

Chapter 5: Summary and Future Work

Table of Contents

5.1 Summary

I-123 has been proven to be an effective diagnostic agent when used in radiopharmaceutical therapy. When labelling I-123 with metaiodobenzylguanidine (mIBG), it can be used to diagnose heart disease, brain tumours and locate neuroblastomas metastases. However, I-123 has a complicated decay scheme that includes ideal imaging emissions (159.0 keV) along with high-energy photon emissions (> 440.0 keV). Using LEHR collimators during I-123 SPECT studies results in images with a high resolution. However, the high-energy photons of I-123 can penetrate the collimator septa and contribute to reduced image contrast and quantification accuracy. When the goal of the clinical investigation is to determine the amount of radioactivity contained within an object of interest (patient), it is preferable to use ME collimators rather than LEHR collimators. However, the disadvantage is a reduction in resolution as a result of the thicker collimator septa and hole size. The collimator choice for I-123 diagnostic imaging is dependent on the clinical need, the type of study that needs to be performed and the resources available.

The aim of the study was to assess and compare the quantification accuracy of I-123 LEHR and ME SPECT images after an optimised reconstruction protocol was implemented during reconstruction. Most clinical facilities have access to LEHR collimators, but not necessarily ME collimators. Therefore, the study focused on whether similar image quality and quantification accuracy could be achieved using LEHR and ME collimators. The study was based on SIMIND MC simulations of voxel-based phantoms.

The first part of the study used MC simulations to generate a virtual gamma camera model for emission tomography. This was done by creating and validating a SIMIND MC model of the Siemens Symbia T16 gamma camera for I-123 SPECT imaging, using the LEHR and ME collimators and a constant energy resolution value. The validation was based on the gamma camera performance tests of intrinsic and system energy resolution, system spatial resolution and sensitivity. The SPECT image quality attained with an image quality phantom for each collimator dataset was also compared. This study showed that the SIMIND MC code could accurately simulate I-123 images obtained with both the LEHR and ME collimators to within 3.4%, 6.4% and 5.3% for the energy resolution, system spatial resolution and planar system sensitivity, respectively. Thus, the SIMIND MC code can be used with

confidence to simulate LEHR and ME NM I-123 images in order to optimise imaging processing and activity quantification.

The validated MC model from the first article (**Chapter 2**) was used to simulate I-123 SPECT images of simple geometry sources and an image quality (IQ) phantom using the LEHR and ME collimators.

The second part of the study (**Chapter 3**) optimised the OSEM reconstruction protocol in terms of equivalent iterations (EI) and SPECT corrections. This was done to optimise the OSEM iterative reconstruction algorithm parameters in terms of count density recovery, image noise, contrast, resolution and linearity. The influence of SPECT corrections on LEHR and ME I-123 images was also evaluated by comparing the image quality of LEHR and ME SPECT corrected images. The results of the recovered count densities were used to determine the optimal number of EI to implement during the reconstruction process. The IQ phantom images were reconstructed with the optimal number of EI to assess the IQ parameters of uniformity, contrast, resolution and linearity. These images were also reconstructed with various combinations of SPECT corrections. When attenuation, scatter, and collimator detector response corrections were applied, the image quality of LEHR and ME images (reconstructed with 64 EI) was comparable in terms of %RMS, contrast, and resolution. As a result, I-123 SPECT studies for quantification could be acquired using either LEHR or ME collimators. This assumption theory was further explored in **Chapter 4.**

In the final part of the study, LEHR and ME I-123 SPECT simulations of a sphere in water was reconstructed using the optimised reconstruction protocol. The simulations were performed using the LEHR and ME collimators. A collimator-specific calibration factor (CF) was determined from the counts recovered from the reconstructed sphere image. This CF was applied to counts recovered from simulation images of a voxel-based patient phantom to convert the counts to activity concentration. Partial volume effects were compensated for using appropriate recovery coefficients. The quantification of reconstructed LEHR and ME I-123 SPECT patient phantom studies resulted in quantification errors no greater than 3.8%. These results indicate that accurate quantification of I-123 images can be achieved clinically with either LEHR or ME collimators, if the appropriate SPECT

corrections and reconstruction protocols are implemented. Sufficient correction must be applied for image degrading factors such as attenuation, scatter, and collimator-detector response (including geometric response, septal penetration and scatter).

5.2 Future Work

It should be noted that the patient phantoms used in this study were based on clinical CT data; however some assumptions were made: the tumours quantified in the patient-phantoms were geometrically uniform, the borders were well distinguished from neighbouring organs/ healthy tissue, and the background activity uptake were uniform throughout the organs. CT data from a single patient was used, therefore no anatomical variation was included. The patient studies also lacked clinically realistic movement artefacts brought on by the patient's breathing, organ movement and shifting. This study can be expanded by using CT data from numerous patients to create voxel-based patient phantoms with varying anatomy. Should access to patient data be limited, hybrid phantoms such as the 4D XCAT (Segars *et al.*, 2010) can also be implemented, which have the advantage to incorporate clinically realistic factors such as patient movement and varying anatomy.

Further studies can be performed where recovery coefficients are determined from phantom studies simulated with background activity. The processing protocols could also be applied to phantom studies of irregularly shaped tumours and non-uniform radioactivity distribution.

SIMIND could also be validated for the GE Discovery NM/CT 670 system used at National District Hospital in Bloemfontein, South Africa. This would enable us to assess the feasibility of using LEHR collimators for I-123 SPECT studies on the GE Discovery NM/CT 670 system. Image quality and quantitative accuracy of SPECT images acquired with LEHR and ME collimators with the Siemens Symbia SPECT/CT and GE Discovery NM/CT 670 systems can also be compared with MC simulations.

Finally, the enhanced image quality and quantitative accuracy for both LEHR and ME collimators shown in this study can serve as a platform for future research aimed

at improving diagnostic accuracy for a range of routine clinical studies conducted with I-123.

Appendices

Contents

***Figure A-1**: Screenshots of the Change program indicating flags and parameters used in SIMIND to determine geometry and setup of simulations. Parameters for the simulations of energy resolution, spatial resolution (at 100 mm) and system sensitivity are shown.*

C H A N G E: Scintillation camera parameters	Energy Resolution	Planar Spatial Resolution (100 mm)	Planar System Sensitivity
1 - Photon energy.....keV:	-159.0000	-158.9700	-159.0000
2 - Source: half-length Source.....cm:	13.2500	1.8000	13.2500
3 - Source: half-width Source.....cm:	40.0000	1.8000	40.0000
4 - Source: half-height Source.....cm:	40.0000	1.8000	40.0000
5 - Phantom: half-length Phantom.....cm:	16.2000	19.6000	18.3750
6 - Phantom: half-width Phantom.....cm:	40.0000	0.5000	40.0000
7 - Phantom: half-height Phantom.....cm:	40.0000	0.5000	40.0000
8 - Crystal: half-length/Radius.....cm:	22.7500	100.0000	22.7500
9 - Crystal: thickness.....cm:	0.9500	0.9500	0.9500
10 - Crystal: half-width..[0=Circular].....cm:	29.5500	29.5500	29.5500
11 - Backscattering material: Thickness.....cm:	40.0000	40.0000	40.0000
12 - Height to detector surface.....cm:	125.0000	10.0000	10.0000
13 - Thickness of cover.....cm:	0.1000	0.1000	0.1000
14 - Phantom type.....:	-5.0000	-5.0000	-5.0000
15 - Source type.....:	-5.0000	-5.0000	-5.0000
16 - Shift source in x-direction.....cm:	0.0000	0.0000	0.0000
17 - Shift source in y-direction.....cm:	0.0000	0.0000	0.0000
18 - Shift source in z-direction.....cm:	0.0000	0.0000	0.0000
19 - Photon direction.....deg:	3.0000	3.0000	3.0000
20 - Upper window threshold.....keV:	-15.0000	-15.0000	-15.0000
21 - Lower window threshold.....keV:	-15.0000	-15.0000	-15.0000
22 - Energy resolution ...[140 keV]..... %:	-9.1000	-9.0100	-8.9100
23 - Intrinsic resolution [140 keV].....cm:	0.3800	0.3800	0.3800
24 - Emitted photons per decay.....:	0.8330	0.8325	0.8850
25 - Source activity.....MBq:	93.1450	89748.0000	28563.0000
26 - Number of photon histories * 1E6.....:	10.0000	1.0000	10.0000
27 - keV/channel.....keV:	1.0000	1.0000	1.0000
28 - Pixel size in simulated image.....cm:	0.1200	0.1200	0.2400
29 - SPECT: No of projections.....:	1.0000	1.0000	1.0000
30 - SPECT: Rotation [0=-360,1=-180,2=360,3=180] :	0.0000	0.0000	0.0000

	Energy Resolution	Planar Spatial Resolution (100 mm)	Planar System Sensitivity
C H A N G E: Non-homogeneous phantom and SPECT parameters			
31 - Pixel size in density maps..... cm:	0.0780	0.0780	0.0980
32 - Orientation of the density map phantom.....:	0.0000	0.0000	0.0000
33 - Start image when reading density maps.....:	1.0000	1.0000	1.0000
34 - Number of CT-images.....:	162.0000	196.0000	245.0000
35 - Density limit defining the border..... g/cm3:	0.0100	0.0000	0.0100
36 - Shift density map relative origin (y-dir).cm:	0.0000	0.0000	0.0000
37 - Shift density map relative origin (z-dir).cm:	0.0000	0.0000	0.0000
38 - Step size for photon path simulation.....cm:	0.1000	0.0900	0.1000
39 - Shift density map relative origin.(x-dir).cm:	0.0000	0.0000	0.0000
40 - Density threshold between soft & bone..g/cm3:	0.0000	0.0000	0.0000
41 - SPECT: Starting angle..... degree:	0.0000	0.0000	0.0000
42 - SPECT: Orbital rotation fraction.....:	-125.0000	-10.0000	-10.0000
43 - Camera offset in x-direction.....cm:	0.0000	0.0000	0.0000
44 - Camera offset in y-direction.....cm:	0.0000	0.0000	0.0000
45 - Code definitions in generic Zubal phantom...:	1.0000	1.0000	1.0000
C H A N G E: Imaging parameters and other settings			
76 - Matrix size image I .....:	512.0000	512.0000	256.0000
77 - Matrix size image J .....:	512.0000	512.0000	256.0000
78 - Matrix size density map I .....:	512.0000	512.0000	512.0000
79 - Matrix size source map I .....:	512.0000	512.0000	512.0000
80 - Energy spectra channels .....:	1024.0000	512.0000	512.0000
81 - Matrix size Density map J .....:	512.0000	512.0000	512.0000
82 - Matrix size source map J .....:	512.0000	512.0000	512.0000
83 - Cut-off energy to terminate photon history..:	0.0000	0.0000	0.0000
84 - Scoring routine .....:	1.0000	1.0000	1.0000
85 - CSV file content .....:	0.0000	0.0000	0.0000
86 - Dynamic study..... :	0.0000	0.0000	0.0000

C H A N G E: Collimator parameters: SY-LEHR	SY-LEHR	SY-ME
46 - Hole Size X..... cm:	0.1110	0.2940
47 - Hole Size Y..... cm:	0.1282	0.3395
48 - Distance between holes in x-direction.....cm:	0.0160	0.1140
49 - Distance between holes in y-direction.....cm:	0.0918	0.3672
50 - Displacement center hole in x-direction...cm:	0.0635	0.2040
51 - Displacement center hole in y-direction...cm:	0.1100	0.3533
52 - Collimator thickness.....cm:	2.4050	4.0640
53 - Collimator routine .....:	1.0000	1.0000
54 - Hole shape:2=Cir,3=Hex,4=Rect.....:	-3.0000	-3.0000
55 - Type: 0=PA,1=PI,2=CO,3=FB,4=DV,5=SH .....:	0.0000	0.0000
56 - Distance from collimator to detector.....cm:	0.0000	0.0000
57 - .....:	0.0000	0.0000
58 - .....:	0.0000	0.0000
59 - Random collimator movement (0=no).....:	0.0000	0.0000
60 - .....:	0.0000	0.0000

Appendix B – NMISA Calibration Certificate for I-123

nmisa
National Metrology Institute of South Africa

Certificate of Analysis

15 Lower Hope Road, Rosebank, Cape Town, 7700
Tel: +27 21 685 2065/7776
Fax: +27 21 686 2759
E-mail enquiries: info@nmisa.org
www.nmisa.org

Analysis of:	One I-123 solution
Description of sample:	I-123 solution in a 10 ml glass vial
Identification of sample:	I-123 30/09/2020
Analysed for:	University of the Free State Faculty of Health Sciences Department of Medical Physics Bloemfontein E-mail: gnbijvs@ufs.ac.za ; Telephone: (051) 405-3156/ 2831
Location of preparation- and analysis:	Radioactivity Standards Laboratory 15 Lower Hope Road Rosebank, Cape Town
Preparation procedures:	RS-WEI-0001-11 & RS-WEI-0002-7
Analysis procedure:	RS-TEC-0015-4
Date sample received:	2 October 2020
Period of analysis:	7 October 2020

1 PROCEDURE

a) Analysis required

The solution was received in a 10 ml glass vial for analysis of gamma-emitting radionuclides.

b) Methods

A counting sample was prepared (weighed on calibrated balances) in a 100 ml plastic bottle containing 52,306 (± 0,016) g de-ionized water, as per NMISA weighing procedures. An energy calibrated, closed-end coaxial vertical High-Purity Germanium (HPGe) detector was used to measure a 20 hour live-timed gamma-ray energy spectrum of the sample in the 100 ml plastic bottle. The spectrum was corrected for background and an efficiency curve was determined through a Monte Carlo simulation.

Analysis of the spectrum resulted in the identification of the radionuclides provided in the Results section, with corresponding radioactivity level, combined uncertainty at 1 sigma (coverage factor k = 1) and Minimum Detectable Activity (MDA) concentration calculated from the ISO11929 MDA formula with a 95 % confidence level.

Analysed by **M.W. van Rooy** **Metrologist**	Checked by **J. Lubbe** **Metrologist**	For Chief Executive Officer
Date of Issue **04 November 2020**	**Page 1 of 3**	Certificate number **RS\20-34**

Your measure of excellence

c) Equipment and standards used

Description	NMISA Inventory No.
Sartorius electronic toploader balance, model E 2000 D	NAC 03863
Mettler microbalance, model M3	NAC 00877
Canberra High-Purity Germanium (HPGe) detector, model GC3018	NNR-RS-001
NMISA mixed radionuclide (Co-60, Cs-137, Eu-152, Am-241) water equivalent standard	NMISA Mixed RN 01

The results of the measurements are traceable to the relevant national measurement standards for radioactivity.

2 RESULTS

Radionuclide(s) identified and the corresponding reference date, activity concentration and Minimum Detectable Activity (MDA) concentration are shown in Table 1 below. The activity concentration was determined using the **buoyancy-corrected** sample mass provided below.

Sample mass: 0,124061 (± 0,000044) g.

Table 1.

Radionuclide	Reference date	Activity concentration (Bq/g)	Uncertainty at 1σ (Bq/g)	MDA (Bq/g)
I-123	2 October 2020, 12h00 SAST	$1{,}815 \times 10^{6}$	$\pm 1{,}595 \times 10^{5}$	1 030
I-125	2 October 2020, 12h00 SAST	$1{,}404 \times 10^{5}$	$\pm 2{,}392 \times 10^{4}$	784
I-133	2 October 2020, 12h00 SAST	$3{,}534 \times 10^{2}$	$\pm 1{,}771 \times 10^{2}$	117
Sb-122	2 October 2020, 12h00 SAST	5,8	± 2,0	2,3
Xe-131m	2 October 2020, 12h00 SAST	74,4	± 11,1	30,2

3 REMARKS

3.1 The results in this certificate relate only to the sample mentioned herein.

3.2 The results provided in this certificate were obtained from methods that are not included in the SANAS Schedule of Accreditation for this laboratory.

3.3 The reported uncertainties of measurement were calculated and expressed in accordance with the BIPM, IEC, ISO, IUPAP, OIML document entitled "A Guide to the Expression of Uncertainty in Measurement" (International Organisation for Standardisation, Geneva, Switzerland, 2008).

3.4 Certain of the NMISA certificates are consistent with the capabilities that are included in appendix C of the MRA (Mutual Recognition Arrangement) drawn up by the CIPM. Under the MRA, all participating institutes recognise the validity of each other's calibration and measurement certificates for the quantities and ranges and measurement uncertainties specified in Appendix C. For details see http://www.bipm.org.

3.5 The analyses were carried out at an ambient temperature of 21 °C ± 3 °C and a relative humidity of 58 %RH ± 15 %RH.

---------- end of certificate ----------

Analysed by **M.W. van Rooy** **Metrologist**	Checked by **J. Lubbe** **Metrologist**	For Chief Executive Officer
Date of Issue **04 November 2020**	**Page 3 of 3**	Certificate number **RS\20-34**

Appendix C – SASNM Congress 2021 – Abstract

LEHR vs ME collimated I-123 SPECT image quality: A Monte Carlo study

A Richards, JA van Staden, H du Raan

Department of Medical Physics, University of the Free State, Bloemfontein

I-123 is performed in clinical SPECT imaging using the 159keV γ-ray. High-energy photons between 440 keV and 784 keV are also part of the I-123 decay scheme. These photons have a noted influence on image quality and quantification accuracy due to septal penetration and scatter. Imaging with a medium energy (ME) collimator is preferred to the low-energy high resolution (LEHR) collimator, as it reduces the effects of high-energy photons. However, this comes at the cost of spatial resolution and an extra collimator set. Reconstruction algorithms correcting for collimator detector response (CDR), which includes septal penetration and scatter, may result in improved LEHR collimator SPECT imaging. The aim of this study was to compare LEHR and ME SPECT image quality after applying attenuation, scatter and CDR corrections to the data.

Monte Carlo software was used to simulate SPECT images of the Carlson quality control phantom. Images were reconstructed using the OSEM algorithm with CT-based attenuation, effective source scatter estimation and CDR corrections. Uniformity, cold contrast and hot lesion resolution were evaluated semi-quantitatively. The influence of the CDR correction on both datasets was evaluated.

Uniformity profiles obtained through the LEHR and ME images were comparable. The ME collimator images had a negligible difference in noise compared to LEHR images when full CDR was applied (6% vs 7%), and cold contrast values were comparable (LEHR: 21% vs ME: 23%). The resolution section of the phantom yielded similar results between the ME and LEHR collimator. The contrast values obtained with and without the CDR correction, were compared. A significant improvement in contrast was obtained for the LEHR collimator data after applying the CDR correction (8% to 21%). The contrast improvement for the ME collimator data was small (19% to 23%).

The results show that the LEHR collimator yields images comparable to the ME collimator when reconstructed with CDR correction and can be considered for routine clinical imaging.

Appendix D – Ethical Approval Letter

UNIVERSITY OF THE FREE STATE
UNIVERSITEIT VAN DIE VRYSTAAT
YUNIVESITHI YA FREISTATA

UFS·UV
HEALTH SCIENCES
GESONDHEIDSWETENSKAPPE

Health Sciences Research Ethics Committee

10-Nov-2020

Dear Miss **Anneray Richards**

Ethics Number: UFS-HSD2019/0151/2801-0001

Ethics Clearance: **Quantification Accuracy for I-123 SPECT/CT studies using LEHR and ME collimators: A Monte Carlo Study**

Principal Investigator: **Miss Anneray Richards**

Department: **Medical Physics Department (Bloemfontein Campus)**

SUBSEQUENT SUBMISSION APPROVED

With reference to your recent submission for ethical clearance from the Health Sciences Research Ethics Committee. I am pleased to inform you on behalf of the HSREC that you have been granted ethical clearance for your request as stipulated below:

- Continuation report:
  Annual re-approval until 26 Nov 2021

The HSREC functions in compliance with, but not limited to, the following documents and guidelines: The SA National Health Act. No. 61 of 2003; Ethics in Health Research: Principles, Structures and Processes (2015); SA GCP(2006); Declaration of Helsinki; The Belmont Report; The US Office of Human Research Protections 45 CFR 461 (for non-exempt research with human participants conducted or supported by the US Department of Health and Human Services- (HHS), 21 CFR 50, 21 CFR 56; CIOMS; ICH-GCP-E6 Sections 1-4; The International Conference on Harmonization and Technical Requirements for Registration of Pharmaceuticals for Human Use (ICH Tripartite), Guidelines of the SA Medicines Control Council as well as Laws and Regulations with regard to the Control of Medicines, Constitution of the HSREC of the Faculty of Health Sciences.

For any questions or concerns, please feel free to contact HSREC Administration: 051-4017794/5 or email EthicsFHS@ufs.ac.za.

Thank you for submitting this request for ethical clearance and we wish you continued success with your research.

Yours Sincerely

Dr. SM Le Grange
Chair : Health Sciences Research Ethics Committee

Health Sciences Research Ethics Committee
Office of the Dean: Health Sciences
T: +27 (0)51 401 7795/7794 | E: ethicsfhs@ufs.ac.za
IRB 00011992; REC 230408-011; IORG 0010096; FWA 00027947
Block D, Dean's Division, Room D104 | P.O. Box/Posbus 339 (Internal Post Box G40) | Bloemfontein 9300 | South Africa
www.ufs.ac.za

Appendix E – Turnitin Report

MMedSc

ORIGINALITY REPORT

9%	5%	7%	0%
SIMILARITY INDEX	INTERNET SOURCES	PUBLICATIONS	STUDENT PAPERS

PRIMARY SOURCES

1	www.ncbi.nlm.nih.gov Internet Source	3%
2	Michaella Morphis, Johan A. van Staden, Hanlie du Raan, Michael Ljungberg. "Modelling of energy-dependent spectral resolution for SPECT Monte Carlo simulations using SIMIND", Heliyon, 2021 Publication	1%
3	D Minarik. "Evaluation of quantitative ^{90}Y SPECT based on experimental phantom studies", Physics in Medicine and Biology, 10/21/2008 Publication	1%
4	discovery.ucl.ac.uk Internet Source	<1%
5	"Basic Sciences of Nuclear Medicine", Springer Science and Business Media LLC, 2011 Publication	<1%
6	Gopal B. Saha. "Physics and Radiobiology of Nuclear Medicine", Springer Science and	<1%

	Business Media LLC, 2006 Publication	
7	iopscience.iop.org Internet Source	<1 %
8	"Handbook of Nuclear Chemistry", Springer Nature, 2011 Publication	<1 %
9	www.sciencegate.app Internet Source	<1 %
10	theses.gla.ac.uk Internet Source	<1 %
11	M. Booyens, M. Morphis, J. Van Staden, H. du Raan. "Verification of a Monte Carlo simulated Siemens Symbia SPECT/CT", Physica Medica, 2015 Publication	<1 %
12	www.hindawi.com Internet Source	<1 %
13	Verschure, Derk O., Tim C. de Wit, Vivian Bongers, Petronella J. Hagen, Charlotte Sonneck-Koenne, Julia D'Aron, Kurt Huber, Berthe L.F. van Eck-Smit, Peter Knoll, Gerhard Aernout Somsen, Siroos Mirzaei, and Hein J. Verberne. "123I-MIBG heart-to-mediastinum ratio is influenced by high-energy photon penetration of collimator septa from liver and	<1 %

	lung activity :", Nuclear Medicine Communications, 2014. Publication	
14	"Nuclear Oncology", Springer Science and Business Media LLC, 2017 Publication	<1 %
15	jnm.snmjournals.org Internet Source	<1 %
16	Pernilla Nordberg. "Quantification and optimisation of lung ventilation SPECT images", Linkoping University Electronic Press, 2014 Publication	<1 %
17	"Computer Methods in Biomechanics and Biomedical Engineering", Springer Science and Business Media LLC, 2018 Publication	<1 %
18	Alicia Aliena-Valero, Mikahela A. López-Morales, María C. Burguete, María Castelló-Ruiz et al. "Emergent Uric Acid Treatment is Synergistic with Mechanical Recanalization in Improving Stroke Outcomes in Male and Female Rats", Neuroscience, 2018 Publication	<1 %
19	Radiolabeled Monoclonal Antibodies for Imaging and Therapy, 1988. Publication	<1 %

20	research.library.mun.ca Internet Source	<1 %
21	Dan J Kadrmas. Physics in Medicine and Biology, 04/1998 Publication	<1 %
22	Arda Könik, Benjamin Auer, Jan De Beenhouwer, Kesava Kalluri, Navid Zeraatkar, Lars R Furenlid, Michael A King. "Primary, scatter, and penetration characterizations of parallel-hole and pinhole collimators for I-123 SPECT", Physics in Medicine & Biology, 2019 Publication	<1 %
23	Tsui, B.M.W.. "Quantitative myocardial perfusion SPECT", Journal of Nuclear Cardiology, 199809/10 Publication	<1 %
24	Submitted to University of Limerick Student Paper	<1 %
25	Whiting, Bruce R., Christoph Hoeschen, Nouf Abuhadi, David Bradley, Dev Katarey, Zsolt Podolyak, and Salem Sassi. "Investigation of the quantitative accuracy of 3D iterative reconstruction algorithms in comparison to filtered back projection method: a phantom study", Medical Imaging 2014 Physics of Medical Imaging, 2014. Publication	<1 %

26	Yong Du. "Model-based compensation for quantitative ^{123}I brain SPECT imaging", Physics in Medicine and Biology, 03/07/2006 Publication	<1 %
27	N Song. "EQPlanar: a maximum-likelihood method for accurate organ activity estimation from whole body planar projections", Physics in Medicine and Biology, 09/07/2011 Publication	<1 %
28	van Gils, C A J, C Beijst, R van Rooij, and H W A M de Jong. "Impact of reconstruction parameters on quantitative I-131 SPECT", Physics in Medicine and Biology, 2016. Publication	<1 %
29	"X-Ray Astronomy in the Exosat Era", Springer Science and Business Media LLC, 1985 Publication	<1 %
30	Mattijs Elschot, Maarten L. J. Smits, Johannes F. W. Nijsen, Marnix G. E. H. Lam et al. "Quantitative Monte Carlo-based holmium-166 SPECT reconstruction", Medical Physics, 2013 Publication	<1 %
31	Hine, Gerald J., Peter Paras, and Charles P. Warr. "", Recent and Future Developments in Medical Imaging I, 1978. Publication	<1 %

32	Submitted to University of Surrey Student Paper	<1 %
33	Chenggang Yu, Xiaohe Wang, Chen Wu, Chunyan Zou, Jianhui Wu, Xiangzhou Cai, Jingen Chen. "Supply of I-131 in a 2 MW molten salt reactor with different production methods", Applied Radiation and Isotopes, 2020 Publication	<1 %
34	Submitted to King's College Student Paper	<1 %
35	Xing Rong. "A method for energy window optimization for quantitative tasks that includes the effects of model-mismatch on bias: application to Y-90 bremsstrahlung SPECT imaging", Physics in Medicine and Biology, 06/21/2012 Publication	<1 %
36	hdl.handle.net Internet Source	<1 %
37	intrans.iastate.edu Internet Source	<1 %
38	D Lazaro. "Fully 3D Monte Carlo reconstruction in SPECT: a feasibility study", Physics in Medicine and Biology, 08/21/2005 Publication	<1 %

39	Garcia, Marie-Paule, Julien Bert, Didier Benoit, Manuel Bardiès, and Dimitris Visvikis. "Accelerated GPU based SPECT Monte Carlo simulations", Physics in Medicine and Biology, 2016. Publication	<1 %
40	Submitted to University of Sydney Student Paper	<1 %
41	etheses.dur.ac.uk Internet Source	<1 %
42	Bin He. "Comparison of conventional, model-based quantitative planar, and quantitative SPECT image processing methods for organ activity estimation using In-111 agents", Physics in Medicine and Biology, 08/21/2006 Publication	<1 %
43	Habib Zaidi, Kenneth F. Koral. "Scatter modelling and compensation in emission tomography", European Journal of Nuclear Medicine and Molecular Imaging, 2004 Publication	<1 %
44	I Laurette. Physics in Medicine and Biology, 11/2000 Publication	<1 %
45	jcem.endojournals.org Internet Source	<1 %

46	livrepository.liverpool.ac.uk Internet Source	<1 %

Exclude quotes	On	Exclude matches	< 10 words
Exclude bibliography	On		

Dr JA van Staden